UNIVERSITÀ
DEGLI STUDI
FIRENZE

DOTTORATO DI RICERCA IN
FISICA E ASTRONOMIA

CICLO XXXIV

COORDINATORE Prof. D' Alessandro Raffaello

Laboratory studies on photoprocessing and desorption of prebiotic molecules in space

Settore Scientifico Disciplinare FIS/05

Dottorando
Dott. Corazzi Maria Angela
(firma)

Tutori
Prof. Brucato John Robert
(firma)

Prof. Casetti Lapo
(firma)

Coordinatore
Prof. D' Alessandro Raffaello
(firma)

Anni 2018/2021

Contents

1 Infrared and Mass Spectrometry theory **14**
1.1 Infrared reflectance spectroscopy 14
1.1.1 Fourier-Trasform InfraRed spectroscopy (FTIR) 21
1.2 Mass spectroscopy 25
1.2.1 Temperature-Programmed Desorption (TPD) 28

2 Astrophysics in laboratory **39**
2.1 Astrobiology laboratory and facilities 40
2.1.1 Samples preparation 40
2.2 Experimental setup 42
2.2.1 Bruker VERTEX 70v 42
2.2.2 Hiden Analytical Quadrupole Mass Spectrometer . . . 44
2.2.3 Vacuum and cryogenics techniques 45
2.2.4 UV irradiation system 52

3 Photoprocessing of formamide ice **57**
3.1 Formamide and minerals 58
3.2 Laboratory procedure and UV photodissociation analysis . . . 60
3.2.1 Results and discussion 62
3.3 Laboratory procedure and Thermal Desorption analysis 69
3.3.1 Results and discussion 73

4 Thermal desorption of acetaldehyde and acetonitrile from olivine dust **81**
4.1 Acetaldehyde and Acetonitrile 82
4.2 Laboratory procedure, samples preparation and thermal desorption diagnostic 83
4.3 Thermal desorption from olivine grains results 85
4.4 Discussion and astrophysical implication 98
4.4.1 Interaction with water 98
4.4.2 The role of grains 103

4.4.3 Comparison with the observed abundance ratios 105
4.4.4 Highlighted results 106

5 Photoprocessing of acetaldehyde and acetonitrile ices mixed with olivine 108
5.1 Results 109
5.1.1 UV irradiation of acetonitrile and acetaldehyde 109
5.1.2 UV irradiation of acetonitrile and acetaldehyde in presence of olivine grains 118
5.1.3 UV radiation and olivine grains 127
5.2 Discussion and astrophysical implication 136
5.2.1 The effects of UV radiation and iCOMS in PDRs . . . 136
5.2.2 The catalytic role of olivine and the high masses observed 139

6 Conclusions 143

Bibliography 150

Introduction

Over 200 different molecular species have been detected in the interstellar and circumstellar medium to date. Of these, about 50 contain 6 or more atoms and the carbon. These molecules have been defined by astronomers as interstellar complex organic molecules (iCOMs)(e.g., Blake et al. 1987).

Why are we interested in iCOMs and what is meant by prebiotic molecules? The origin of life is one of the open themes that has always fascinated humanity. How did life originate and why on Earth while it seems to be a challenge elsewhere? These questions are still far from being resolved and span a wide range of disciplines, including astrobiology and astrochemistry.

Through laboratory studies, it is possible to enter one of the most fascinating and unsolved aspects of astrobiology and astrochemistry: the origin of the chemical complexity that we observe today on Earth.

This Ph.D. project is focused on laboratory studies of photoprocessing and thermal desorption of prebiotic molecules, the building blocks of life, in simulated space conditions. We will see that photoprocessing and thermal desorption are among the fundamental processes for the evolution and preservation of molecules in space and for their observation in the gas phase respectively. Before going into the specifics of my Ph.D. work, i.e., how to simulate the processes involving prebiotic molecules, we will describe what is meant by prebiotic molecules or interstellar complex organic molecules, why they are important, and in which astrophysical environments they are observed. To do this, we will first briefly describe the interstellar medium (ISM), and what we can observe and know thanks to space astronomy and infrared observatories. We will briefly describe the different evolutionary phases involved in low-mass star formation, i.e., a star and planetary system like our own. In this way, according to the astrophysical environment that hosts a complex molecule, we will know at what moment (age) we are in the star and planets formation. Next, we will talk about iCOMs, why to look for them in star-forming regions, the state of the art and what we know about their formation and evolution processes, and how laboratory experiments fit into this context.

ISM, and Star Formation In astronomy, the interstellar medium (ISM) is the rarefied material found in the space between stars within a galaxy and is typically traced back to gas and dust. The ISM plays a fundamental role in the composition of the Universe as it provides material for star formation and is enriched by the death of the stars themselves. The birth of a star occurs within dense regions made of gas and dust that hide the process from our eyes. Thanks to space astronomy and infrared observatories such as Spitzer Space Telescope, the InfraRed Astronomical Satellite (IRAS), and Hubble Space Telescope (HST), we were able to penetrate dust and gas and partially understand star birth and formation. In 1983, the launch of IRAS made it possible to observe dusty disks around young stars. The ISO infrared satellite provided detailed mid-infrared spectra of many light disks. The Spitzer Space Telescope revealed mid-infrared emission of the disk in very large samples of stars spanning a wide range of age. At the same time, radio wavelength interferometry provided high spatial resolution images of cold dust and gas in the outer disks and estimates of the masses of the disk itself. The Hubble Space Telescope provided images of disks in a wide variety of environments and produced important constraints on accretion rates due to observations in the ultraviolet. Theoretical knowledge of star formation processes was also improved thanks to time-dependent numerical simulations that integrate analytical and stationary models. However, there are still many open points. There is no conclusive theory explaining the stellar initial mass function, and there is no conclusive theory on understanding the angular momentum transport mechanisms that drive disk accretion despite numerous advances. Despite this, a coherent picture of star formation is emerging (Hartmann 2009).

We know that the ISM consists of 7-11$\cdot$ 10^9 $M_\odot$ of gas. The molecular gas H_2 (T$\sim$ 10 K) is 1-2$\cdot 10^9$ $M_\odot$ and it is concentrated in clouds, clumps, and cores. The cold atomic gas HI (T$\sim$50 K) is 2-3$\cdot 10^9$ $M_\odot$, the warm atomic gas HI (T$\sim$ 8000 K) is 3-5$\cdot$ 10^9 $M_\odot$, and the ionized gas HII (T$\sim$ 10^4 - 10^6 K) is $1\cdot 10^9 M_\odot$. In the Milky Way, most of the gas is distributed near the plane of the galaxy's disk. The molecular gas H_2 increases towards the Galactic center and it is concentrated in the inner regions of the molecular ring about 3-5 kpc from the center where the galaxy's brightest star-forming regions are present. The atomic gas H is instead distributed more uniformly (see Figure 1). The young stars are generally distributed near or within clouds of relatively dense molecular gas. In a molecular cloud, most of the gas is H_2 and the temperatures are generally in the 10-20 K range.

Stars form in dense, cold molecular clouds that show low turbulent motions. Indeed, the formation of a star requires that gravity overcomes the resisting forces of thermal gas pressure, turbulent movements, and mag-

netic fields. Molecular clouds have a complex spatial structure characterized by substructures such as filaments, sub-filaments, hub-like networks, fibers, threads, ridges, and cores. These substructures are clearly related to the star formation. Molecular cloud "cores" are regions with densities $>10^3$ cm^{-3}, and are thought to be the predecessors of low-mass stars. They are objects close to gravitational instability and they are typically found from radio-frequency surveys of spectral lines of NH_3, a molecule excited at high gas densities (e.g., Wolfire et al. 2003). In Taurus, cloud cores have densities $>10^4$ cm^{-3} and sizes $\sim$ 0.1 pc (e.g., Wolfire et al. 2003, Myers et al. 1983). At such high densities, the predicted times for gravitational collapse are only a few hundred thousand years, and star formation could proceed fairly quickly from these cores. Hence, the first phase is represented by a pre-stellar core, which is a cold (T<10 K) and dense condensation of molecular gas and dust in which matter accumulates towards its center (e.g., López-Sepulcre et al. 2019). A Class 0 protostar is formed and the protostellar phase begins. This phase lasts about 10^4 years. During the protostellar phase, the Class 0 protostars are embedded in the parental nucleus and are increasing their mass. The gravitational energy due to a faster collapse to the center causes the warm-up of the inner core envelope and the sublimation of the icy mantles recovering dust grains. In this phase, the hot corinos are formed, i.e., compact (<100 astronomical units, AU) and hot (T>100 K) regions, where the temperatures are hot enough to evaporate dust mantles and trigger a gas-phase chemistry (see e.g., López-Sepulcre et al. 2019). Later ($\sim 10^5$ years), disk-like growth structures begin to form and, at this stage (Class 1 protostar), violent ejections of material in the form of bipolar jets ant outflows occur. The more evolved phase is the protoplanetary disk phase, where the envelope of the protostellar object is dissipated, and only the disk remains. This is the region where planetesimals and small bodies around the newly born star can form. In all these objects, i.e., along the formation process of a Sun-like star, iCOMs are observed.

iCOMs The presence of iCOMs in different space environments leads us to question how organic chemistry works in space, how the chemical complexity that we observe today is formed, what type of chemistry is along the star and planetary formation process.

Life can be considered as something complex. A single living being is composed of the same basic elements: carbon (C), hydrogen (H), oxygen (O), and nitrogen (N). These elements are easily found anywhere in the Universe and today we know that, in many space environments, they can also be found as complex organic molecules (e.g. CH_3OH, $HCOOCH_3$, CH_3NH_2,

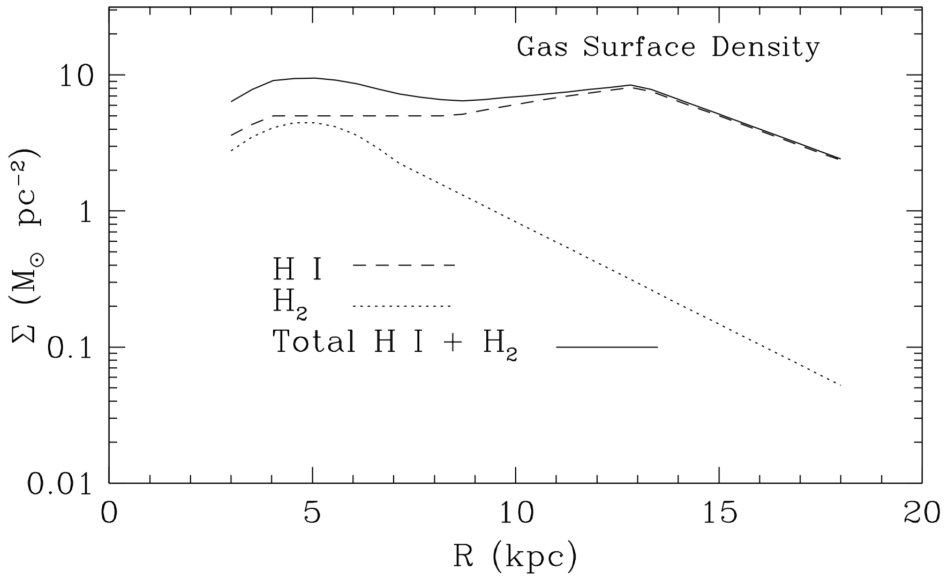

Figure 1: Galactic distribution of atomic and molecular gas (Wolfire et al., 2003).

CH_3CH_2CN) (see e.g., López-Sepulcre et al. 2019).

Millimeter and centimeter observations are discovering an increasing number of iCOMs in a large variety of star forming sites. The advent of large interferometers in the (sub-)mm range, such as IRAM-NOEMA and ALMA, have shown the presence of iCOMs in all stages of the Solar-like star formation process: from the earliest stages of star formation (see e.g., the review by Caselli et al. 2012), i.e., in pre-stellar dense cores (e.g., Bacmann et al. 2012, Vastel et al. 2014), in hot corinos around protostars (e.g., Cazaux et al. 2003, Ceccarelli et al. 2007), and in the associated jets and outflows (e.g., Bachiller et al. 1997, Arce et al. 2008, Codella et al. 2010, Lefloch et al. 2017), to protoplanetary disks. The latter are of particular interest because they are the place where planets form, which could inherit their chemical complexity. In the case of protoplanetary disks, complex species are hardly detected because the region where the dust temperature is high enough to let water ice and iCOMs to thermally desorb (T>100 K) is very small ($\lesssim$ 5 AU) for Solar-like stars (e.g., Cieza et al. 2016, see sketch reported in panel a in Figure 2). Only methanol (Walsh et al. 2016, Podio et al. 2020), acetonitrile (e.g., Öberg et al. 2015), and formic acid (Favre et al., 2018) have been observed so far. A new fascinating perspective was recently provided by FU Ori objects in which the young central star undergoes a strong accretion burst, hence a sudden increase in brightness which leads to heating of the surrounding disk and to a quick expansion of the molecular snow lines to larger radii (see sketch reported in panel b in Figure 2). This phenomenon was first observed in V883 Ori by Cieza et al., 2016. These latter authors observed that the increase in brightness extended the water snow line up to 42 AU. Methanol has been detected in this disk by Hoff et al., 2018: the transitions observed suggest the thermal desorption of methanol from dust grains from the surface layers beyond or within the water snow line, which would therefore have extended up to 100 AU. Thanks to the increase in temperature of the disk, five iCOMs thermally desorbed from the disk were later detected: methanol, acetone, acetonitrile, acetaldehyde, and methyl formate (Lee et al. 2019). Moreover, prebiotic iCOMs considered precursors of a large number of organic compounds essential for life, such as formamide (NH_2CHO), have been identified in comets that are considered to have partly inherited their current chemical composition during the birth of the Solar System. Thus, a non-negligible amount of organic compounds may have been exogenously released on Earth about four billion years ago (López-Sepulcre et al. 2019).

Various different mechanisms have been invoked in the literature to explain the formation and observed abundances of complex molecules. The processes considered efficient in governing the chemistry of the interstellar

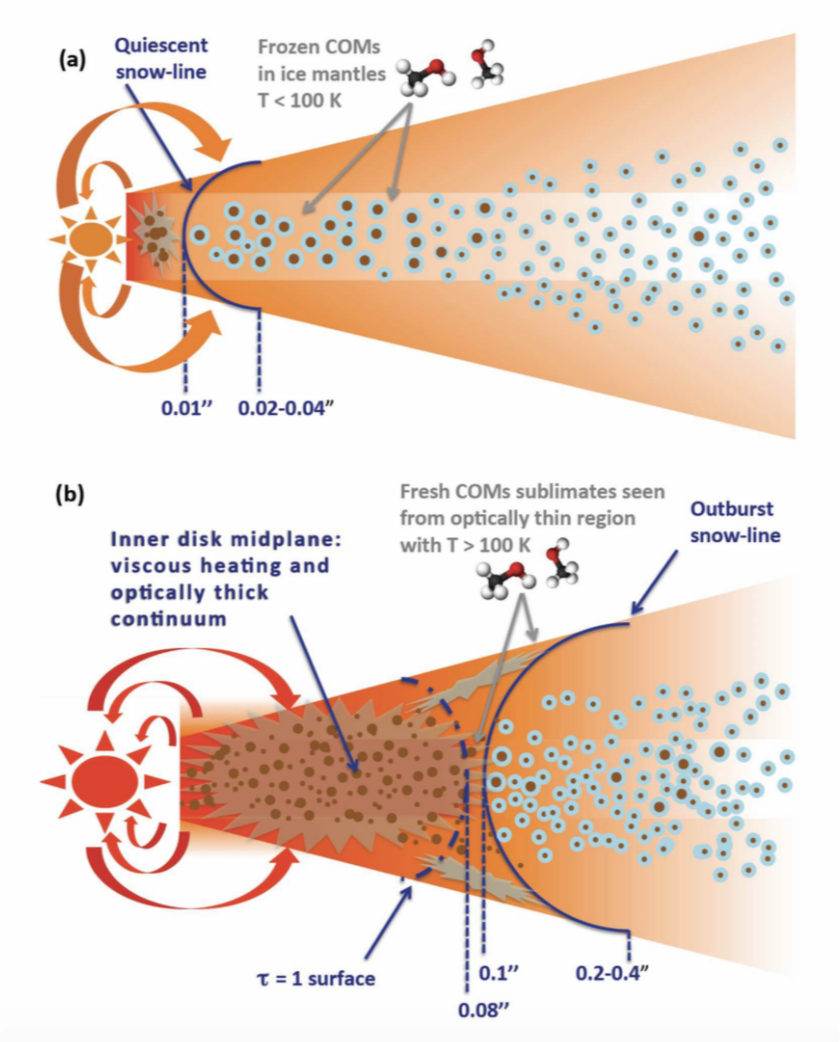

Figure 2: The sketches shown in Figure reveal the differences between a protoplanetary disk around a Solar-like star (Fig. a) and a FuOri object (Fig. b). The sketch (a) shows that in a protoplanetary disk around a Solar-like star, the region where the dust temperature is high enough to let the water and iCOMs thermal desorption (>100 K) is very small. At a distance from the central star greater than 0.01"($\sim$ 5 AU), the dust temperatutre is lower than 100 K and the iCOMs are frozen in the ice mantles. The sketch (b) shows what happens in a FuOri object. The central star undergoes a sudden accretion burst which leads to heating of the surrounding disk and to a quick expansion of the molecular snow lines to larger radii (0.08" $\sim$100 AU) (Lee et al. 2019).

medium are divided into two categories: the reactions that occur in the solid phase on the surface of the grains and the reactions that occur in the gas phase. One formation mechanism of complex iCOMs on the dust grains present in the interstellar medium is the subsequent CO hydrogenation (see e.g., López-Sepulcre et al. 2019), which can form methanol CH_3OH (e.g., Garrod et al. 2007, Wirström et al. 2011), glycoaldehyde $COHCH_2OH$, ethylene glycol $(CH_2OH)_2$, and methyl formate $HCOOCH_3$ (e.g., Simons et al. 2020). Once the molecules have formed on the grains, an important aspect is the processing they can undergo through low-energy cosmic rays (Palumbo et al. 1993), X-ray (Ciaravella et al. 2010), and UV (e.g., Meinert et al. 2016) photons irradiation.

In particular, UV radiation is one of the mechanisms responsible for chemical evolution in space promoting photochemical reactions on surfaces of dust grains. Laboratory experiments simulating thermal and energetic processing of interstellar ice analog showed how new molecules, radicals, and fragments are produced by the ice photoprocessing (e.g., Agarwal et al. 1985, D'Hendecourt et al. 1986, Bernstein et al. 1995, Muñoz Caro et al. 2003, Muñoz Caro et al. 2004, Kouchi et al. 2005, Materese et al. 2011, Bertin et al. 2016, Abou Mrad et al. 2016). Photolysis and photoprocessing of interstellar grains are important processes during most of the grain's life, including the time spent in dense clouds, when the grains are photoprocessed for the penetration of UV radiation (Whittet et al. 1998). The presence of neighboring young massive stars can also expose the material within the cloud to intense UV fields, with a typical scale length of the UV penetration of 1 pc (Beuther et al. 2000, Muñoz Caro et al. 2003). The laboratory results of Hagen et al., 1979 followed the evolution of grain analogs by observing the infrared absorption spectra of photolyzed ice samples deposited at 10 K. The evolution of grain, the creation and storage of radicals, and the molecule production is depicted as a statistical process within the dense clouds. The authors observed that the astronomically observed shape and position of the 3.1 μm band is doubled in the laboratory as a consequence of the processing of the grain mantle. Moreover, the reduction of the characteristic band to 3.4 μm is the observational evidence of the photoprocessing of grains exposed to UV radiation in dense clouds (e.g., Muñoz Caro et al. 2001, Muñoz Caro et al. 2003).

The photoprocessing can take place in different protostellar regions and in environments where the iCOMs are observed at different evolutionary stages: around young stellar objects (e.g., Aikawa et al. 1999, Gibb et al. 2000) or in the outer regions of the circumstellar environments, where there are the UV photons scattered by dust in the bipolar outflow cavities around protostars (e.g., Spaans et al. 1995, Kempen et al. 2009).

Energetic processing have an important role also during the formation and evolution of protoplanetary disks. The disk can be schematically divided into three layers in the vertical direction: the middle plane, the intermediate region, and the outer surface regions where the molecules are dissociated by UV radiation (Aikawa et al. 1998). By looking at the CO emission maps in the highly inclined circumstellar disk around SSTC2D J163131.2-242627 (Flores et al. 2021), the temperature in the midplane of $\sim$33 K and $\sim$20 K at radii $<$200 AU were derived. At distances larger than 200 AU, the disk midplane temperature rises to $\sim$30 K, with an almost vertical isothermal profile. The authors interpreted this increase due to interstellar UV radiation which provides a source of heating to the outer region of the disk. Furthermore, above 100 AU, the magnetic field couples to the gas causing turbulence and vertical mixing of the material in the accretion disk with a time scale of 10^5 years, shorter than the average life of the accretion disk, 10^6 years. So, most of the material in the outer disk is subjected to stellar photons and complete photolysis (Muñoz Caro et al. 2003, Aikawa et al. 1996).

In the disk around the Herbig star HD 179218, Taha et al., 2018 observed the emission of the polycyclic aromatic hydrocarbons (PAHs). Using radiative transfer (RT) model of the continuum, it was found that PAH molecules extend along the surface of the disk and are excited and ionized by stellar UV photons even at large distances. So, they are in a state of ionized charge due to the strong UV radiation field due to the central star. Finally, Muñoz Caro et al., 2003 calculated that at 100 AU from the central star in a disk of the T Tauri phase with a UV field of intensity 10^{12} photons$\cdot$cm$^{-2}\cdot$sec^{-1} (Herbig et al. 1986) and for a UV cross-section of 10^{-18}cm^2, a molecule absorbs about 1 UV photon per week inside the ice mantle, enough to convert $\sim$10% of the carbon in the ice into complex organic molecules.

On the other hand, many works show how complex molecules can be formed through gas-phase ion-molecule reactions in cold and dense gas (e.g., Duley et al. 1984, Caselli et al. 2012), and through gas phase reactions taking place in the protostellar phase once the icy mantles sublimate in the warm regions (Charnley et al. 1995).

To correctly interpret the distribution and abundances of iCOMs observed along the formation process of a Sun-like stars, we need to comprehend their formation processes and the mechanisms responsible for their release in gas-phase. The release of molecules in the gaseous phase can be both non-thermal and thermal. Non-thermal desorption mechanisms occur in environments such as dark starless cores (e.g., Smith et al. 1993, Garrod et al. 2007, Navarro-Almaida et al. 2020), or outflows and winds around protostars where the release in the gaseous phase of a large number of molecules is due to gas-grain and grain-grain collisions (e.g., Codella et al. 2017). Among

the non-thermal desorption processes, there is photo-evaporation due to UV photons induced by cosmic rays. This process appears to be responsible for the gaseous phase release of methanol (CH_3OH) in different environments such as a spiral arm of M51 (Watanabe et al. 2014) and the Taurus Molecular Cloud-1 (Soma et al. 2015). Another non-thermal desorption mechanism is X-ray desorption of molecules from grains in protoplanetary disks (e.g., Najita et al. 2001, Andrade et al. 2010, Mendoza et al. 2013, Dupuy et al. 2018, Ciaravella et al. 2020, Basalgéte et al. 2021). Instead, thermal desorption plays a dominant role in regions where icy mantles of dust grains are released in the gaseous phase due to the high temperatures (>100 K) present, as in hot corinos or FuOri objects.

Through laboratory analyses, it is possible to study the physical and chemical processes involving iCOMs and their interactions with grains analog to interstellar ones. The last three decades have shown the importance of laboratory experiments to experimentally verify the efficiency of the mechanisms invoked to explain the formation of iCOMs (e.g., Muñoz Caro et al. 2003, Urso et al. 2017, Kanuchová et al. 2016, Bergantini et al. 2014, Gerakines et al. 2004). Further studies have clarified the evolution and conservation of iCOMs in hostile astronomical environments (e.g., Mennella 2015, Baratta et al. 2015) where the presence of grains can play a key role. Minerals may play a fundamental role in processes that lead to the emergence of complex molecules because they can act as catalysts, promoting chemical reactions and the synthesis of new molecular species on their surface or protecting molecules against UV degradation. Moreover, they can adsorb molecules allowing their concentration in the ice mantles (e.g., Fornaro et al. 2013).

Laboratory studies are crucial to study the evolution and preservation of processed complex molecules and organic compounds in harsh astronomical environments. Moreover, the interpretation of iCOMs observations in various star-forming regions can benefit from information coming from the laboratory.

In my Ph.D. project, we studied the evolution in simulated space conditions of interstellar ice analogs subjected to UV irradiation. We used Fourier Transformed infrared (FTIR) spectroscopy, Temperature Programmed Desorption (TPD) analysis, and mass spectroscopy as analysis techniques.

In the first chapter, the theory of infrared (IR) and mass spectroscopy will be illustrated. In the first part of the chapter, we will start with the theory of IR reflectance spectroscopy and then pass specifically to FTIR spectroscopy. Similarly, in the second part of the chapter, we will start from the theory

that underlies mass spectroscopy and then move on to TPD analysis.

In the second chapter, we will describe the facilities present in our laboratory at the INAF Astrophysical Observatory of Arcetri. In the first section of the chapter, we will focus on one of the key points of the laboratory work, that is the preparation of the analog samples to be analyzed, i.e., iCOMs adsorbed on grains similar to interstellar ones. In the second part of the chapter, we will describe the specifications of the instruments used for IR reflectance spectroscopy and for mass spectroscopy, the principles of cryogenic and vacuum techniques to simulate the spatial conditions in terms of temperature and pressure, and the description of the Xenon lamp source used to simulate the radiation of Sun-like stars to process the analog samples.

The third chapter describes the first work of my project dedicated to a particular prebiotic molecule, formamide. The study of formamide was developed in two parts and types of measurements: photo-processing of icy samples of pure formamide and adsorbed on space relevant minerals investigated in situ by FTIR spectroscopy and thermal desorption of pure formamide ice and in the presence of grains, before and after UV irradiation.

Chapter four describes the second work of my Ph.D. dedicated to thermal desorption studies of other two iCOMs, acetaldehyde and acetonitrile, from micrometric grains of silicate olivine.

In the fifth chapter, we will investigate the role of UV photons irradiation on acetaldehyde and acetonitrile. Samples of pure acetaldehyde, pure acetonitrile, and mixtures were subjected to in-situ UV irradiation to study photolysis and the formation of more complex molecules.

Chapter 1

Infrared and Mass Spectrometry theory

1.1 Infrared reflectance spectroscopy

Infrared spectrum (IR) is the region of electromagnetic spectrum with frequencies lower than visible lights (VIS), wavelenghts above 0.7μm, and higher than radio waves, wavelenghts under 300 μm. The IR spectrum is in turn divided in three regions

1. Near Infrared (NIR), wavelenghts between 0.7μm and 5μm
2. Medium Infrared MIR, wavelenghts between 5μm and 25μm
3. Far Infrared FIR, wavelenghts between 25μm and 300μm

IR spectroscopy is an analytical technique based on the interaction between electromagnetic radiation and matter. The interaction between radiation and matter and the subsequent excitation of atomic vibrations determines the appearance of particular features in the IR spectrum. Through spectroscopic techniques, we study the spectrum of a given molecule, that is the intensity of the characteristic features of the molecule as a function of the wavelength. In classical physics, when a molecule is hit by infrared radiation, the energy yielded by the radiation itself is converted into vibrational energy. The vibrations of the molecular and mineral structure can range from the simple coupled motion of two atoms of a diatomic molecule to the more complex motion due to each atom in a large polyfunctional molecule or mineral structure (Bohren et al., 1983). The two basic ways the molecule can vibrate are by stretching (a rhythmic movement along the binding axis with the consequent increase or decrease of the interatomic distance) and

bending (due to a variation in the bending angle in the bonds with a common atom or to a movement of a group of atoms with respect to the rest of the molecule). In the case of bending vibrations, the movement can occur in the plane (vibrations in-plane: scissoring and rocking) or outside the plane (vibrations out-of-plane: wagging and twisting), see Figure 1.1.

The dipolar moment of the molecule is defined by $\bar{\mu}_d = q \cdot \bar{d}$, where q is the electric charge and $\bar{d}$ is the vector distance. The spectrum bands intensity depends on the value of the dipolar moment of the bond to which they refer. For example, the molecule of CO_2 has zero dipolar moment and the symmetrical stretching of the carbonyl bonds doesn't cause the absorption in the infrared since every dipolar moment associated with a C$\Longrightarrow$O bond is canceled by the other (the symmetrical vibration doesn't destroy the center of symmetry of the system). In this case, a passive IR absorption occurs. To have an active IR absorption, the dipolar moment of the molecule needs to be modified by the vibrations. Asymmetric stretching involves the appearance of a time-varying dipolar moment, i.e., absorption. As the dipolar moment varies, the absorption increases, i.e., the intensity of the molecule's spectrum bands increases (Fig. 1.2).

The IR spectrum of a molecule is obtained by plotting the intensity of absorption as a function of the wavelength. It is characterized by bands referable to specific functional groups that are part of the molecule itself. These bands describe the structure of the analyzed molecule. Hooke's law is the classical law that allows us to predict the frequency with which a certain functional group present in the molecule will be absorbed. If we consider two atoms linked together as a simple harmonic oscillator represented by two masses linked by a spring, we observe that:

- small balls are easier to move, so the frequency at which they oscillate is inversely proportional to their mass
- the stiffer the spring, the greater the frequency at which the oscillation will occur therefore, the frequency is directly proportional to the strength of the link

The Hooke's law is

$$\nu_{vibr} = \frac{1}{2\pi} \cdot \left(\frac{k}{\mu}\right)^{1/2}, \tag{1.1}$$

where

- $\mu = \frac{m_1 \cdot m_2}{m_1 + m_2}$ is the reduced mass,
- ν_{vibr} is the frequency at wich the oscillation occurs,

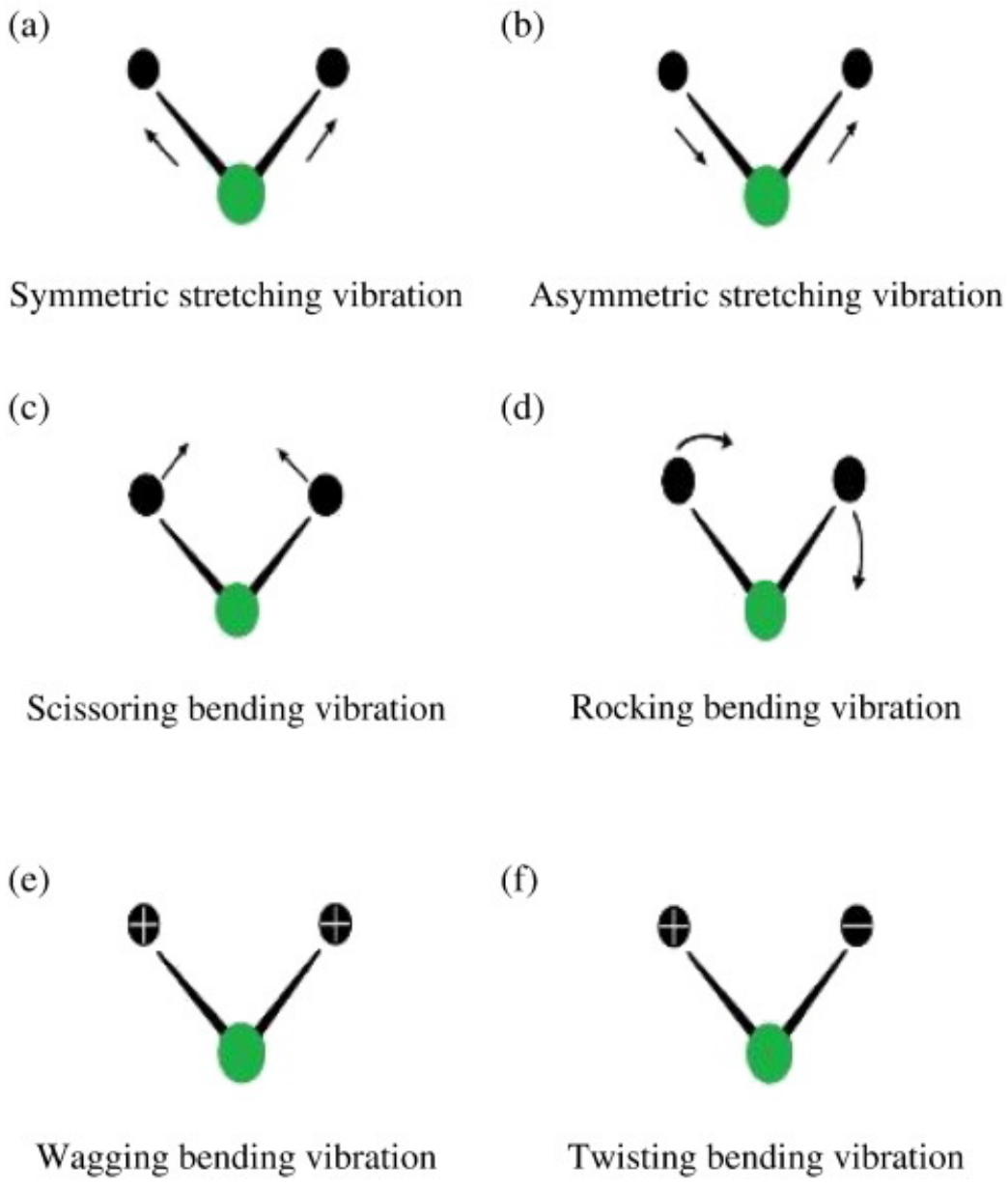

Figure 1.1: Stretching and bending vibrations (Hosein et al., 2017).

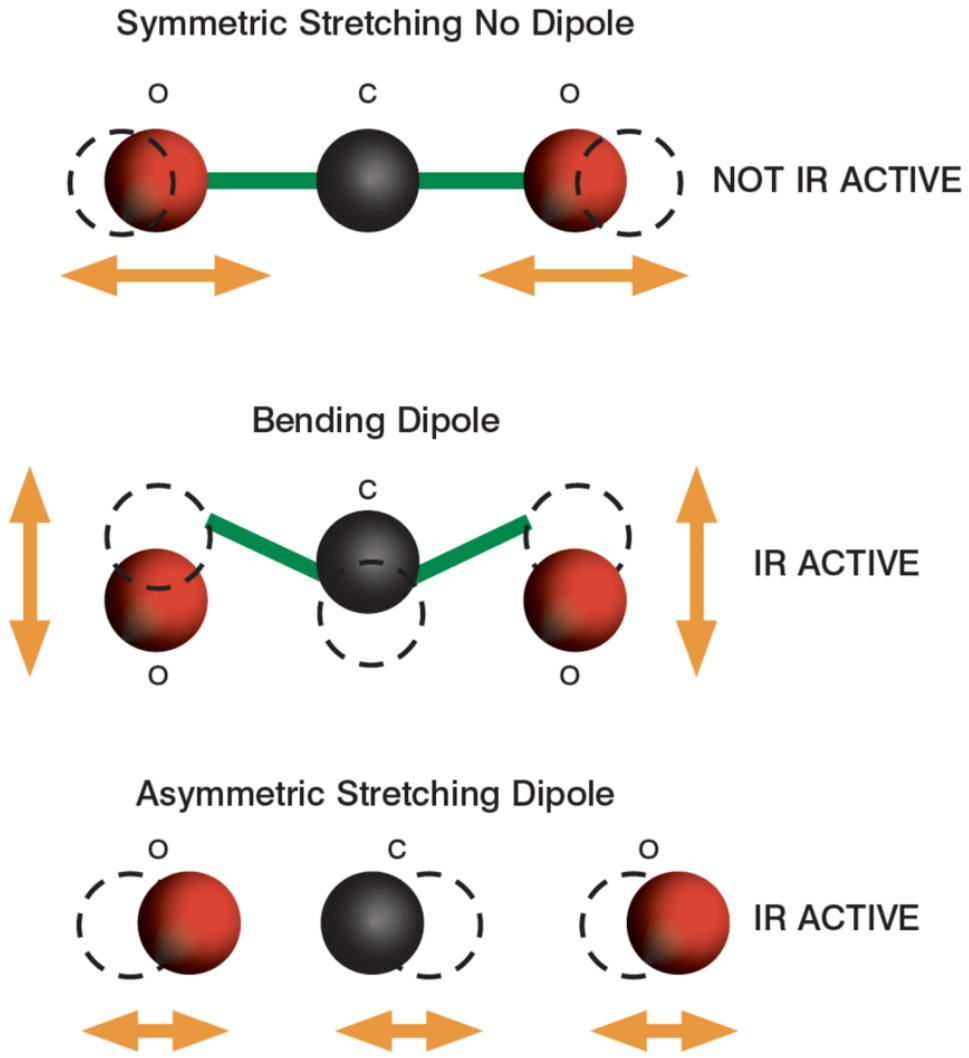

Figure 1.2: Sketch of active and passive IR vibration (courtesy of AWE International).

- k is the constant strength of the chemical bond.

The equation 1.1 tells us that oscillators made up of small masses oscillate at higher frequencies and that the atoms joined by a single bond vibrate at lower frequencies than those joined by double or triple bonds. When two oscillators share a common atom, as in the CO_2 molecule, there is a mechanical interaction between the two oscillators. During symmetrical stretching, an elongation and a contraction in phase occur: this does not cause a change in the dipolar moment of the oscillator and therefore it does not generate an active IR vibration. During the asymmetric stretching instead, two out-of-phase stretchings occur (one bond is stretched while the other is contracted): this causes a change in the dipolar moment, and therefore, it generates an active IR vibration, i.e., a variation in the oscillator absorption frequency. We use the three spatial coordinates x, y, and z to define the movement in space of each atom of a generic molecule made up of n atoms. Each atom, therefore, has three degrees of freedom and the entire molecule has 3n degrees of freedom. All possible movements of the molecule (translations, rotations, and vibrations) are counted in this value. The translational movements concern the entire molecule understood as a rigid body and can be described with the displacement of the barycenter along with the three coordinates: the molecule thus has three translational degrees of freedom. The rotational movements also occur around the three Cartesian axes, so the molecule has three degrees of freedom of rotation which are reduced to two for linear molecules. The vibrational degrees of freedom are the difference between the 3n total degrees and the translational and rotational degrees of freedom:

- vibrational degrees of freedom (non linear molecule)=3n-(3+3)
- vibrational degrees of freedom (linear molecule)=3n-(3 + 2)

IR spectrum appears as a sequence of absorption bands as a function of the wavelength or wavenumber (cm^{-1}). An IR absorption band is characterized by 3 parameters:

- the position of the band given by its maximum wavelength λ in μm or by the wavenumber ν in cm^{-1}. The maximum frequency ν depends on the constant strength of the chemical bond k, so the stiffer the bond, the greater the energy needed to amplify the vibrations, see 1.1 equation.
- The intensity of the band. This characteristic expresses the probability that the energetic transition from the ground state to the excited state will occur by the functional group that causes the absorption. The intensity depends on the variation of the dipolar moment.

- The shape of the band, that can be of two types: sharp and broad.

Studying an IR spectrum means studying a sequence of absorption bands. To interpret them, we can divide the spectrum into regions:

- the range of the spectrum with wavenumbers between 10000 - 4000 cm^{-1} is the region where the overtone bands are present. These bands are due to energetic transitions between the fundamental vibrational state and the second excited state and therefore prohibited by the first selection rule. Transitions of this type give rise to bands of low intensity, called harmonic bands or overtone bands. Since the energy difference between the two states is about double compared to the energy difference between the fundamental state and the first excited state, the harmonic bands are about twice the frequency of the normal bands originating from vibration. They are called overtones because they resonate outside the specific field of IR and so, they are multiples of other characteristic bands allowed by the selection rule.

- The range of the spectrum with wavenumbers between 4000 - 2700/2800 cm^{-1} is the region where the stretchings of the X——H bonds are present. To accurately locate a particular X——H bond in this region, it is necessary to take into account that as the atomic masses increase the absorption band shifts towards smaller wavenumbers, and that if the force between 2 atoms increases, the frequency of vibration increases, see equation 1.1.

- The range of the spectrum with wavenumbers between 2500-2000 cm^{-1} is the region where the stretchings of the triple bonds are present. Triple bonds absorb at higher wavenumbers than a double or single bond because the binding energy and consequently the k constant strength of the triple bond is greater than that of a double or single bond, see always the equation 1.1. In this region, bands related to alkyne (C≡≡C), nitriles (C≡≡N), and C≡≡O at 2140 cm^{-1} are present.

- The range of the spectrum with wavenumbers between 1900 - 1600 cm^{-1} is the region where the stretchings of the double bond are present. It is a narrow region, only 300 cm^{-1}, but it could be due to a large number of double bonds. In the double bond C==C, for example, the two carbon atoms do not have a great difference in electronegativity, but the dipolar moment will not be zero because the pair of electrons can generate oscillating electric fields. All other cases that fall within this range are characterized by a strong variation of the dipolar moment. Due to these variations, the bands in this area are very intense.

- The range of the spectrum with wavenumbers between 1500 and 1200 cm^{-1} is the region in which the C——O stretchings occur. In these regions, we find the absorptions related to the stretches of the functional groups C——O, C——N, C——C. The last ones are difficult to understand and often they resonate with the rest of the molecule and give rise to complex bands. Furthermore, a molecule deforms the bond angles by vibration as well as stretch along the deformations bonding. The absorptions due to these deformations generally fall at lower frequencies than stretching and they depend on the nature of the functional groups and on their position in the molecular skeleton. So in this region, we can find absorptions due to stretching, skeleton vibrations, and molecule deformations, which appear as peaks with different shapes and symmetries. Some characteristic peaks, such as those of CO and CN, will be recognizable by their intensity.

- The range of the spectrum with wavenumbers between 1300 - 900 cm^{-1} is the region of the fingerprints. In this region, the bands due to the stretching of the single X——Y bonds are present. This region does not correspond to a specific vibration of the molecule. The deformations interact with each other and combine giving rise to a series of bands that are precisely the fingerprint of the molecule.

The sample spectral properties can be investigated through different types of IR spectral investigation: reflectance, emittance, and transmittance.

Our work will focus on reflectance spectra properties, so now, we will show some quantitative considerations. First of all, we introduce the law of Lambert-Beer. When radiation with I_0 intensity crosses a medium of thickness l, part of the radiation will be absorbed by the medium itself and the transmitted radiation will have a residual intensity I_T. Lambert-Beer's law says that the transmittance of a pure sample of thickness l at wavenumber ν, $T(\nu)$, is the ratio between the intensity of transmitted radiation and the intensity of incident radiation on the medium:

$$T(\nu) = \frac{I_T}{I_0} = e^{-\alpha(\nu)l}, \tag{1.2}$$

where $\alpha(\nu)$ is the linear absorption coefficient at ν (it is a typical constant of the crossed medium and depends on the wavenumber ν).
$A(\nu)$ is the absorbance of the sample and it is defined as the opposite of the natural logarithm of transmittance; we can write the equation 1.2 as follows:

$$A(\nu) = \log_{10} \frac{1}{T(\nu)} = \frac{1}{\ln 10} \cdot \alpha(\nu) \cdot l = a(\nu) \cdot l, \tag{1.3}$$

where $a(\nu)$ is the absorptivity at ν.
If there is scattering from the sample, part of the incident radiation will be reflected. We can define the reflectance R as the ratio between the reflected intensity from the sample, $I_r(\nu)$, and the intensity of the incident radiation on the sample $I_0(\nu)$.

$$R(\nu) = \frac{I_r(\nu)}{I_0(\nu)} \tag{1.4}$$

Reflectance, absorbance, and transmittance are linked by the energy conservation as follows:

$$R(\nu) + A(\nu) + T(\nu) = 1$$

The absorption of radiation is regulated by the real and imaginary component of the complex refractive index

$$\bar{n}(\nu) = n(\nu) + i \cdot k(\nu),$$

where $k(\nu)$ is the imaginary refractive index, known as absorption index. For any material, the refractive index $n(\nu)$ is given by Snell's law. A few materials have no absorption in the MIR and NIR spectrum, so they are useful as windows in optical system for spectroscopy. For pure materials, $k(\nu)$ and the linear absorption coefficient $\alpha(\nu)$ defined in the equation 1.3 are linked by the following equation

$$k(\nu) = \frac{\alpha(\nu)}{4\pi \cdot \nu} \tag{1.5}$$

The refractive index changes across the absorption band and this variation is known as anomalous dispersion. Outside the regions of anomalous dispersion, n is fairly constant from VIS through MIR spectrum. Now, we will describe the measurement technique used to perform IR reflectance analysis.

1.1.1 Fourier-Trasform InfraRed spectroscopy (FTIR)

Fourier transform infrared spectroscopy (FT-IR) is an advanced technique compared to dispersion spectroscopy. Every single scansion radiation is recorded on the full spectral range unlike the dispersion spectrometer that acquires data on a small region (Fellgett's advantage) and a larger quantity of energy is acquired due to a bigger beam aperture (Jacquinot's advantage) (Griffiths et al., 2007).

Michelson Interferometer Many interferometers used for FTIR spectrometry are based on interferometer designed by Michelson in 1891 (Griffiths et al., 2007). This device can split an incident radiation beam into

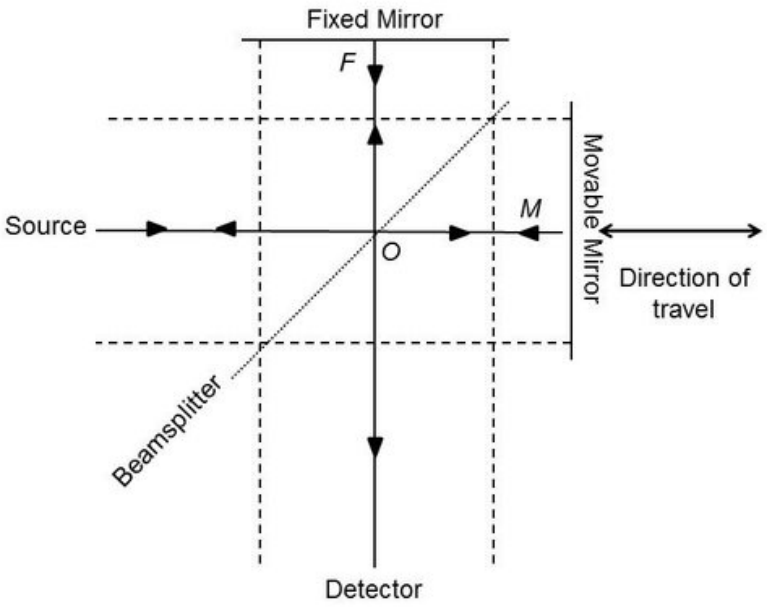

Figure 1.3: Michelson interferometer. The solid line is the median ray of the incident beam. The dashed lines are the extremes of the collimated incident beam (Griffiths et al., 2007).

two beams and then recombine them with a difference path. In this way, it creates a condition in which the interference between the two beams occurs. The variation of the beam intensity emerging from the interferometer as a function of the path difference is measured by a detector.

Figure 1.3 shows an example of Michelson Interferometer. Michelson interferometer consists of two perpendicular mirrors, one of which is fixed and the other can move along a direction that is perpendicular to its plane. The central part of the interferometer is a beamsplitter, a device where the collimated incident beam of radiation, coming from an external source, can be partially reflected to the fixed mirror (point F for the median ray) and partially transmitted to the movable mirror (point M). The two beams reflect on the respective mirrors and once they return to the beamsplitter, they interfere and are again partially reflected and transmitted. The instrument measures the intensity of the beam reaching the detector (Fig. 1.3). The

intensity of the beam reaching the detector depends on the difference in the path of the beam in the two arms of the interferometer. The intensity variation of the beams passing to the detector and returning to the source as a function of the path difference produces the spectral information in an FTIR spectrometer (Griffiths et al., 2007). The beam returning to the source is of no interest and usually, only the outgoing beam traveling in the direction perpendicular to that of the incoming beam is measured (in fact in Figure 1.3, the detector is located only in the direction perpendicular to that of the incoming beam). Both beams contain equivalent information. The reason for measuring only the output beam is the difficulty of separating the beam returning to the source from the incoming beam.

We can consider a monochromatic radiation source of wavelength λ_0 which produces a narrow and collimated beam. The wavenumber ν_0 is $\nu_0 = 1/\lambda_0$ and $I(\nu_0)$ is the source intensity at this wavenumber. We assume the ideal beamsplitter, i.e., there is no absorption, and the reflected and the transmitted beam is exactly fifty-fifty. The path difference between the two beams that travel to fixed and movable mirror and then back to the beamsplitter is 2(OM-OF) (as visible in Figure 1.3). This optical path difference (OPD) is called retardation and is indicated by δ. The retardation is the same for all parallel input beams, so this description applies also to a beam not infinitely narrow but collimated. When the two mirrors are equidistant from the beamsplitter, the retardation is zero, $\delta = 0$. In the zero path difference (ZPD) case, the two beams directed towards the detector are in phase on recombination at the beamsplitter. They interfere constructively and the intensity of the beam that reaches the detector is the sum of the intensities of the beams passing to the fixed and movable mirrors. All the radiation from the source reaches the detector and none returns to the source. A beam reflected by a mirror at normal incidence undergoes a phase change of 180°, a beam reflected by an ideal beamsplitter undergoes a phase change of 90°, while the phase of the transmitted beam is unchanged. The beam reaching the detector from the fixed mirror undergoes a total phase change of 270°, similar to the beam reaching the detector from the moving mirror. The two beams are therefore in the recombination phase at the beamsplitter and interfere constructively. On the other hand, the beam returning to the source from the fixed mirror undergoes a phase shift of 90° for the first reflection from the beamsplitter, 180° for the reflection from the mirror, and 90° for the second reflection from the beamsplitter, for a total change of 360°. The beam traveling towards the moveable mirror and then returns to the source instead undergoes a phase change of 180° due to the reflection from the mirror and does not undergo phase change for both transmissions through the beamsplitter. The two beams are 180° out of phase and they interfere in a

destructive way. So in the ZPD case, the total power of the incident beam is transmitted to the detector and no radiation returns to the source. When the movable mirror is localized at a distance $\lambda_0/4$, $\delta = \lambda_0/2$, i.e., the retardation is non zero. In this case, the two beams are out of phase on recombination at the beamsplitter, so they interfere destructively and all the radiation returns to the source and none reaches the detector. If the movable mirror is localized at a distance $\lambda_0/2$, the total retardation becomes $\delta = \lambda_0$. The two beams are once more in phase on recombination at the beamsplitter and we have a constructive interference for the beams that travel to the detector. If the movable mirror is moved at a constant velocity, the signal at the detector will have a sinusoidal shape: it will be maximum when the retardation is an integral multiple of λ_0. The intensity of the beam at the detector as a function of retardation, $I'(\delta)$, is given by the following expression

$$I'(\delta) = 0.5 \cdot I(\nu_0) \left[1 + \cos\left(\frac{\pi \cdot \delta}{\lambda_0}\right)\right] \tag{1.6}$$

The 1.6 equation displays that the intensity is composed by a constant component, $0.5 \cdot I(\nu_0)$, and by a modulated component, $0.5 \cdot I(\nu_0) \cdot \cos(2\pi \cdot \delta)$. Only this last component is important in spectrometry and it is generally called *interferogram* $I(\delta)$. So, the interferogram from a monochromatic source is given by

$$I(\delta) = 0.5 \cdot I(\nu_0) \cdot cos(2\pi\nu_0\delta) \tag{1.7}$$

The signal amplitude measured at the detector also depends on the efficiency of the beamsplitter (which is generally not ideal). The non-ideality of the beamsplitter is taken into account by multiplying $I(\nu_0)$ by a wavenumber-dependent factor less than one that represents the relative beamsplitter efficiency. Furthermore, the IR detectors do not have a uniform response at all wavenumbers. Therefore, the amplitude of the interferogram observed after detection and amplification is proportional to the intensity of the source, to the beamsplitter efficiency, to the detector response ($H(\nu_0)$), and to the amplifier characteristics ($G(\nu_0)$ in V/W). The final signal $S(\delta)$ in V is given by:

$$S(\delta) = 0.5 \cdot H(\nu_0) \cdot G(\nu_0) \cdot I(\nu_0) \cdot cos(2\pi\nu_0\delta) = B(\nu_0) \cdot cos(2\pi\nu_0\delta), \tag{1.8}$$

where $B(\nu_0)$ is the source intensity at a wavenumber ν_0 modified by the instrumental characteristics:

$$B(\nu_0) = 0.5 \cdot H(\nu_0) \cdot G(\nu_0) \cdot I(\nu_0)$$

Mathematically, the signal $S(\delta)$ is the cosine Fourier transform of $B(\nu_0)$. The spectrum is calculating from the interferogram by computing the cosine

Fourier transform of $S(\delta)$ which gives the name to this spectrometric techniques: **Fourier transform spectrometry** (Griffiths et al., 2007). When the source is a continuum, the interferogram is represented by the integral

$$S(\delta) = \int_{-\infty}^{+\infty} B(\nu) \cdot cos(2\pi\nu\delta) d\nu \tag{1.9}$$

Since $S(\delta)$ is an even function, we can write

$$B(\nu) = 2 \cdot \int_{0}^{\infty} S(\delta) \cdot cos(2\pi\nu\delta) d\delta \tag{1.10}$$

The equation 1.10 shows that theoretically, it is possible to measure the spectrum from zero to $+\infty$ in cm^{-1} with an infinitely high resolution by varying δ from zero to $+\infty$ cm, i.e., by moving the mirror of the interferometer at an infinite distance. δ limited is responsible for a finite resolution because the spectral resolution depends on the maximum delay $\Delta\nu = \frac{1}{\delta_{max}}$.
Fast Fourier Transform (FFT) is an algorithm studied by Cooley and Tukey (Griffiths et al., 2007). This algorithm requires much less computation than the classic Fourier transform. The following expression is the Discrete Fourier Transform (DFT):

$$B(r) = \sum_{k=0}^{N-1} S_0(k) \cdot e^{-i2\pi rk}, \tag{1.11}$$

where $r = 1, 2, ..., N-1$. N is the number of points of the interferogram, and $B(r)$ is the spectrum at a discret wavenumbers r. If we define $W = e^{-i2\pi/N}$, the equation 1.11 becomes

$$B(r) = \sum_{k=0}^{N-1} S_0(k) \cdot W^{rk} \tag{1.12}$$

FFT algorithm is based on the idea that the equation 1.12 can be expressed in general matrix form and this matrix can be factored in a way that will reduce the overall number of computations. This algorithm is general and can be applied to any Fourier transform. The computation is simplified if N is a base 2 number (for example $N = 2 \cdot \alpha$), with α an integer positive (we can try with $\alpha = 2$ and $N = 4$). In general, FFT needs $N/2$ complex multiplications, while DFT needs N^2 complex multiplications.

1.2 Mass spectroscopy

The second analysis technique on which my Ph.D. project is based is mass spectrometry and Temperature Programmed Desorption analysis.

Mass spectrometry is a technique based on the ionization of a molecule and its subsequent fragmentation into ions of different mass/charge ratio (m/z). Unlike IR spectroscopy, mass spectrometry is a destructive method of analysis and it is not based on the interaction between radiation and matter. During the mass spectrometry experiment, the molecule is ionized in the gas phase by expelling an electron. The molecular ion, that has been formed, partly fragments giving origin to molecules and neutral radicals and partly fragments giving origin to cations and radical cations (fragment ions). The ions that originate by fragmentation (cations and radical cations) are separated and discriminated based on their mass/charge ratio and are detected by a detector. In fact, the ions, once produced, pass through a trajectory defined by a pair of slits between which a potential difference V is applied. At the exit from the second slit, the ions with the same charge q have a kinetic energy equal to:

$$E_c = \frac{1}{2} \cdot m \cdot v^2 = q \cdot V, \tag{1.13}$$

where the kinetic energy is independent of their mass. The ion beam is therefore isoenergetic (the ions have the same energy).

Now, we will describe briefly the theory behind the operating principle of a mass spectrometer and the ability to discriminate ions based on their mass/charge ratio. The ions enter a region in which a uniform magnetic field B acts. The ions are subjected to the Lorentz force equal to:

$$\vec{F_L} = q \cdot (\vec{v} \times \vec{B}) \tag{1.14}$$

The charged particle q describes a trajectory whose curvature radius is obtained by equating the Lorentz force with the centripetal force. The curvature radius obtained is:

$$r = \frac{mv}{qB} \tag{1.15}$$

The mass m, the field B, and the charge q are constant. Furthermore, the velocity v does not change in modulus since the force is exclusively centripetal and therefore also the curvature radius is constant, that is, the trajectory described by the particle is an arc of circumference. With the same charge and therefore kinetic energy, different speeds correspond to different masses, and therefore different radii. The mass/charge ratio depends on the measurement of r, note the magnetic field and the accelerating potential difference.

The mass spectrometry experiment, therefore, consists of the ionization of molecules in the gas phase, in the separation of the different ions produced based on their mass/charge ratio, and in their detection. The result of the

experiment is the mass spectrum. It describes the relative abundance of ions versus their ratio m/z. This technique allows to measure the molecular masses and to obtain specific fragmentation profiles for each compound, of which they constitute a fingerprint.

The sample introduction into the ionization chamber can be done both in the solid state and in the liquid or gaseous state (as in our experiments), using a system of valves that allow access to the ionization chamber without it coming into contact with external. The ionization can occur through the expulsion of electrons, or through protonation, deprotonation, and cationization. With the expulsion of electrons, a radical-ion is generated (our laboratory case). The radical-ion is an unstable species that can easily undergo fragmentation. With protonation and deprotonation, a pseudomolecular ion is instead generated. The ionization technique of our spectrometer is the electron impact ionization (E.I.). The ion source is an electron impact ionizer with twin-oxide-coated iridium filaments. The filament emits a beam of electrons which are accelerated towards an anode placed on the opposite side of the filament with an energy of 70 eV. When these electrons impact a molecule, they transfer their energy to it, causing the expulsion of an electron and therefore the formation of a radical cation (molecular ion). Since the energy required to ionize an organic molecule is about 13-14 eV, the cation radicals are produced at a very high vibrational energy that can cause their fragmentation with the formation of a radical and a cation. The cations and radical cations are accelerated towards a series of plates with increasing positive potential, called accelerator plates. The ions undergo an acceleration proportional to the potential V of the accelerator plates and acquire kinetic energy given by the formula 1.13. The flow of ions enters the analyzer, i.e., in a device capable of separating the ions according to their m/z ratio, (see equation 1.15). There are several types of analyzer. Our mass spectrometer is a Quadrupole mass spectrometer. A mass analyzer is a mass filter capable of transmitting only the chosen ion. This type of analyzer is the most used in mass spectrometers for routine analysis and it has unit resolution. It consists of four cylindrical metal bars, about 20 cm long, which describe the path of the ions coming from the ionization chamber and directed to the detector. The bars are kept at an oscillating electromagnetic potential: when the two vertical bars have positive potential, the horizontal ones have negative potential. The electrons are accelerated by the accelerator plates and enter the tunnel delimited by the bars, repelled by the positive poles and attracted by the negative ones. Due to the quadrupole oscillation, the ions take a zigzag trajectory and end up discharging on one of the bars, except for those which, for a certain oscillation frequency, have kinetic energy such that the motion becomes sinusoidal and manage to exit the tunnel and enter the de-

tection system (photomultiplier) (see e.g., Rubinson et al. 2002). Our mass analyzer is a triple quadrupole (HAL 3F RC Quadrupole mass spectrometer, whose specifications are given in the next chapter where we will describe the instruments present in the laboratory). In this configuration, the first and third quadrupoles act as mass filters, while the central quadrupole, filled with an inert gas, acts as a collision cell. An electronic multiplier consisting of a series of cascaded electrodes is commonly used as a detector. When an ion arrives on the first electrode, it emits a beam of electrons that hit the second electrode, which in turn emits a greater quantity of electrons and so on. The result is a strong amplification of the signal which is then digitized and processed by the spectrometer software for the elaboration of the mass spectrum. Our system is supplied with MASsoft Professional software.

1.2.1 Temperature-Programmed Desorption (TPD)

Through mass spectroscopy, we performed Temperature-Programmed Desorption (TPD) experiments. Temperature programmed desorption is a method to observe in the gas phase molecules desorbed from a surface when the surface temperature rises. This experimental technique is also referred to as thermal desorption spectroscopy when the experiments are performed using well-defined surfaces of monocrystalline samples in a continuously pumped ultra-high vacuum (UHV) chamber (e.g., O'Connor et al. 2013). Once the molecules are deposited on a surface, they adsorb on it and form a bond with the surface itself. The binding energy varies according to the surface and the adsorbed species, adsorbate. If the surface is heated, the energy transferred to the adsorbed species will cause its desorption. The temperature at which the desorption occurs is the desorption temperature, T_{des}. The figure describing the thermal desorption of the adsorbed species with increasing temperature is called the TPD curve and contains information on the desorption temperature and energy, E_{des}.

The sample is heated with a constant heating rate h_r given by

$$h_r(t) = \frac{dT}{dt}. \tag{1.16}$$

Once the molecules are desorbed as the temperature rises, they enter the mass spectrometer and are discriminated on the basis of their m/z ratio. Then, the TPD curve describes the signal detected by the mass spectrometer as the temperature increases for a given value of m/z. So, the TPD experiments observe the mass of the desorbed molecules. In this way, they show the species adsorbed on the surface and allow us to recognize the different adsorption conditions through for example the differences between the

T_{des} of the molecules that desorb from different sites on the surface. The TPD curves also give information on the amount of molecules adsorbed on the surface by the intensity of their peak.

In the next paragraphs, we will briefly address first the theory concerning the adsorption and desorption of an adsorbate from an adsorbent surface and then the theory of thermal desorption. We will then describe in detail the TPD curves and how to quantitatively interpret and analyze them.

Adsorption and Desorption Adsorption between molecular species (adsorbate) and a surface occurs when an attractive interaction between the adsorbate and the surface is strong enough to overcome the disordering effect of thermal movement. As early as 1932, Lennard-Jones described that two types of adsorption can occur: physisorption and chemisorption (Lennard-Jones 1971). In the first case, the attractive interaction is the result of van-der-Waals forces. Physiosorptive bonds are characterized by dissociation energies below about 50 kJ/mol. In the second case, however, the overlap between the molecular orbitals of the adsorbate and the surface atoms allows the formation of chemical bonds, with dissociation energies higher than 50 kJ/mol. The chemisorption is an activated process, i.e., the formation of a chemisorptive bond requires the overcoming of an activation barrier. Figure 1.4 shows the curves of the potential energy V as a function of the distance z on a substrate surface. The three panels a, b, and c respectively describe the formation of a weak van-der-Waals bond with a depth of 20 Mev, the formation of a strong chemical bond with energies on the order of electron volts, and the transition from physisorption to chemisorption. Panel c displays the initial appearance of a weak van-der-Waals bond followed by a transition that may show a high (black curve), medium (green and red curves), and low (blue curve) energy barrier. A molecule on the surface can immediately chemisorb if its thermal energy is sufficient to overcome the energy barrier of the green potential curve. If a stronger energy barrier (black curve) occurs, the thermal excitation must increase its energy to form a chemical bond (Huber et al. 2019). Molecular chemisorption involves the weakening of intramolecular bonds and often leads to the dissociation of the adsorbed molecule. The adsorption of oxygen molecules to metal surfaces at room temperature is an example of activated dissociative chemisorption (e.g., Schroeder et al. 2002). In Figure 1.5, a schematic diagram of the potential for activated dissociative adsorption of a diatomic molecule X_2 is shown. On the abscissa axis, the z trajectory of the molecule along the metal surface is reported. On the order axis, we find the potential energy of the entire system. The physisorption potential describes the interaction between the metal and the undissociated

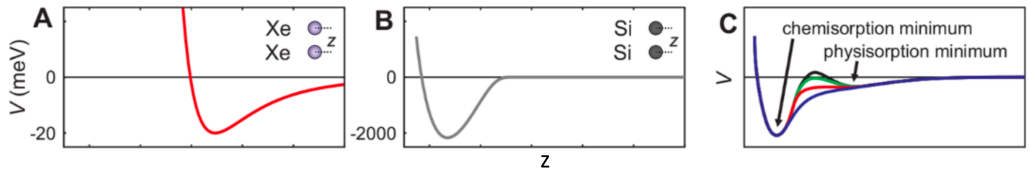

Figure 1.4: The figure shows the potential curves as a function of the distance z. The three panels a, b, and c respectively describe the formation of a weak van-der-Waals bond, the formation of a strong chemical bond, and the transition from physisorption to chemisorption after the overcoming of a high (black curve), medium (green and red curves), and low (blue curve) energy barrier (Huber et al., 2019).

molecule (M + X_2), while the chemisorption potential describes the interaction between the metal and the molecule dissociated into single atoms (M + 2X).

Various reactions can occur on the grain surface. In Figure 1.6, the Eley-Rideal mechanism and the Langmuir-Hinshelwood mechanism are shown. In the Langmuir mechanism, no chemical bonds occur between the adsorbate and the surface. The mechanism is regulated by van-der-Waals forces, so the adsorbed atom is able to move on the grain surface (surface migration). During its residence time on the grain surface, it can interact with another atom and form a molecule; if the temperature exceeds a threshold value, the molecule evaporates and back to the gas phase: desorption process.

Desorption is the release of a particle from the surface in the gaseous phase and occurs when an equilibrium condition is altered. The equilibrium between adsorption and desorption is defined as a constant ratio between the number of adsorbed particles, N_{ads}, and the number of adsorption sites, N_{surf}, available on the surface (surface coverage $\theta = N_{ads}/N_{surf}$). The condition for the chemical equilibrium between adsorbate and gas-phase particles is given by the equality of the chemical potential of the particles in both phases, i.e., $d\mu_{ads} = d\mu_{gas}$.

The adsorption isotherm describes the variation of adsorption (the surface coverage over the sample) as a function of the gas pressure. The Langmuir adsorption isotherm is based on the following assumptions (e.g., Langmuir 1918, Schroeder et al. 2002):

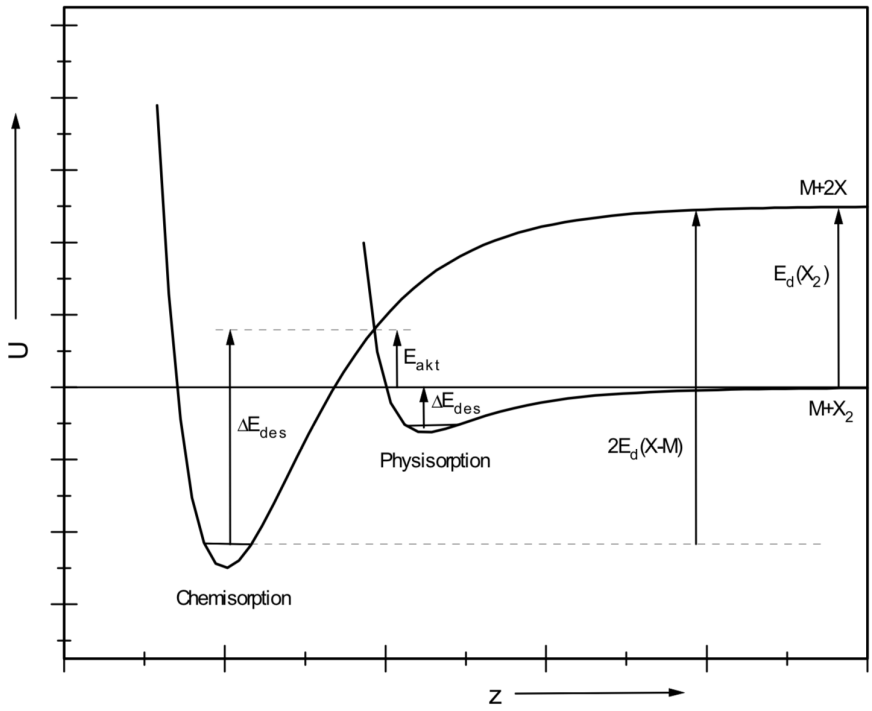

Figure 1.5: Potential curves for the activated dissociative adsorption of a diatomic molecule X_2 on a substrate surface along the z trajectory (Schroeder et al., 2002).

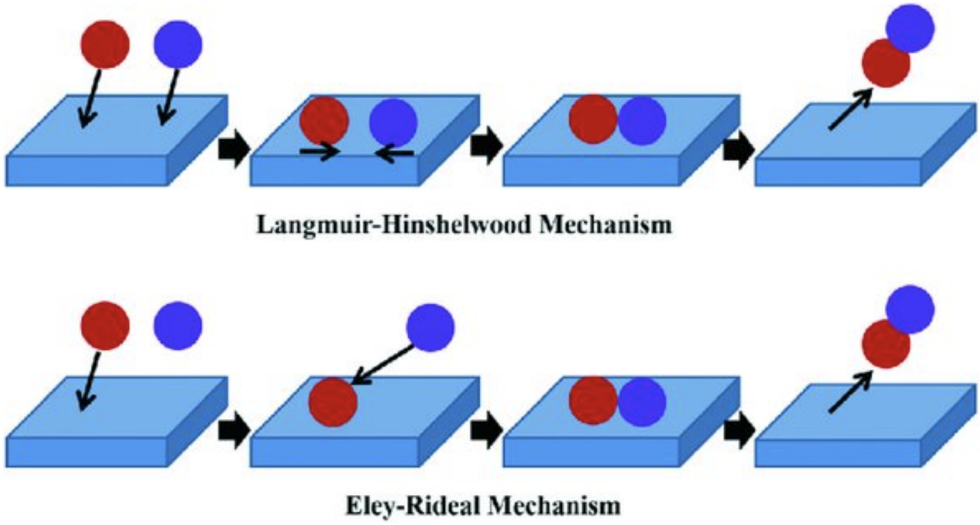

Figure 1.6: Langmuir-Hinshelwood mechanism (above) and Eley-Rideal mechanism (Mahata et al., 2019).

- adsorption is localized, i.e., the adsorbed particles are immobile;
- the substrate surface is saturated when the $\theta = 1ML$ (monolayer), i.e., when all adsorption sites are occupied;
- all the adsorption sites are of equal size and shape;
- there are no interactions between the adsorbed particles;
- there is a dynamic equilibrium between adsorbed gaseous molecules and the free gaseous molecules:

$$A(g) + B(s) \underset{Desorption}{\overset{Adsorption}{\rightleftharpoons}} AB,$$

  where

  - A(g) is the unadsorbed gaseous molecule,
  - B(s) is the unoccupied metal surface,
  - AB is the adsorbed gaseous molecule.

The adsorption and desorption rates are given by:

$$r_{ads}(\theta) = A_m \cdot P \cdot (1-\theta)^m$$

$$r_{des}(\theta) = B_m \cdot \theta^m,$$

where m = 1, 2 and P is the pressure. From the dynamic equilibrium condition ($|r_{ads}| = |r_{des}|$), we obtain the following expression for the surface coverage:

$$\theta_m = \frac{\left(\frac{A_m}{B_m} \cdot P\right)^{1/m}}{1 + \left(\frac{A_m}{B_m} \cdot P\right)^{1/m}}.$$

The condition $m = 1$ describes a first order rate law for adsorption and desorption, while $m = 2$ describes the second order and shows the dissociative adsorption and recombinant desorption of diatomic molecules.

TPD curves and the Polanyi-Wigner equation In a TPD experiment, the molecules are deposited in a UHV chamber (P$\sim 10^{-10}$mbar) on a surface. Once the surface is heated with a constant heating rate h_r given by the equation 1.16, the molecules desorb, enter the mass spectrometer, and are discriminated by their m/z ratio. For a given mass, the TPD curve is the figure describing the thermal desorption which is generally analyzed using the Polanyi-Wigner equation (e.g., Attard et al. 1998):

$$r_{des} = -\frac{d\theta}{dT} = \frac{A}{h_r} \cdot \theta^m \cdot e^{-E_{des}/K_b T}, \tag{1.17}$$

where

- A is the pre-exponential factor in $\sec^{-1}$,
- θ^m is the surface coverage of order m,
- E_{des} is the desorption energy,
- K_b is the Boltzmann's constant.

In Figure 1.7, we can see an example of a TPD curve. A TPD curve and the Polanyi - Wigner equation give us information on the desorption rate, r_{des}, and on the desorption energy, E_{des} (see equation 1.17).

Now, we will briefly outline the steps to get the Polanyi - Wigner equation. The principle of microscopic reversibility requires that a reaction goes

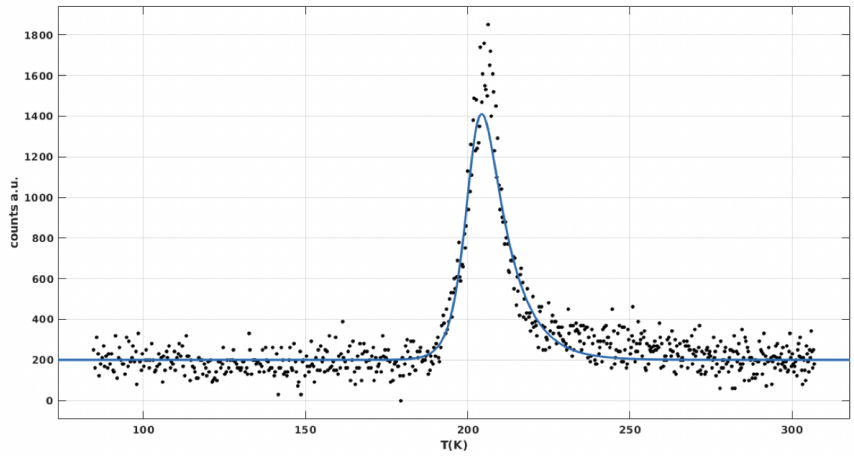

Figure 1.7: The black dots represent an example of a TPD curve obtained in the laboratory. In the graph, we report the temperature T(K) with respect to the signal detected by the mass spectrometer for a determined value of m/z as the temperature increases. The data are fitted using the Polanyi - Wigner equation (equation 1.17).

through the same states regardless of whether it proceeds forward or backward. So, adsorption and desorption can be described by the same rate equation. The desorption rate is usually written as a rate law of mth order:

$$r_{des} = -\frac{d\theta}{dt} = K_d \cdot \theta^m, \tag{1.18}$$

where

1. θ is the surface coverage,
2. K_d is the desorption rate constant,
3. m is the kinetic desorption order.

Adsorption is an activated process that obeys the Arrhenius equation:

$$K_d = A \cdot e^{E_{des}/K_b T}, \tag{1.19}$$

where A is the inverse of a time and it is the pre-exponential factor. By replacing this expression of the Arrhenius equation (equation 1.19) in the adsorption rate equation (equation 1.18), we obtain the following equation which describes the activation desorption energy E_{des}:

$$r_{des} = -\frac{d\theta}{dt} = A \cdot \theta^m \cdot e^{-E_{des}/K_b T}. \tag{1.20}$$

Usually, TPDs are run with a linear heating ramp, h_r:

$$T(t) = T_0 + h_r \cdot t,$$

therefore, deriving respect to time:

$$\frac{dT}{dt} = h_r.$$

So, we can obtain the Polanyi - Wigner equation (1.17) by writing the 1.20 equation as follows:

$$r_{des} = -\frac{d\theta}{dT} = \frac{A}{h_r} \cdot \theta^m \cdot e^{-E_{des}/K_b T}.$$

The shape of the TPD curve changes as a function of the kinetic desorption order m.

- At the zero-order kinetic, $m = 0$, the Polanyi - Wigner equation (1.17) becames

$$r_{des} = \frac{A}{h_r} \cdot e^{-E_{des}/K_b T}.$$

The zero-order kinetic desorption describes the multilayer desorption. The equation shows that there is no link between the desorption rate and the surface coverage. Figure 1.8 a) shows that the peak of the curve shifts to higher temperatures as the surface coverage increases. This trend is typical of multilayer desorption. The supply of deposited particles is theoretically unlimited, there is in fact no dependence on surface coverage, and the leading edges are common.

- At the first-order kinetic, $m = 1$, the 1.17 equation becames

$$r_{des} = \frac{A}{h_r} \cdot \theta \cdot e^{-E_{des}/K_b T}.$$

The first-order kinetic desorption describes unimolecular desorption, i.e., a molecule adsorbs and then desorbs without dissociating. Figure 1.8 b) displays that the position of the desorption peak is independent of the surface coverage. The peaks are asymmetrical with an ascending leading edge.

- At the second-order kinetic, $m = 2$, the 1.17 equation becames

$$r_{des} = \frac{A}{h_r} \cdot \theta^2 \cdot e^{-E_{des}/K_b T}.$$

The second-order kinetic desorption describes the recombinative desorption, i.e., the molecule adsorbs, dissociates on the surface, and then desorbs by recombining. The equation shows that the desorption rate follows θ^2 and Figure 1.8 c) shows that the peak position shifts to lower temperatures with increasing the surface coverage. From the figure, we can see symmetric peak shape and common trailing edges (Ranke 2005).

The TPD curves provide information on the desorption rate and desorption energy. If we write the Polanyi-Wigner equation 1.17 in logarithmic form, we find:

$$\ln(r_{des}) = \ln\left(\frac{A}{h_r} \cdot \theta^m\right) - \frac{E_{des}}{K_b T}, \tag{1.21}$$

if we plot $\ln(r_{des})$ as a function of $1/T$, we obtain information on the desorption energy. The slope of the curve is relative to E_{des} and the intercept is correlated to A.

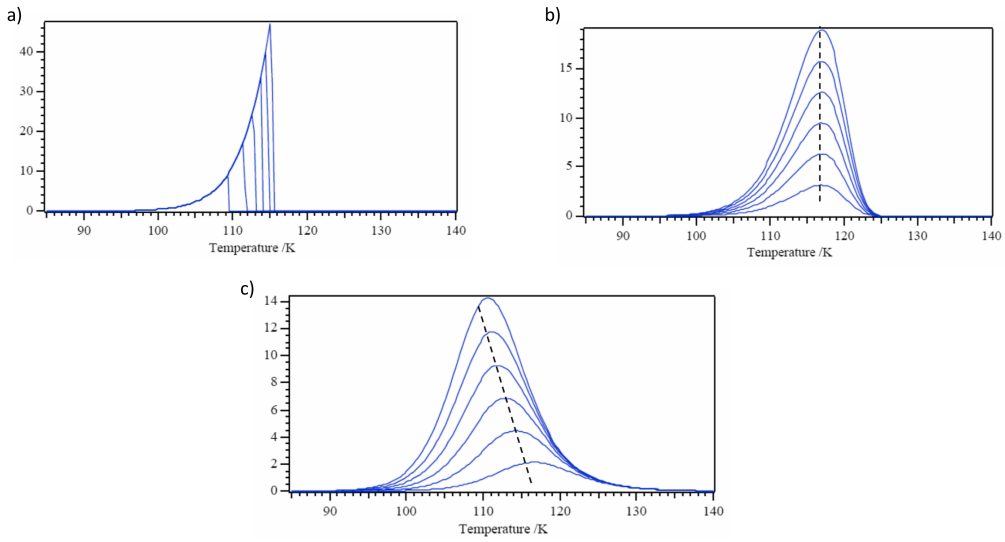

Figure 1.8: The figure shows how the shape of the TPD curves changes as a function of the kinetic order of desorption. The three panels a, b, and c respectively describe the zero, first, and second order of desorption.

Redhead's analysis The desorption energy E_{des} can be calculated starting from the Polanyi-Wigner equation also through the Redhead's analysis (e.g., Redhead 1962). If we consider the Polanyi-Wigner equation 1.17, the temperature has a maximum, T_{max}, when the following condition holds:

$$-\frac{d\theta^2}{dT^2} = 0. \tag{1.22}$$

If we derive the Polanyi-Wigner equation (1.17) and use the 1.22 condition, we find a relationship between T_{max}, the heating rate h_r, and the energy E_{des} (Redhead 1962):

$$\frac{E_{des}}{K_b \cdot T_{max}^2} = \frac{A}{h_r} \cdot m \cdot \theta^{m-1} \cdot e^{-E_{des}/K_b T_{max}} \tag{1.23}$$

For the first order of desorption $m = 1$, it follows:

$$\frac{E_{des}}{K_b \cdot T_{max}^2} = \frac{A}{h_r} \cdot e^{-E_{des}/K_b T_{max}} \tag{1.24}$$

In logarithmic form, the equation becomes:

$$\ln\left(\frac{E_{des}}{K_b \cdot T_{max}}\right) = \ln\left(\frac{A \cdot T_{max}}{h_r}\right) - \frac{E_{des}}{K_b \cdot T_{max}}$$

$$E_{des} = K_b \cdot T_{max} \cdot \left[\ln\left(\frac{A \cdot T_{max}}{h_r}\right) - \ln\left(\frac{E_{des}}{K_b \cdot T_{max}}\right) \right] \tag{1.25}$$

The Redhead approximation is to neglect the second natural log which is relatively small (e.g., Redhead 1962). E_{des} is therefore linearly correlated with T_{max} and this is useful for estimating E_{des} with a single TPD spectrum. Furthermore, the equation 1.24 can be written:

$$\ln\left(\frac{h_r}{T_{max}^2}\right) = -\frac{E_{des}}{K_b \cdot T_{max}} + \ln\left(\frac{A \cdot K_b}{E_{des}}\right)$$

If we plot h_r/T_{max}^2 as a function of $1/T$, we obtain a graph where E_{des} can be derived from the slope of the curve and A from the intercept.
On the other hand, for the second desorption order, the equation 1.24 becomes:

$$\ln\left(\frac{h_r}{T_{max}^2}\right) = -\frac{E_{des}}{K_b \cdot T_{max}} + \ln\left(\frac{A \cdot K_b \cdot \theta(0)}{E_{des}}\right),$$

where it has been taken into account that at the second order, the peaks are symmetrical and, therefore, the following condition holds: $\theta(T_{max}) = \theta(0)/2$.

Chapter 2

Astrophysics in laboratory

Laboratory study is a powerful and fundamental tool in every scientific field to understand natural processes through increasingly complex analysis carried out in a controlled environment. From this point of view, laboratory astrophysics is a very special branch of science: the analysis and direct verification of an astrophysical process is often an inaccessible tool due to the very nature of the phenomena dealt with. Even in the case of the study of organic molecules detected in space, where direct sample analysis is possible, laboratory analysis of analog samples remains an extremely powerful tool to understand data obtained from large radio and millimeter telescopes and from space missions.

Through laboratory works, we can study the chemical and physical properties of prebiotic molecules, their interaction with mineral surfaces at high (500 K) and cryogenic (20 K) temperatures, and their degradation driven by UV photochemical processing. A proper laboratory setup with simulated space conditions is needed to obtain results that best match the physical properties found in space to correctly interpret incoming data from the space.

In the first part of this chapter, we will show the facilities present in the laboratory and we will discuss one of the key points of the laboratory work, that is the analog samples preparation to be analyzed. In the second part of the chapter, we will describe the experimental setup used for the research and experiments carried out in three years of Ph.D. We will present the instruments used for the IR reflectance spectroscopy and for the mass spectrometry. Then, we will discuss the principles of vacuum and cryogenic techniques and we will present a description of the Xenon lamp used to simulate the radiation of Solar-type stars.

2.1 Astrobiology laboratory and facilities

2.1.1 Samples preparation

One of the key points of the laboratory work is the preparation of the analog samples to be analyzed.

We will illustrate how the sample set was obtained, starting from the selection of grain sizes and applying procedures for cleaning of organic contaminants. The procedure for obtaining the final samples is mainly based on two aspects: the mineral grinding to obtain grains of different sizes and the cleaning procedure to remove any organic contaminants.

Grinding Purchased minerals are natural crystalline forms, but to simulate interstellar analog dust, we need to obtain micrometer size grains. So, to obtain substrate of suitable dimensions, terrestrial bulk mineral was first ground using a Retsch Planetary Ball Mill PM100 with an agate jar and spheres. Crushing was performed with a grinding time of 10 minutes with a rotation speed of 450 rpm (round per minute); the rotation direction was inverted every two minutes. Finally, the mineral grains were separated according to their size by a Retsch Vibratory Sieve Shaker AS200. Through different sieves, we selected grains in variable dimensions: grains smaller the 20 μm, between 20 μm and 50 μm, between 50 μm and 100 μm, and between 100 μm and 200 μm. To select micrometric grains, two procedures were adopted: dry sieving to select grains with size d<20 μm and then a methanol sedimentation procedure to select grains with even smaller dimensions. The use of methanol as a solvent is justified by its high volatility, but also because it is a polar solvent able to remove organic contamination from the natural mineral. With sedimentation, grains with dimensions d<5 μm were selected. The grain size measurement was carried out with the Bruker Hyperion 1000 microscope.

Before the washing cycle, the minerals were characterized by FTIR spectroscopy. Through the mineral spectra, we can identify the presence of bands due to organic contaminants in the spectral region between 3300 and 2900 cm^{-1} due to stretching vibrational mode of functional group CH of alkene, alkane, alkyne, and aromatic compounds.

Washing cycle To remove the organic contaminants, three different types of washing cycles were carried out with different types of solvents: ddH_2O, ultra-purified H_2O, and methanol CH_3OH (MeOH). All the washing cycles were separated by centrifugation technic to divide the mineral pellet from the used solvent supernatant. All supernatants have been preserved for further

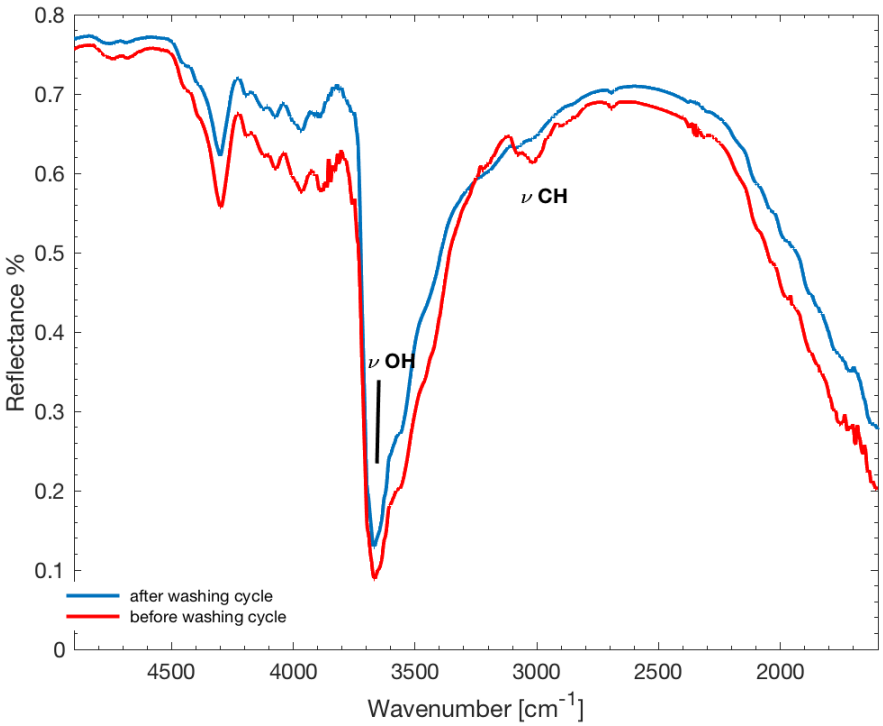

Figure 2.1: IR reflectance spectra of mineral serpentine before (red) and after (blue) the washing cycle in range 4700 - 1500 cm^{-1}. After washing, the absorption bands with wavenumber ∼2900 - 3000 cm^{-1} disappear. The bands are due to asymmetrical and symmetrical stretching of methyl ($–CH_3$) and methylene ($–CH_2–$) groups.

analysis of the samples while the pellets were subjected to subsequent washing. Through the FTIR spectroscopy, we can verify that the methanol and water pre-treatment does not alter the surface sites of the sample via hydroxylation reactions (which would introduce hydroxyl groups into the molecule). Figure 2.1 shows the IR reflectance spectrum of mineral serpentine before (red curve) and after (blue curve) the treatment. The figure does not reveal changes in the OH stretching region of the mineral (band at 3600 cm^{-1}) and in general in the overall spectrum. The comparison of the two IR reflectance spectra, therefore, allows us to verify that there were no alterations in the sample surface sites. The figure also shows how through the FTIR mineral spectra, we can identify the presence of bands due to organic contaminants and check that they have been removed from the washing process.

The steps to remove organic contaminants are given below:

- the mineral of suitable size was washed by sonification with MeOH (75 ml of solvent for 1 g of mineral)
- the solution was separated into two vials of equal mass and centrifuged. The pellet was subjected to a second washing process
- the mineral pellet was washed with methanol plus ddH_2O (80 ml of solvent for 1 g of mineral) for 30 minutes by ultrasonic bath carried on at 60 °C through VWR ultrasound cleaning bath USC200TH
- the solution was centrifuged and the pellet was dried in the oven at 80 °C for one night

The last step to obtain the final analog sample set is the molecule adsorption on the clean mineral surface. Incipient wetness impregnation technique (spiking) was used for rapid adsorption of a controlled number of molecules on solid mineral grains.

2.2 Experimental setup

2.2.1 Bruker VERTEX 70v

For the IR reflectance spectroscopy, a non-destructive technique useful to acquire information on the molecular composition of the solid samples, we used the Bruker VERTEX 70v interferometer. It is a vacuum Fourier Transform Infrared (FTIR) spectrometer with an evacuable optics bench. It is a fully evacuated digital Fast FTIR, double-pendulum interferometer where the two mirrors are rigidly coupled. It is configured for transmission spectroscopy and with a combination of optical components (detectors, source, and beamsplitter), it can cover the spectral range from 10 cm^{-1} in the far infrared (FIR) up to 28000 cm^{-1} in the visible (VIS) spectral range, passing through medium and near infrared (MIR and NIR). In Figure 2.2, we can see an optical scheme of the interferometer. The compartments of the spectrometer can be evacuated separately, i.e., we can evacuate the complete interferometer (sample compartment plus optical bench) or just the optical bench. The vacuum doors, which can be equipped with optical or IR windows, allow ventilation of the only sample compartment to maintain the vacuum in the optical bench compartment during the sample exchange. In our analysis, we used a combination of DTGS DigiTecTM detector with a KBr (potassium bromide) beamsplitter that allows analysis in the air on the spectral range

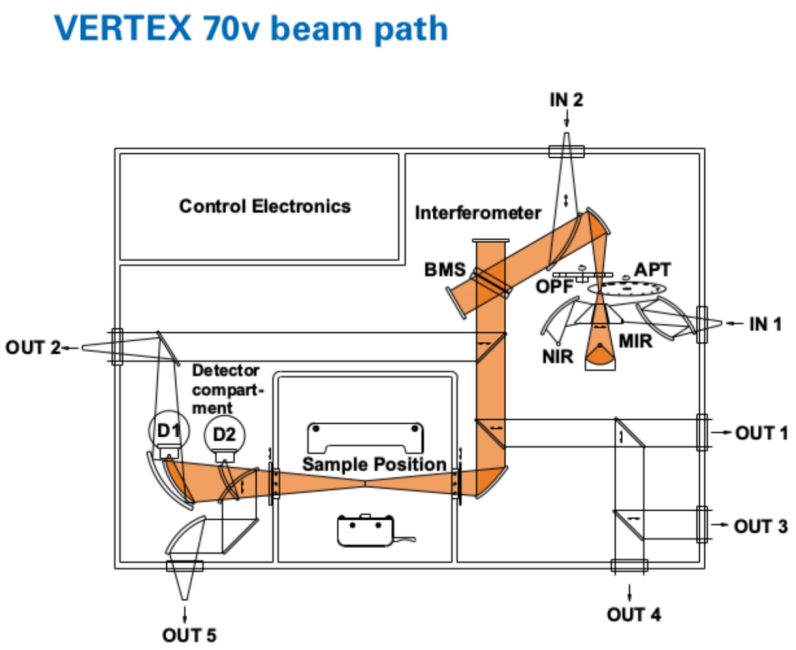

Figure 2.2: Optical scheme of VERTEX 70v interferometer (courtesy of Bruker instrument manual).

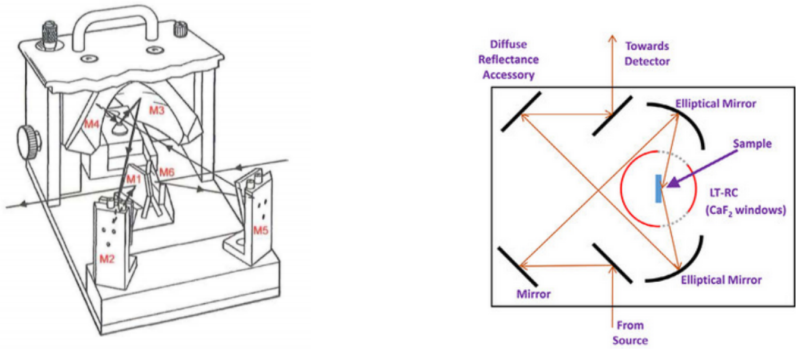

Figure 2.3: Scheme of Praying Mantis^{TM} Diffuse Reflection Accessory (courtesy of Harrick Instruments).

8500 - 350 cm^{-1}. The IR source is a standard MIR Globar lamp a silicon carbide rod, which is electrically heated between 1000 and 1650 °C . As shown in the figure, the VERTEX 70v vacuum spectrometer is equipped with five beam exit ports and two beam input ports and offers the possibility to readily upgrade the systems with external measurement accessories, sources, and detectors. In our analysis, we used the Praying Mantis Diffuse Reflection Accessory from Harrick (from now, we call it PM). PM allows acquiring reflectance spectroscopy, thanks to a set of mirrors as shown in Figure 2.3. It is a highly efficient diffuse collection system that minimizes the detection of the specular component. The system consists of two ellipsoidal mirrors. As we can see from Figure 2.3, the incident beam reaches the first elliptical mirror and this mirror focuses the beam on the sample. The diffuse radiation reflected from the sample reaches the second ellipsoidal mirror. This last mirror collects the diffuse reflected radiation and converges it towards the detector through a diffuse reflectance accessory. Both ellipsoidal mirrors are tilted forward so the diffusely reflected radiation is collected at an azimuthal angle of 120 °C. In this way, the specular reflected component is deflected behind the ellipsoid collection and minimized.

2.2.2 Hiden Analytical Quadrupole Mass Spectrometer

For the mass spectrometry, a useful technique to analyze in the gas phase how the specific fragmentation profiles of a given molecule or compound change following for example a photo-destruction process and to identify any new

more complex molecules formed, we used Hiden Analytical 3F RC 301 Pic Quadrupole Mass Spectrometer. The HAL 3F RC systems are designed for gas analysis in high precision scientific applications. The quadrupole analyzer is a precision assembled triple mass filter. It is a unique, independently driven RF filter, with only secondary filter stages preceding and following the primary mass filter. The triple filter is connected to an RF Head, frequency converter, through a mounting flange, Conflat type DN-63-CF, 4.5/114 mm. In the following Figure 2.4, an image of HAL/3F PIC Quadrupole Mass Spectrometer and an image of its scheme is shown. The ion source is represented by a UHV low profile electron impact ionizer with twin oxide coated iridium filaments which emits a beam of electrons accelerated with an energy of 70 eV. The detector is represented by a pulse ion counting single channel electron multiplier detector. Desorbing surfaces may be positioned within 8 mm of the ion source. The particles detected are neutrals and radicals. Hiden instrument is supplied with MASsoft mass spectrometer control software. MASsoft Professional is a software package allowing both the control of mass spectrometer parameters and manipulation of data and control of external devices.

2.2.3 Vacuum and cryogenics techniques

To simulate space conditions, we need to work in a regime of low pressures and low temperatures. In the interstellar medium, the numerical densities are of the order of 1 particle/cm^3. The pressure range varies from 10^{-6} to 10^{-17} mbar, and the temperature range extends from 20 K up to 8000 K. So, we will illustrate the laboratory tools used to simulate the spatial conditions, i.e., the tools for cryogenic and vacuum conditions.

Tools for vacuum conditions Depending on whether the pressure is little or much lower than atmospheric pressure, there are different regimes of vacuum. Different types of pumps are used to reach high vacuum regimes and low temperatures. The more commons are the diaphragm pumps. These devices use a combination of the reciprocating of a diaphragm and suitable valves to do a pumping action. The oscillation of a diaphragm that closes one side of a chamber causes a variation in volume. When the volume of the chamber is increased from the movement of the diaphragm, the pressure decreases and the fluid is drawn into. When the volume decreases and the pressure increases, the fluid, previously drawn in, is forced outside (Figure 2.5 shows a schematic diaphragm pump). With this pump, the lowest pressure we can reach is typically $\sim$ 1 - 0.3 mbar, a low-medium vacuum.

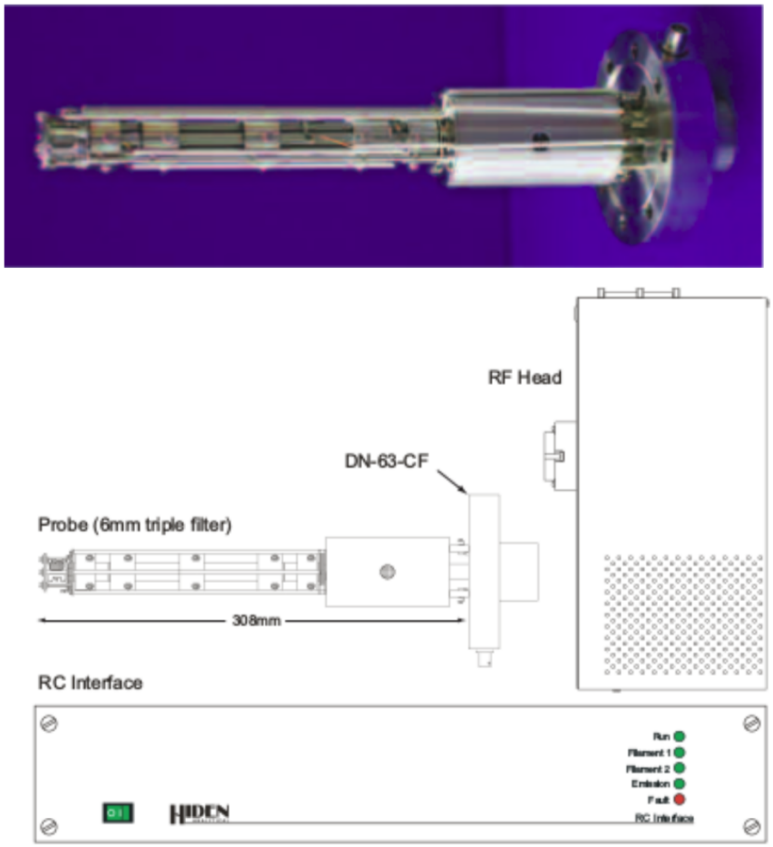

Figure 2.4: HAL/3F PIC Quadrupole Mass Spectrometer (top); scheme of HAL/3F Mass Spectrometer (bottom) (with the courtesy of Hiden Analytical).

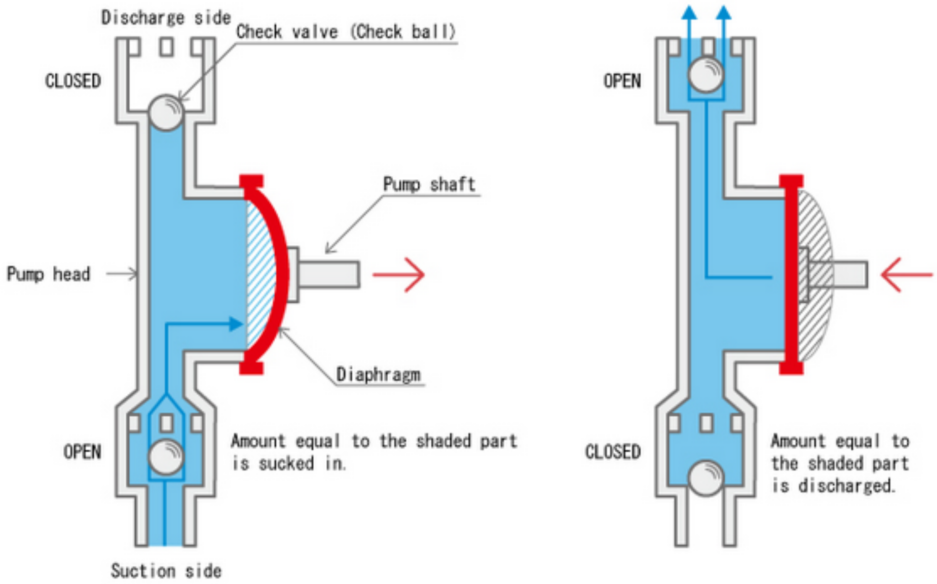

Figure 2.5: Scheme of a diaphragm pump (courtesy of Tacmina instrument manual).

Another type of pumps is represented by rotary pumps. The rotary pump is a mechanical vacuum pump, a device that creates and maintains a vacuum in a region by moving air molecules away. Its rotor is equipped with moving vanes and eccentrically rotates in a stator. The gas is compressed to a pressure slightly higher than the atmospheric pressure by the mechanical action of a rotor and a stator. This overpressure opens a spring-loaded outlet valve, and the gas escapes to the atmosphere. With one stage, the lowest attainable pressure is about 10^{-3} mbar.

To reach ultra-high vacuum conditions, we used a turbomolecular pump. It is made of 10-40 rotating (rotor) and fixed (stator) disks alternately located. Each disk has 20-60 blades with proper tilt. Rotors turn at 10^4 -10^5 rounds per minute. The pumping speed of a turbomolecular pump depends on its rotational speed. The highest rotational speed is achieved at pressures below 10^{-3} mbar. The high speed of the rotating surface transfers momentum to the gas molecules and high vacuum rates can be achieved. Turbo pumps can reach pressure below 10^{-10} mbar, but they must be supported by a primary pump (rotary or diaphragm). We can see an example of a turbomolecular pump in Figure 2.6. In our experimental setup, we used a T-Station 85 turbomolecular pumping station. This structure is formed by

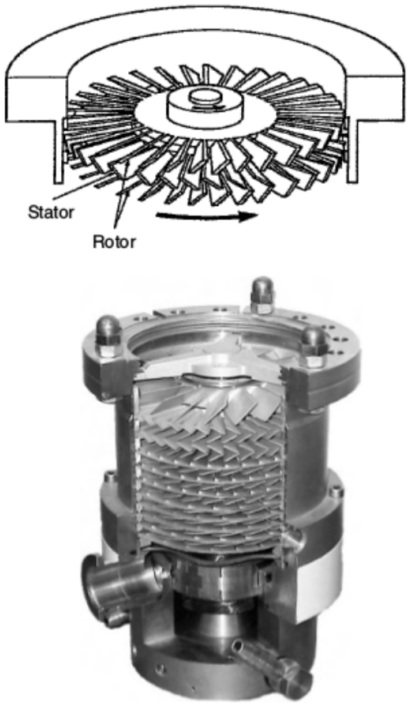

Figure 2.6: Turbomolecular pump. Figure taken from "The art of cryogenic" (Ventura et al., 2008).

a nEXT85H turbomolecular pump (speed 47 l/s) supported by a dry diaphragm pump (speed 1.2 m3/h) and a Turbo and Active Gauge controller. Figure 2.7 displays a scheme of the vacuum system.

Tools for cryogenics conditions In vacuum regime, cryogenic temperatures can be obtained by a coolant cryostat. In the first approximation, the system is composed of a cooler liquid pumped through a transfer line in contact with the sample holder, technically defined as cold finger. Temperature is regulated by the flux of cooling liquid through the transfer line, with the possible support of a heating system. Cooling efficiency depends obviously on the technical characteristics of the system, but it depends mostly on the choice of the coolant. Liquid Helium (LHe) and liquid Nitrogen (LN_2) are often used in laboratory as cooling liquids. Table 2.1 reports the minimum temperatures obtainable with the use of LHe and LN_2.

The Bruker VERTEX 70v interferometer for the reflectance spectroscopy

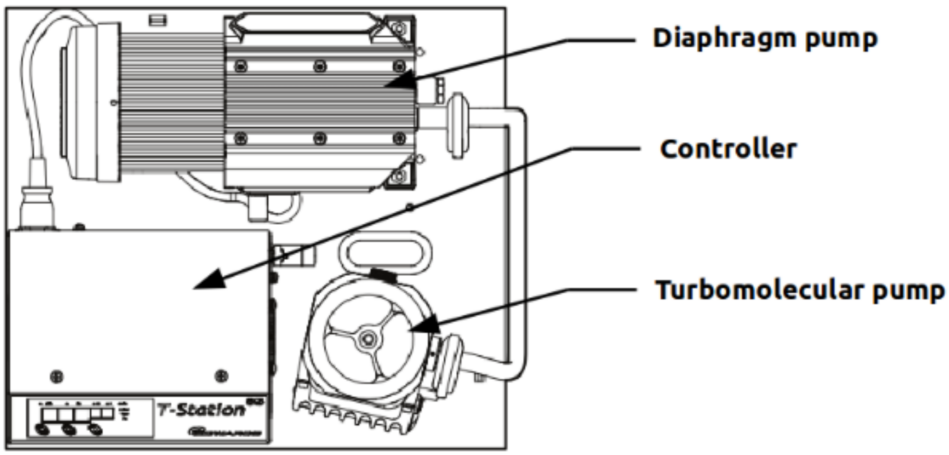

Figure 2.7: Scheme of the T-Station 85 turbomolecular pumping station system (courtesy of Edwards).

	Boiling Point (K)	Melting Point (K)
N_2	77.4	63.3
He4	4.21	

Table 2.1: Thermodynamic properties of LN_2 and LHe

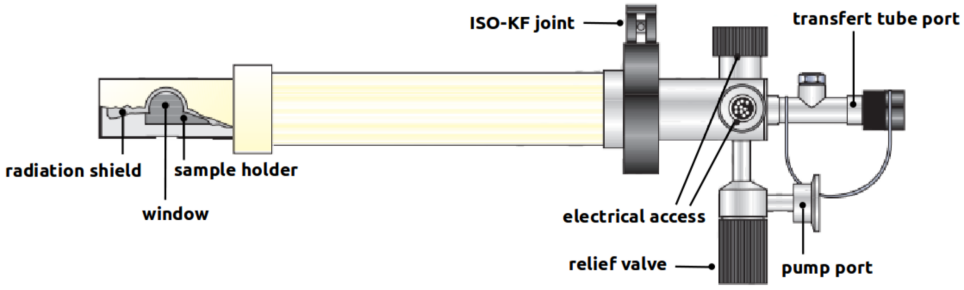

Figure 2.8: A scheme of MicroststHe-R cryostat (courtesy of Oxford Instruments).

interfaces with a MicrostatHe-R cryostat from Oxford Instruments cooled with LN_2. LN_2 is commonly used as a coolant due to its abundance on Earth and its easier handling. With LN_2 as a refrigerant, the minimum temperature obtained is 77.4 K, i.e., its boiling temperature (technically in the laboratory, this limit temperature can be reduced up to 64 K thanks to the kinetic cooling in the forced flow system). In the experimental setup used for infrared spectroscopy, the MicrostatHe-R cryostat operates in the temperature range between 64 and 350 K (nominally the heater can reach 500 K). Figure 2.8 reports a scheme of the cryostat. An oil-free pump draws LN_2 from a storage tank along the low-loss transfer tube (LLT) to the heat exchanger where the temperature sensor is located. A radiation shielded sample chamber is provided to keep the cryostat in vacuum. Using the T-station, a pressure of $5{\cdot}10^{-6}$ mbar was obtained and its value was monitored with a Pfeiffer pressure gauge. The cryostat sample chamber can be equipped with two different sets of IR transparent window: a sapphire window transparent to wavenumbers in the NIR spectral range between 8000 - 1500 cm^{-1} (1.25 - 6 μm), and a KRS-5 window transparent in the MIR up to 400 cm-1 wavenumbers (1.25 - 25 μm). For my vacuum IR spectroscopy experiments, the sample chamber with the sapphire window was used. The infrared spectra of the samples will therefore show the spectral range up to 1500 cm^{-1}. The sample holder is located on the cold finger and inserted into the sample chamber closed with ISO-KF joint to allow high vacuum regimes. The cold finger details are shown in Figure 2.9. To allow reflectance measurements of powdered samples, a cylindrical opening of 3 mm in diameter and 3 mm in depth was made (analog of the standard Harrick Praying Mantis sample holder) on aluminum support fixed on the cold finger to maximize thermal conductivity.

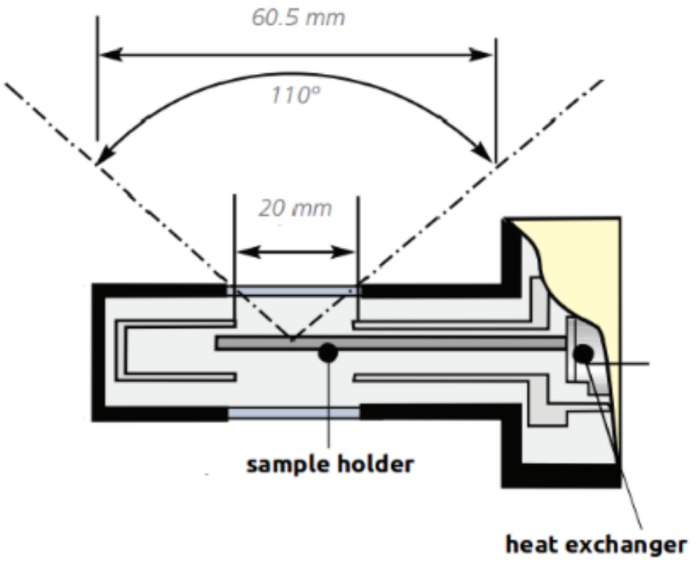

Figure 2.9: Cold finger detail (courtesy of Oxford Instruments).

The sample temperature was measured at the bottom of the cold finger by a thermocouple connected to MercuryiTC cryogenic environment controller from Oxford Instruments. The temperature selected was regulated through the LN_2 flow through the LLT and the power of an electronic heater placed at the bottom of the cold finger. To calibrate the cryostat, we used the spectral features of water ice. The temperature recorded by the sensor has an accuracy of 1 K, value used as the standard error. During the measurement, both the sample chamber and Praying Mantis were sealed and fluxed with nitrogen gas to avoid atmospheric contamination along the beam path.

The ultra-high vacuum (UHV) chamber (P $\sim 6.68 \cdot 10^{-10}$ mbar) equipped with the Hiden Analytical 3F RC 301 Pic Quadrupole Mass Spectrometer (HAL 3F RC) for mass spectrometry interfaces instead with a cryostat cooled with Helium. The advantage of working with a helium cryostat is the possibility of reaching lower temperatures than the cryostat cooled with liquid nitrogen and therefore simulating a wider range of astrophysical temperatures. In fact, helium boils at 4.2 K. In our experimental set-up, we worked with an ARS closed-cycle helium cryocooler able to get a temperature of 17 K. By going down to 17 K, we can simulate the temperatures of interstellar ice analogs composed of iCOMs and grains relevant in astrophysics. Closed-cycle

cryostats have the advantage of not requiring the expensive and inconvenient use of cryogenic liquids and allow to reach very low temperatures ($\sim$ 17 K) without the use of liquefied gases. The closed-cycle cryostat operates on the principle of the Gifford-McMahon refrigeration cycle. The cryostat uses helium gas as the operating refrigerant gas and contains a compression and an expansion space. Helium gas is 99.999% pure, with dew point $<$ -50° at 300 psig (2069 kpa). Two gas lines and an electrical power cable connect the compressor to the expander. Via the two gas lines, high-pressure helium gas enters the expander, and low-pressure helium gas exits the expander. The expander electrical power from the compressor drives the valve motor inside the expander. The compressor requires electricity and cooling water, in our experimental setup supplied by a Eurochiller chiller.

2.2.4 UV irradiation system

In the laboratory, vacuum regime and cryogenic temperatures allow us to simulate and reproduce the spatial conditions. Furthermore, other factors can be introduced into the experiment to increase the potential of the laboratory analysis. Both the Bruker Vertex 70v FTIR interferometer and the ultra high vacuum chamber equipped with the quadrupole mass spectrometer can be interfaced with an enhanced UV lamp to simulate the solar radiation. In the astrobiology context, it is important to study the interactions between molecules and minerals to understand the physico-chemical mechanisms that lead to the synthesis of complex chemical compounds observed in the gas phase in space. UV radiation is one of the mechanisms responsible for chemical evolution in space promoting photochemical reactions on surfaces of dust grains.

The photodissociation rate of a molecule exposed to a UV radiation field is:

$$k = \int \sigma(\lambda) \cdot I(\lambda) \cdot (\lambda), \tag{2.1}$$

where $\sigma(\lambda)$ is the photodissociation cross section and $I(\lambda)$ is the intensity of the incident UV radiation summed over all angles of incidence. The integration limits are defined by the wavelength of the incident radiation (Heays et al. 2017). Photochemical processes induced by UV radiation can be photolysis, photocatalysis, and photosynthesis. The term photolysis indicates the decomposition of an atomic structure following exposure to UV photons. Photocatalysis refers to the promotion of an exergonic reaction, while photosynthesis to an endergonic reaction. The mineral can play a key role in

this process acting as catalysts protecting molecules against UV degradation or promoting chemical reactions. A strong bond between the molecule and the mineral surface makes weaker the internal bonds of the molecule. In this case, the minimum photon energy to split the bond is reduced and the fraction of photons capable of causing the split increases.

In our experimental setup to simulate the radiation of Solar-type stars, we used Newport Xenon enhanced UV 300 W lamp with purified Xenon at 5- 20 bar (wavelength range 185-2000 nm). Xenon (Xe) light sources have a smooth emission in the UV-VIS spectrum, with characteristic wavelengths emitted from 750-1000 nm. Xenon light sources are a good simulator of the radiation of Solar-type stars because their emission spectrum is like that of the Sun with a color temperature of ∼5800 K. In Figure 2.10, the lamp spectrum is reported. The UV radiation emitted by the lamp was collimated through an optical system formed by a first mirror that reflects the radiation coming from the lamp to a grade fused silica collimating condenser lens and it collimates UV radiation towards an optical fiber. The lamp flux was calibrated at Istituto Nazionale di Ottica in Arcetri. The Newport Research Arc Lamp Housing 50-500 W is shown in Figure 2.11.

Figures 2.12 and 2.13 show respectively the Bruker Vertex 70v FTIR interferometer for IR spectroscopy and the ultra-high vacuum chamber equipped with a quadrupole mass spectrometer both interfaced with the enhanced UV lamp.

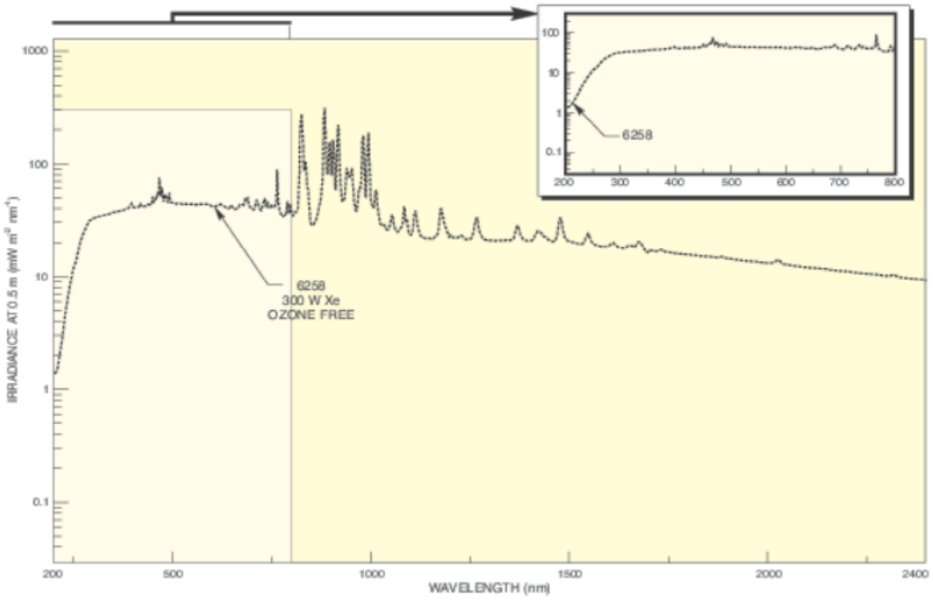

Figure 2.10: Spectrum of Newport Xenon ehnanced UV 300 W lamp (courtesy of Newport Corporation).

Figure 2.11: Newport Research Arc Lamp Housing 50-500 W (courtesy of Newport Corporation).

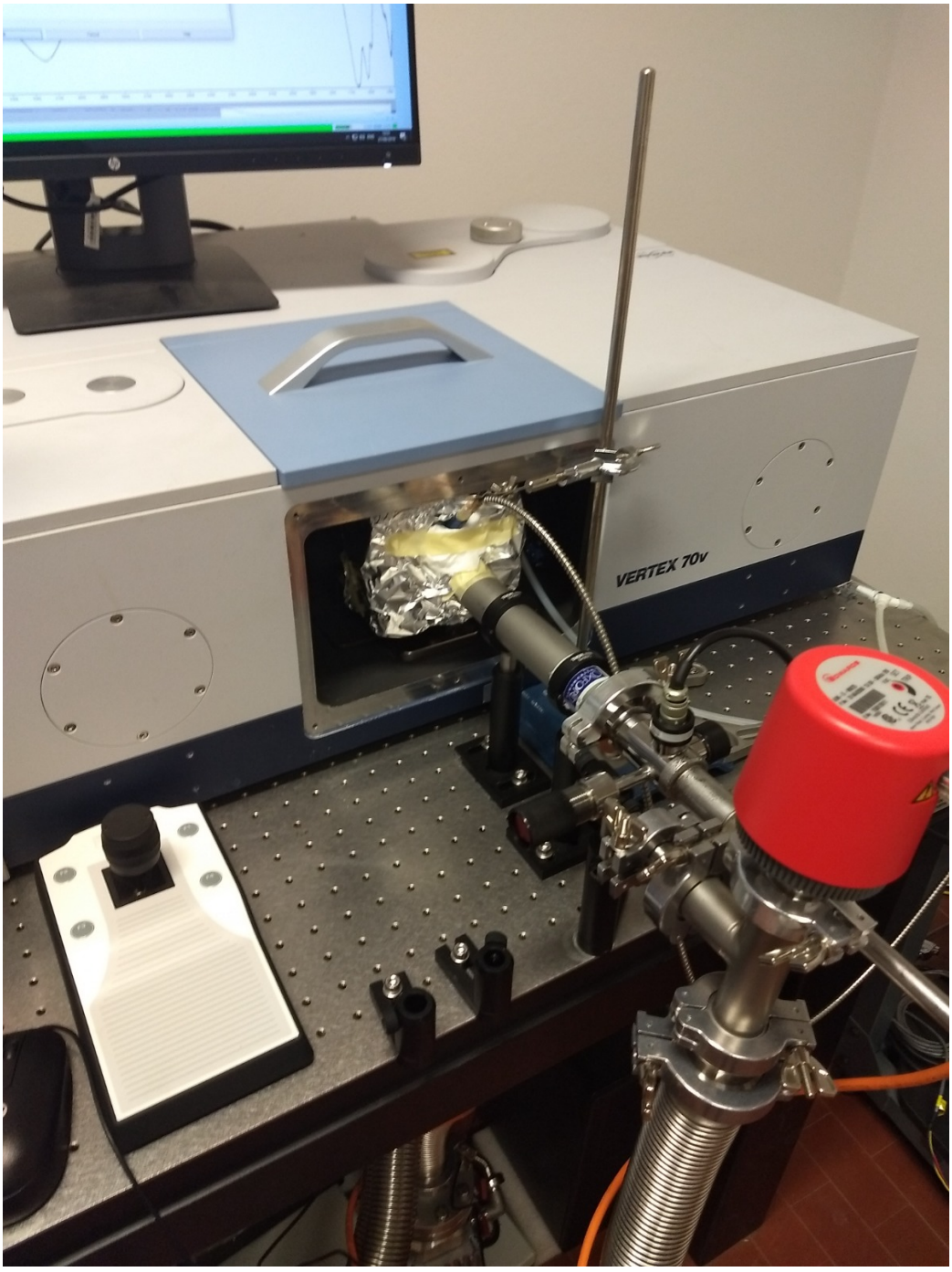

Figure 2.12: The figure shows the Bruker 70v interferometer, the LN2-cooled cryostat arm, and the optical fiber of the enhanced UV lamp entering the chamber for in situ UV irradiation experiments.

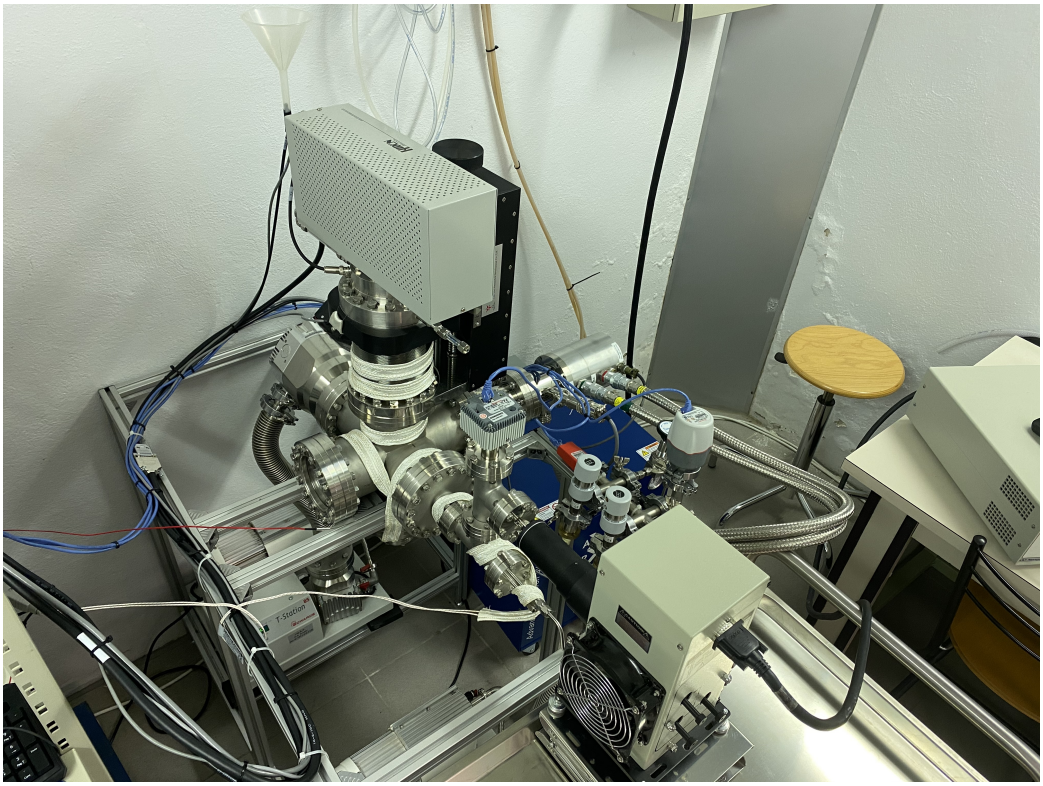

Figure 2.13: The figure shows the experimental set-up used for thermal desorption experiments. The UHV chamber interfaces with quadrupole mass spectrometer to analyze masses from 1 to 300 m/z, with closed cycle helium cryostat to work at 17 K, and with enhanced UV lamp to simulate the UV radiation.

Chapter 3

Photoprocessing of formamide ice

The first work of my PhD project involved a particular prebiotic molecule, formamide ($HCONH_2$, molecular weight of 45 a.m.u.). Initially, samples of pure formamide ice and adsorbed on space relevant minerals were subjected to UV irradiation in situ and analyzed by FTIR spectroscopy. Through these analyzes, the effects of UV degradation and the interactions between formamide and two different types of minerals, silicates and oxides, are compared. We found that silicates, both hydrates and anhydrates, offer the molecules a higher level of protection from UV degradation (one order of magnitude) than mineral oxides. The second part of the work concerned the thermal desorption of pure formamide ice and in the presence of TiO_2 dust, before and after UV irradiation, investigated by TPD analysis.

In the first section, we will present formamide, because it is considered a prebiotic molecule and its relevance in astrophysics, and the different minerals chosen as analog samples. In the second section, in situ UV irradiation of pure formamide ice and its adsorption by minerals at 63 K are reported and we will describe the laboratory procedure, the UV photodissociation analysis and the results obtained. In the third section, the thermal desorption of pure formamide ice and in the presence of TiO_2 dust, before and after UV irradiation, and the results obtained are described.

This chapter is based on the publication "Photoprocessing of formamide ice: route to prebiotic chemistry in space", Corazzi et al., 2020.

3.1 Formamide and minerals

Chemical reactions of molecules containing H, C, N, and O such as formamide ($HCONH_2$) are considered a plausible pathway for synthesis of biomolecules under prebiotic conditions (Oparin, 1938). Moreover, formamide is the simplest molecule containing the peptide bond, which is known to be the basis for assembling proteins and polypeptides starting from amino acids, with a crucial role in the biotic processes of life on Earth. Formamide was first detected in the gaseous phase in two high-mass star forming regions: Orion-KL, an active star forming region, and the giant molecular cloud $SgrB_2$ (e.g., Turner 1991; Nummelin et al. 1998; Halfen et al. 2011); later it was detected in the comet Hale Bopp (Bockelée-Morvan et al., 2000), whose chemical composition is suspected to be similar to the chemical composition of the primitive Solar Nebula. Furthermore, during landing of Philae aboard Rosetta mission, in situ mass spectrometer data inferred the presence of formamide in the comet nucleus with the highest abundance after water (Goesmann et al., 2015). In recent years, formamide was also observed in two types of low-mass star forming environment: shocked regions by protostellar jets (e.g., Codella et al. 2017) and hot corinos (Kahane et al. 2013; López-Sepulcre et al. 2015; Marcelino et al. 2018; Imai et al. 2016; Oya et al. 2017; Lee et al. 2017). Protostellar shocks produced by episodic jets of matter propagate at supersonic velocity through dense gas surrounding the star. In these shocked regions, the presence of a large number of molecules is due to mechanical release by gas–grain collisions and grain–grain collisions (López-Sepulcre et al. 2019, Codella et al. 2017). Instead, in the hot corinos, that are inner, compact (<100 AU) and hot regions of some Class 0 protostars (Ceccarelli 2004, Ceccarelli et al. 2007, López-Sepulcre et al. 2019), the presence of molecules in gas pahse is due to thermal desorption given the high temperatures involved (>100 K). Interestingly, formamide has only been detected in protostars that host a hot corino (Sakai et al. 2013, López-Sepulcre et al. 2019). This evidence implies that, besides the release in protostellar shocks, the presence of formamide is strictly linked to hot (>100 K) regions where thermal desorption is the responsible process for sublimation of frozen mantles into the gas phase.

Because silicates are ubiquitous in space, their choice as analog samples is quite straightforward. There is evidence of silicates from comets, observed from both ground observations (e.g., Shinnaka et al. 2018 and Ootsubo et al. 2020 with Subaru 8.2 m telescopes or Picazzio et al. 2019 with 4.1m SOAR telescopes) and from space missions (e.g., Brownlee et al. 2006 for Stardust Comet Sample Return Mission and Bockelée-Morvan et al. 2017 for Rosetta Mission), to protoplanetary disks (e.g., Cohen et al. 1985, Przy-

Table 3.1: **Minerals and origin**

Mineral	Origin
Antigorite $(MgFe^{++})_3Si_2O_5(OH)_4$	Reichenstein
Titanium dioxide TiO_2	Sintetic
Pyrite FeS_2	Cerro de Pasco
Spinel $MgAl_2O_4$	Vesuvio
Forsterite Mg_2SiO_4	Vesuvio
Olivine $(Mg,Fe)_2SiO_4$	purchased

godda et al. 2003, Boekel et al. 2004, Natta et al. 2007, Henning 2010). Silicates were also found in the cometary coma of Hale Bopp (Min et al., 2005), the first comet where formamide was detected. Moreover, dust has been observed in circumstellar envelopes around young stars (Cesaroni et al., 2017) and in evolved stars and planetary nebulae (Jaeger et al., 1998). Among silicates, we chose antigorite $(Mg,Fe^{++})_3Si_2O_5(OH)_4$, and forsterite Mg_2SiO_4 for formamide studies and olivine ($(Mg,Fe)_2SiO_4$) for acetaldehyde and acetonitile experiments (subsequent chapters). Antigorite belongs to the serpentine group; it is a hydrate silicate with a water or hydroxyl group present in the structure and has a lamellar aspect with well-defined cleavages. Forsterite is the magnesium-rich end-member of the olivine group and is one of the most abundant silicate minerals in the Solar System. It has been found in meteorites (Weinbruch et al. 2000), cometary dust (Messenger et al. 2005), and in a protoplanetary disk (Fujiyoshi et al. 2015). Furthermore, Mg-containing minerals are important because the magnesium may have played an important role in prebiotic geochemistry. Olivine is an isomorphic mixture of forsterite (Mg_2SiO_4) and fayalite (Fe_2SiO_4) and in our acetaldehyde and acetonitrile experiments (subsequent chapters), we used olivine made up of 80% of forsterite and 20% of fayalite. Fayalite (Fe_2SiO_4), the iron end-member of the olivine group, was found in the interstellar medium and meteorite (Boruah et al., 2017). Olivine is one of the most common silicate grain in space: through IRAS low-resolution spectra, olivine dust was detected as common material in the circumstellar disks or/and shells of Herbig Ae/Be stars (e.g., Chen et al. 2000) and around T Tauri stars (e.g., Honda et al. 2003). More recently, the mid-infrared spectrum obtained through Spitzer Space Telescope revealed the presence of crystalline silicate in a cold, infalling, protostellar envelope of the Orion A protostar HOPS-68 (Poteet et al., 2011). Protostar EX Lupi is the prototype of EXORs like objects, that are similar to FUORs objects mentioned above but their outbursts are

shorter and recursive in time, and it underwent its most important explosion in 2008, when its brightness increased by a factor of 30 for six months, due to the high accretion from the circumstellar disk on the star. Ábrahám et al., 2020 observed the system during the explosion and discovered the crystallization of the amorphous silicate grains due to the heating of the disk. In particular, they observed silicates of the order of micrometer size.

In the formamide experiments described in this chapter, mineral oxides are the other class of minerals chosen besides silicates. We used magnesium alluminium oxide $MgAl_2O_4$ from the spinel group and titanium dioxide TiO_2 from the rutile group. Spinel group minerals are interesting because they have been found in a wide range of terrestrial and extraterrestrial geological environments (BjäRnborg et al., 2013; Caplan et al., 2017). TiO_2 comprises a significant amount (0.63%) of the Earth's crust and is preserved as presolar grains extracted from meteorites (Nguyen et al., 2018; Nittler et al., 2008).

Finally, we also made the formamide adsorption on a mineral belonging to the sulfides class. Sulfides were found in the ejecta of comets (Jauhari, 2008) and in the cometary coma of Hale Bopp (Lisse et al., 2006). Among sulfides, pyrite FeS_2 was chosen as it is involved in the chemical mechanism responsible for the synthesis of hydrocarbons (Navarro-Gonzalez et al., 2008).

Table 3.1 lists the minerals chosen and their origin.

3.2 Laboratory procedure and UV photodissociation analysis

In the previous chapter, we described the analog samples preparation and the methanol and water pre-treatment of minerals to remove the organic contaminants. Rutile TiO_2 was not subjected to such treatments to not alter its Lewis acidity (see e.g., Panayotov et al. 2010).

The formamide sample was purchased from Sigma Aldrich, Merck corporation with a purity $\geq 99.5\%$. Through FTIR spectroscopy, we investigated in situ UV irradiation of pure formamide and its adsorption onto minerals at 63 K and at $P \sim 10^{-5}$ mbar. LN_2 was pumped along the transfer line to the cryostat. The sample was located in the sample holder, the area and depth of which are $A = 7.07$ mm^2 and $d = 4$ mm, respectively, for a total volume of $V = 0.03$ ml. The sample fixed on the cold finger was inserted into the vacuum chamber interfaced with the interferometer by the reflectance accessory. The temperature was controlled with an accuracy of ± 0.1 K with *Mercury* iTC by Oxford Instruments. The IR reflectance spectra were taken at different irradiation times and the degradation process was followed in real

time by observing the changes in spectral features. Each band area, which is proportional to the number of functional groups, was evaluated at different irradiation times. The degradation rate β was obtained by fitting the fraction of unaltered molecules, A(t)/A(0), estimated by the band area at a specific irradiation time t normalized on the band area before irradiation, versus time t, using an exponential function:

$$\frac{A(t)}{A_0} = B \cdot e^{-\beta \cdot t} + C, \tag{3.1}$$

where A_0 is the band area before irradiation, proportional to the initial number of molecules in the sample, B is the fraction of molecules that interacted with UV radiation, β is the degradation rate, and C is the fraction of molecules that did not interact with UV radiation because they lie deep in the solid samples. In case of band degradation, A(t)/A(0) decreases with increasing irradiation time. The half-life time $t_{1/2}$ (time necessary to destroy 50% of the initial molecules) and the UV destruction cross section σ were obtained from β as follows

$$t_{1/2} = \frac{\ln(2)}{\beta}, \tag{3.2}$$

$$\beta = \frac{\sigma \cdot \phi_{tot}}{A}, \tag{3.3}$$

where the destruction cross section σ is the probability that chemical bonds of formamide are broken by UV radiation. Finally, ϕ_{tot}/A is the incident flux of UV radiation coming out from the optical fiber per unit area integrated with the absorbance of formamide. The photon flux measured from the "Consiglio Nazionale delle Ricerche" (CNR) Laboratory of Optics is $2.48 \cdot 10^{16}$ photons$\cdot$sec$^{-1}\cdot$cm^{-2}.

In case of formation of new bands, the kinetic was investigated by the function

$$\frac{A(t)}{A_{max}} = 1 - e^{-\alpha \cdot t}, \tag{3.4}$$

where A(t) is the band area at the specific time t, which is proportional to the number of molecules formed at the time t; A_{max} is the maximum band area, which is the maximum number of molecules formed; and α is the formation rate. In the case of formation of a new band, A(t)/A_{max} increases with increasing irradiation time. The formation cross section σ_f was evaluated as follows

$$\alpha = \frac{\sigma_f \cdot \phi_{tot}}{A}, \tag{3.5}$$

where the formation cross section σ_f is the probability that new chemical bonds are formed by UV irradiation.

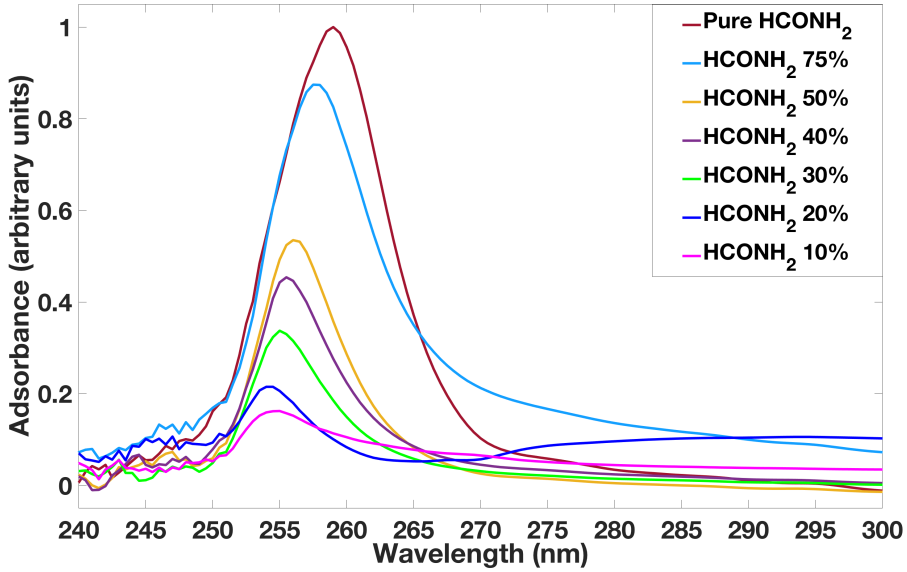

Figure 3.1: Absorption peaks of solutions with different concentrations of formamide in water.

3.2.1 Results and discussion

Initially, we measured the UV absorption of formamide to find out the absorption wavelength range once the samples are subjected to UV irradiation. Figure 3.1 shows the absorption peaks of formamide in water at several concentrations. We found that the absorption is concentrated in the range 200 - 300 nm with a maximum between 255 and 260 nm. As the concentration of formamide decreases (from the highest to the lowest curve), the absorption peak shifts towards shorter wavelengths and Figure 3.2 shows a linear relationship between the maximum absorption and the concentration of formamide.

The reflectance spectrum of pure formamide at 63 K under simulated space conditions is reported in Figure 3.3, which shows the wavenumber range from 4500 to 1500 cm^{-1} where the main bands analyzed in our work are present. Between 3600 and 3281 cm^{-1}, we note the presence of the OH broad band due to residual water present in the chamber and frozen with the sample. Band assignments are reported in Table 3.2. In the first column, we report vibrational modes observed, the second column shows band positions of pure formamide ice compared to the literature positions, which are reported in column three. Band positions of formamide adsorbed

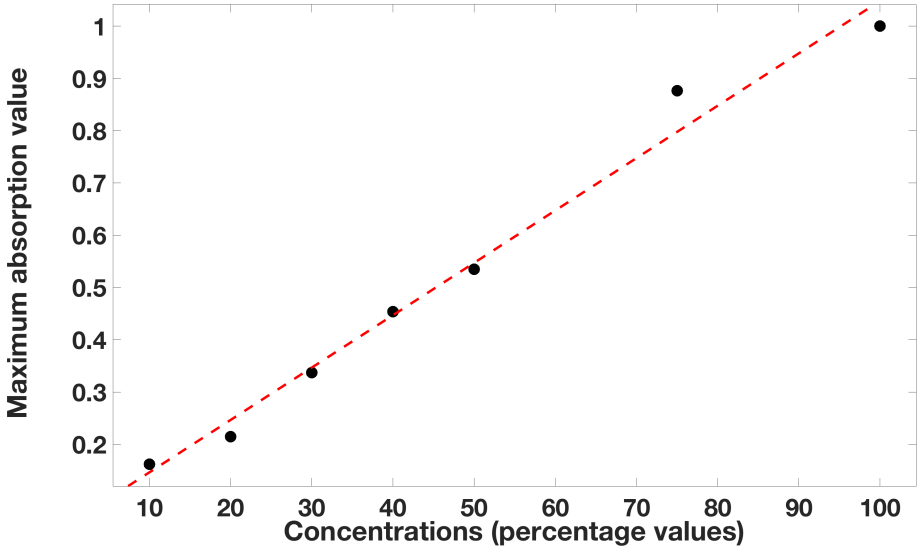

Figure 3.2: Linear relationship between the maximum absorption value and the formamide concentration.

on different minerals are also reported in the last columns.

Table 3.2 shows that the bands of pure formamide are still present when formamide is adsorbed by minerals, even if a shift of peak positions occurs. An example of how spectral features change before and after adsorption onto minerals is reported in Figure 3.4, where the IR reflectance spectrum of pure formamide, antigorite mineral, and formamide adsorbed by antigorite in a vacuum at 63 K are shown. The spectrum of pure formamide ice shows two neighboring bands at 3266 and 3162 cm^{-1} due respectively to NH_2 asymmetric and symmetric stretching and a band at 2895 cm^{-1} due to CH stretching (Sivaraman et al., 2013). These bands are still present and more intense in the spectrum of formamide adsorbed by antigorite, but they are shifted to the wavenumbers 3350, 3166, and 2891 cm^{-1} respectively (Table 3.2). The spectra of formamide adsorbed on the other minerals also show these bands. When formamide is adsorbed by TiO_2, spinel, and forsterite, the band at 3266 cm^{-1} is shifted to the wavenumbers 3298, 3285, and 3275 cm^{-1} respectively, while the 3162 cm^{-1} band is present at 3166 cm^{-1} in the presence of all minerals. On the contrary, pyrite does not show these two neighboring bands. In the presence of TiO_2, spinel, and forsterite, the 2895 cm^{-1} formamide band is shifted to the wavenumber 2891 cm^{-1}, the same shift is obtained in the presence of antigorite. In the case of pyrite, it is moved to

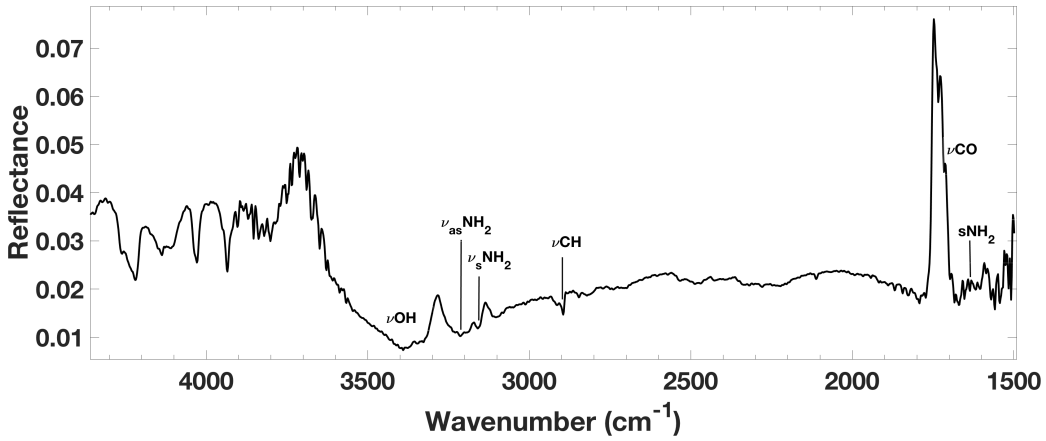

Figure 3.3: Infrared reflectance spectrum of pure formamide ice in the spectral range between 4500 and 1500 cm^{-1} where the main band assignments are present. Vibrational modes: ν_s symmetric stretching; ν_{as} asymmetric stretching; ν stretching; s scissoring.

Table 3.2: **Band assignments**

Mode	Band (cm^{-1})		Formamide adsorbed on				
	Formamide	Literature	Antigorite	TiO_2	Pyrite	Spinel	Forsterite
ν_{as} NH_2	3266	3368[1]	3350	3298	...	3285	3275
ν_s NH_2	3162	3181[1]	3166	3166	...	3166	3166
ν CH	2895	2891[1]	2891	2891	2890	2891	2891
...	...	...	2815	2815	2816	2816	2815
ν CH	...	2770 – 2763[2]	2770	...	...	2772	2771
ν CO	...	...	2473	2471	2473	2475	2474
ν_{as} CO_2	...	...	...	...	...	2348	...
ν CO	...	...	2329	2328	...	2323	2328
ν_{as} NCO	...	...	2275	2275	2276	2277	2277
ν CO	...	1754[3]	1750	1750	1750	1750	1750
ν CO	1715	1713[2]	1716	1717	1717	1716	1717
ν CO	1697	1698 – 1704[1]	1699	1699	1699	1699	1699
ν CO	1684	1685 – 1681[1]	1684	1684	1684	1684	1684
s NH_2	1635	1631[4,1]	1635	1635	1635	1635	1635

Note: First column: vibrational modes; second column: bands observed in the IR reflectance spectrum of pure formamide during laboratory work; third column: band assignments based on published experimental and theoretical studies: (1) Sivaraman et al. 2013, (2) Nguyen 1986, (3) Mc Naughton et al. 1999, (4) Brucato et al. 2006; other columns: bands observed in the IR reflectance spectrum of formamide adsorbed by antigorite, TiO_2, pyrite, spinel, forsterite. Vibrational modes: ν_s symmetric stretching; ν_{as} asymmetric stretching; ν stretching; s shissoring.

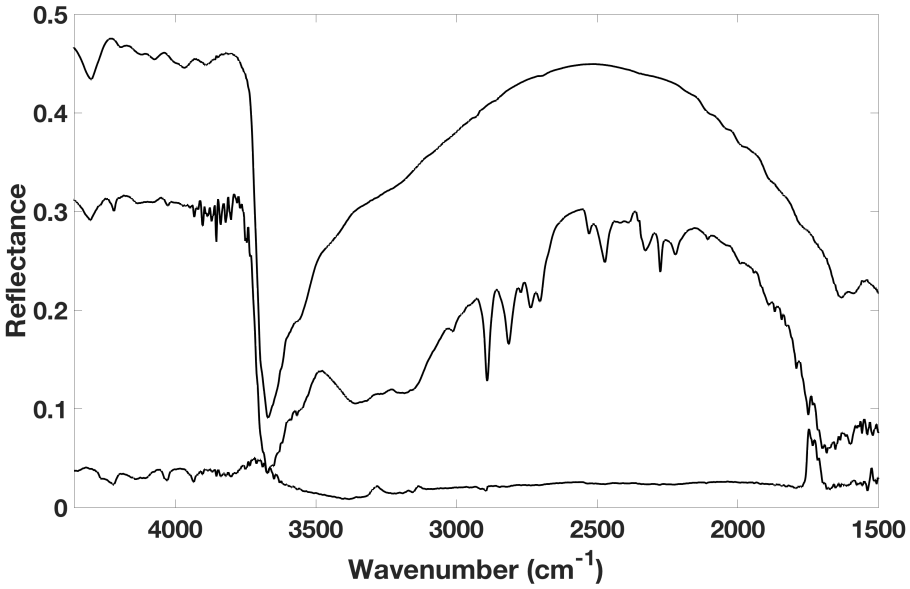

Figure 3.4: From top to bottom: IR reflectance spectrum of antigorite, formamide adsorbed by antigorite, and pure formamide in vacuum. Formamide bands are still present and more intense in the spectrum of formamide adsorbed by the mineral.

2890 cm^{-1}. At lower wavenumbers, the formamide spectrum shows bands due to CO stretching: 1715 cm^{-1} (Nguyen, 1986), 1697 cm^{-1}, and 1684 cm^{-1} (Sivaraman et al., 2013). All these bands are still present in the mineral spectra. The band of this functional group at 1715 cm^{-1} shows a small shift to 1716 cm^{-1} when formamide is adsorbed by antigorite and spinel and to 1717 cm^{-1} in the presence of TiO_2, pyrite, and forsterite. The band at 1697 cm^{-1} shifts to 1699 cm^{-1} in all the other spectra. Alternatively, the band at 1684 cm^{-1} has the same position in all spectra. The 1635 cm^{-1} formamide band due to NH_2 scissoring (Brucato et al. 2006; Sivaraman et al. 2013) also shows no shift and it is present in the same position in all spectra (see Table 3.2).

Now we present our study of the effects of UV photolysis, first irradiating pure formamide and then when it was adsorbed by minerals. Pure formamide ice did not show any significant degradation (i.e., IR band intensity does not decrease) even after 5 hours of UV irradiation as shown in Figure 3.5. This result suggests that formamide is highly stable upon radiation under the conditions simulated in our experiment.

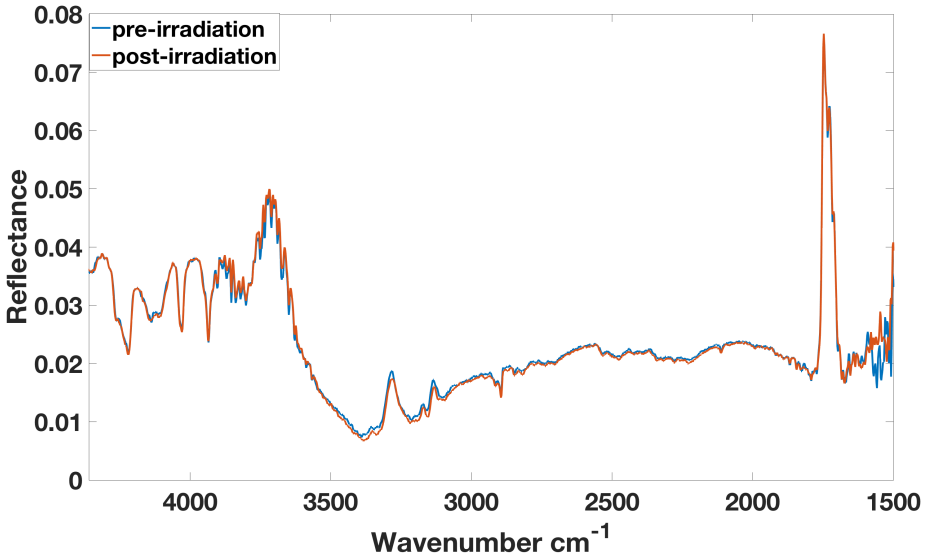

Figure 3.5: Highlighting the pre- and post-irradiation spectra (total UV irradiation time is 5 hours) of pure formamide ice. The spectrum did not show any significant change.

However, finding pure formamide in the solid state in space is unlikely. It is more plausible that formamide is formed in a mixture of other iCOMs as an icy mantle on dust grains. When formamide was adsorbed by minerals and subjected to the same irradiation experiments (equal irradiation time with same photon flux, therefore an equal amount of UV energy), stability was compromised.

Figure 3.6 shows how the spectral features of formamide adsorbed by antigorite changed as the irradiation time increased. From this figure, after 5 hours of radiation, the intensity of the bands at 3350 and 3166 cm^{-1} due to NH_2 stretching can immediately be seen to be notably reduced, that is, the radiation has degraded the molecule, preferentially breaking the amino group bonds. We observed a reduction of intensity also for the band at 2891 cm^{-1} which is due to CH stretching and those at 2473, 2329, and 1750 cm^{-1} which is due to CO stretching. For these bands, we evaluated from the kinetic analysis of the degradation process a cross section σ of $\sim 10^{-20} cm^2$. Similar results were obtained for formamide adsorbed by forsterite, which unlike antigorite is an anhydrate silicate. With forsterite, the two bands due to NH_2 stretching showed no change after 5 hours of irradiation, while the intensity of the bands at 2771 and 2474 cm^{-1} due to CH and CO stretching,

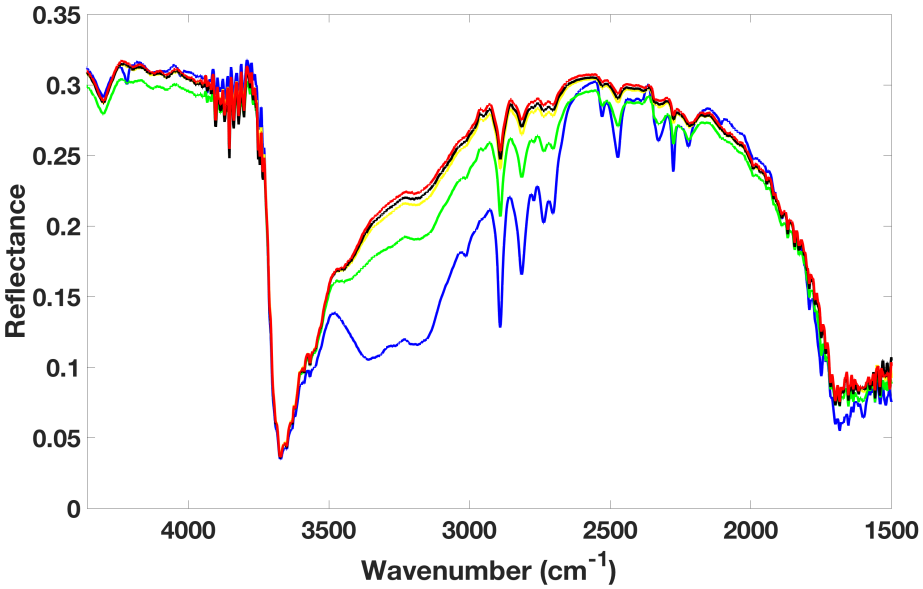

Figure 3.6: Infrared reflectance spectrum of formamide adsorbed on antigorite at 63 K in vacuum. From bottom to top: before irradiation (blue line), after 1 hour of UV irradiation (green line), after 3 hours of UV irradiation (yellow line), after 4 hours of UV irradiation (black line), after 5 hours of UV irradiation (red line).

respectively, was reduced. Compared to antigorite, for irradiating formamide adsorbed by forsterite, we observed intensity changes in a smaller number of bands, but the degradation process occurred with the same cross section of 10^{-20}cm^2. When formamide was adsorbed by TiO_2, the bands that showed variation during the irradiation experiment were the two bands at 3298 and 3166 cm^{-1} due to NH_2 stretching and the band at 2891 cm^{-1} due to CH stretching. With the spinel, on the other hand, the bands at 2323 and 2348 cm^{-1} due to CO stretching and CO_2 asymmetric stretching, respectively, showed changes. When formamide was adsorbed both by TiO_2 and by spinel, the cross sections found were 10^{-19}cm^2, that is, an order of magnitude greater than that obtained for the silicates.

From these results, we can divide minerals according to their effect on photodegradation of formamide. Under the experimental conditions with which the photo-stability of formamide was studied, we found that the silicates are more effective in protecting formamide against UV degradation compared with mineral oxides, the difference being of an order of magnitude.

When formamide was adsorbed by pyrite, the degradation of the bands was not observed even after 5 hours of UV irradiation, and therefore pyrite is capable of protecting the molecule from UV degradation. Interestingly, only when formamide was adsorbed by pyrite or forsterite, we observed the formation of a new band at 2341 cm^{-1} due to CO_2 asymmetric stretching. Therefore, during the irradiation, CO_2 formation occurred within the icy matrix (Figure 3.7).

Tables 3.3, 3.4, and 3.5 report our kinetic analysis of the degradation and formation process performed for all bands of each sample.

3.3 Laboratory procedure and Thermal Desorption analysis

In the high vacuum chamber, HVC ($5 \cdot 10^{-8}$ mbar), formamide vapor was deposited on the cold finger at 63 K through a valve system. The molecules condensed and formed an icy film which was subjected to in situ UV irradiation. After irradiation, the sample was heated at a constant rate of 0.6 K·sec^{-1}. As the cold finger warmed up, the condensed molecules desorbed, entered the mass spectrometer, and were detected; TPD curves were obtained for selected masses. We used the same experimental setup to study the thermal desorption of formamide condensed onto dust grains. The grains were placed on the sample holder of the cryostat and inserted into the high vacuum chamber. In this case, when formamide entered the chamber, it

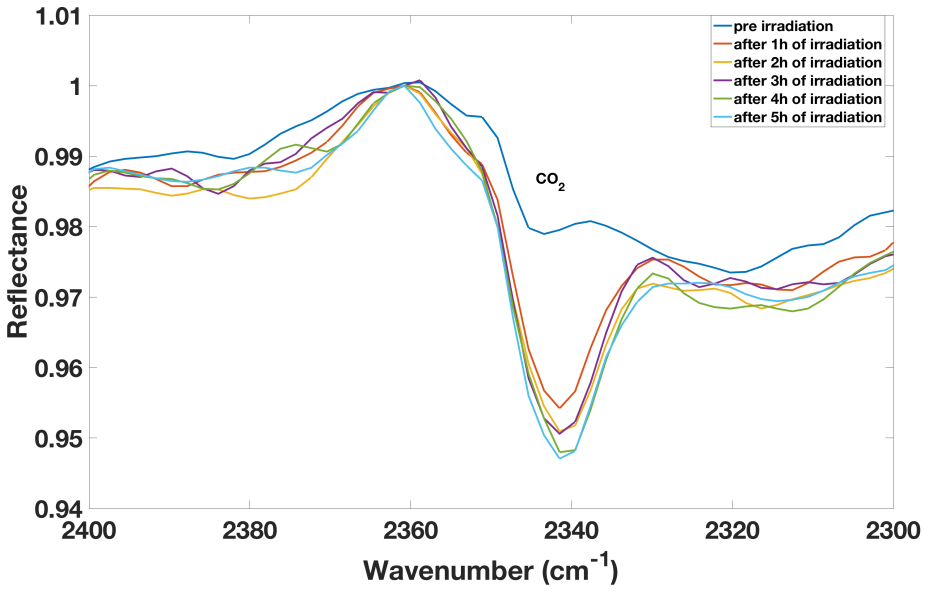

Figure 3.7: Infrared reflectance spectrum of formamide adsorbed by pyrite in the spectral range between 2400 and 2300 cm^{-1}. As the irradiation time increased from the higher to the lower spectrum, the band at 2341 cm^{-1} due to CO_2 asymmetric stretching increased in intensity.

Table 3.3: **Photodissociation parameters in simulated space conditions**

IR reflectance spectrum of formamide adsorbed by antigorite at 63 K in vacuum

Peak (cm^{-1})	Mode	β (min^{-1})	B	C	R^2
3350-3166	$\nu_{as,s}$ NH_2	$0,029 \pm 0,005$	$0,87 \pm 0,05$	$0,05 \pm 0,04$	0,98
2891	ν CH	$0,023 \pm 0,005$	$0,46 \pm 0,06$	$0,51 \pm 0,05$	0,98
2473	ν CO	$0,026 \pm 0,008$	$0,75 \pm 0,07$	$0,24 \pm 0,05$	0,99
2329	ν CO	$0,023 \pm 0,004$	$0,84 \pm 0,05$	$0,20 \pm 0,04$	0,97
1750	ν CO	$0,018 \pm 0,009$	$0,6 \pm 0,1$	$0,38 \pm 0,08$	0,97

IR reflectance spectrum of formamide adsorbed by TiO_2 at 63 K in vacuum

Peak (cm^{-1})	Mode	β (min^{-1})	B	C	R^2
3298-3166	$\nu_{as,s}$ NH_2	$0,17 \pm 0,07$	$0,20 \pm 0,02$	$0,776 \pm 0,011$	0,9
2891	ν CH	$0,08 \pm 0,02$	$0,127 \pm 0,013$	$0,847 \pm 0,007$	0,94

IR reflectance spectrum of formamide adsorbed by spinel at 63 K in vacuum

Peak (cm^{-1})	Mode	β (min^{-1})	B	C	R^2
2348	ν_{as} CO_2	$0,305 \pm 0,001$	$0,994 \pm 0,001$	$0,006 \pm 0,001$	1
2323	ν CO	$0,556 \pm 0,001$	$0,510 \pm 0,001$	$0,490 \pm 0,001$	1

IR reflectance spectrum of formamide adsorbed by forsterite at 63 K in vacuum

Peak (cm^{-1})	Mode	β (min^{-1})	B	C	R^2
2815	...	$0,015 \pm 0,010$	$0,054 \pm 0,013$	$0,954 \pm 0,010$	0,98
2771	ν CH	$0,02 \pm 0,02$	$0,15 \pm 0,12$	$0,85 \pm 0,16$	0,8
2474	ν CO	$0,015 \pm 0,008$	$0,040 \pm 0,006$	$0,952 \pm 0,005$	0,88

Note: First column: bands that showed variations during the irradiation experiment; second column: vibrational modes; third column: the degradation rate β obtained through equation 3.1; fourth and fifth columns: fraction of molecules that interacted and did not interact with UV radiation respectively (with boundary condition B+C=1); sixth column: R^2 points to the goodness of fit with which β was obtained.

Table 3.4: **Cross section and half-lifetimes**

Formamide adsorbed by antigorite

Peak (cm^{-1})	Mode	σ (cm^2)	$t_{1/2}$ (min)
3350-3166	$\nu_{as,s}$ NH_2	$(1,9 \pm 0,6) \cdot 10^{-20}$	24 ± 4
2891	ν CH	$(1,5 \pm 0,9) \cdot 10^{-20}$	30 ± 13
2473	ν CO	$(1,7 \pm 0,8) \cdot 10^{-20}$	27 ± 8
2329	ν CO	$(1,5 \pm 0,5) \cdot 10^{-20}$	30 ± 5
1750	ν CO	$(1,2 \pm 0,8) \cdot 10^{-20}$	39 ± 19

Formamide adsorbed by TiO_2

Peak (cm^{-1})	Mode	σ (cm^2)	$t_{1/2}$ (min)
3298-3166	$\nu_{as,s}$ NH_2	$(1,14 \pm 0,64) \cdot 10^{-19}$	4 ± 2
2891	ν CH	$(0,5 \pm 0,2) \cdot 10^{-19}$	9 ± 2

Formamide adsorbed by spinel

Peak (cm^{-1})	Mode	σ (cm^2)	$t_{1/2}$ (min)
2348	ν_{as} CO_2	$(2,1 \pm 0,3) \cdot 10^{-19}$	$2,273 \pm 0,007$
2323	ν CO	$(3,7 \pm 0,6) \cdot 10^{-19}$	$1,2467 \pm 0,0002$

Formamide adsorbed by forsterite

Peak (cm^{-1})	Mode	σ (cm^2)	$t_{1/2}$ (min)
2815	...	$(1,0 \pm 0,8) \cdot 10^{-20}$	46 ± 31
2771	ν CH	$(1 \pm 2) \cdot 10^{-20}$	35 ± 35
2474	ν CO	$(1,0 \pm 0,7) \cdot 10^{-20}$	46 ± 25

Note: For bands reported in Table 3.3 that showed variations during the irradiation experiment. The cross section σ (third column) and half-lifetime $t_{1/2}$ (fourth column) were evaluated through the equations 3.3 and 3.2 respectively.

Table 3.5: **Parameters and cross section for bands formation process**

Formamide adsorbed by pyrite

Peak (cm^{-1})	Mode	α (min^{-1})	R^2	σ_f (cm^2)
2341	ν_{as} CO_2	$0,043 \pm 0,011$	0,8	$(3 \pm 1) \cdot 10^{-20}$

Formamide adsorbed by forsterite

Peak (cm^{-1})	Mode	α (min^{-1})	R^2	σ_f (cm^2)
2340	ν_{as} CO_2	$0,0121 \pm 0,0016$	0,94	$(0,8 \pm 0,2) \cdot 10^{-20}$

Note: First column: bands that increased in intensity during the irradiation experiment; second column: vibrational modes; third column: the formation rate α obtained through the equation 3.4; fourth column: R^2 points to the goodness of fit with which α was obtained; fifth column: formation cross section evaluated through equation 3.5.

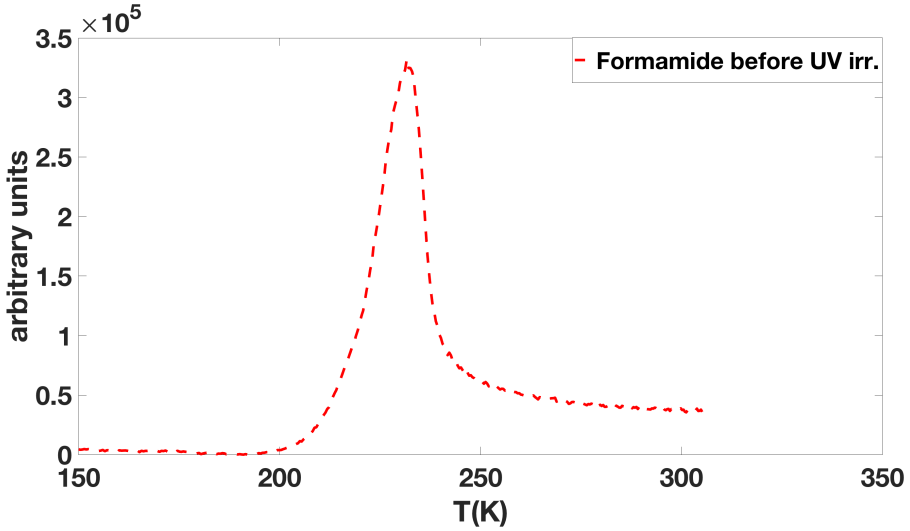

Figure 3.8: Temperature-programmed desorption curve of pure formamide before UV irradiation.

condensed onto the surface of the grains.

Usually, a TPD curve is described by the Polanyi-Wigner equation (e.g., Attard et al. 1998), as described in the first chapter, see equation 1.17. Desorption temperature (T_d) and desorption energy (E_d) were measured by fitting the TPD curves with a pre-exponential factor of 10^{12} s^{-1}, found as the best-fit value.

3.3.1 Results and discussion

Figure 3.8 shows the TPD curve of pure formamide ice at 45 a.m.u. before UV irradiation. The maximum desorption peak was found at $\sim$ 220 K. During the same experiment, it was found that also the signals at 16 a.m.u. (NH_2), 29 a.m.u. (HCO), and 44 a.m.u. (CH_2NO) increased at 220 K, the same temperature of sublimation of formamide (Figure 3.9). These signals were attributed to formamide fragments due to dissociation by the mass spectrometer.

Figure 3.10 shows the TPD curves of formamide (red line), NH_2 (black line), CH_2NO (purple line), and HCO (green line) before (dashed line) and after (continuous line) five hours of UV irradiation. We noticed that after five hours of irradiation, at $\sim$ 180 K the counts of NH_2 (black continuous line) reached the value of $3 \cdot 10^5$ arbitrary units (a.u.) and the counts of CH_2NO (purple continuous line) and of HCO (green continuous line) became $5 \cdot 10^4$

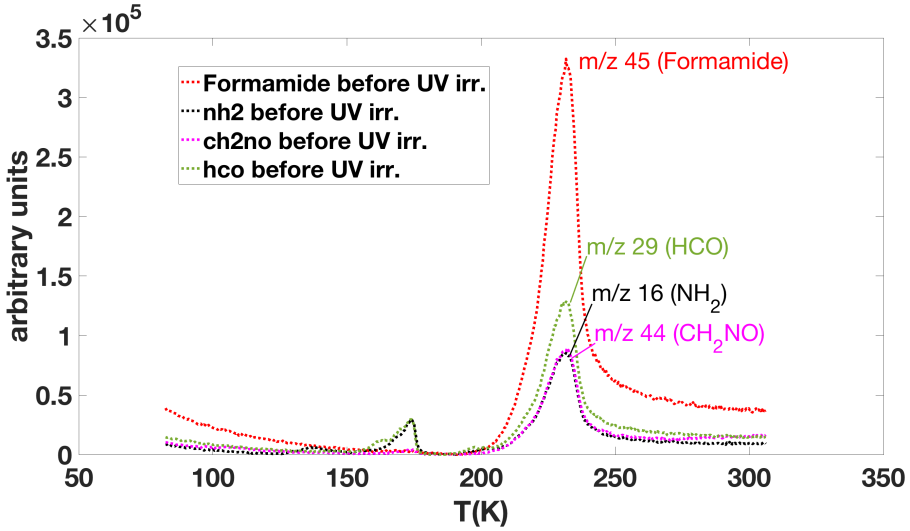

Figure 3.9: Temperature-programmed desorption curves of formamide (red dashed line - m/z 45), NH_2 (black dashed line - m/z 16), CH_2NO (purple dashed line - m/z 44) and HCO (green dashed line - m/z 29) before UV irradiation.

a.u. At this temperature, formamide was not yet desorbed, but it was still condensed on the cold finger of the cryostat. Therefore, these fragments were not due to the dissociation of formamide inside the mass spectrometer, but they were photoproducts due to UV irradiation. In our experiment, the desorption temperature of water occurred at 180 K. The presence of water was due to residual deposition in the high vacuum chamber. It is reasonable to think, therefore, that the sublimation of water ice was responsible for releasing more volatile species. This result is probably a close representation of what can happen in space. The capability of water to trap molecules with lower sublimation temperatures is a well-known process occurring in space and it can influence the gas-phase composition of the interstellar medium (Ángel Satorre Aznar et al., 2010). Figure 3.10 also shows that, after UV irradiation, there was an increase in NH_2 counts at 150 K (maximum value of $1 \cdot 10^5$ a.u.). Also, this peak is connected to water. At 150 K, there is the conversion of cubic crystalline ice to hexagonal ice (Collings et al., 2004), which is responsible for the desorption of more volatile species trapped in the water ice structure. From these results, it seems that desorption of NH_2, HCO, and CH_2NO was driven by the transition of water ice structure. The same phenomenon probably occurs in the space where water is the most abundant molecule. The TPD curve of NH_2 after irradiation shows a small

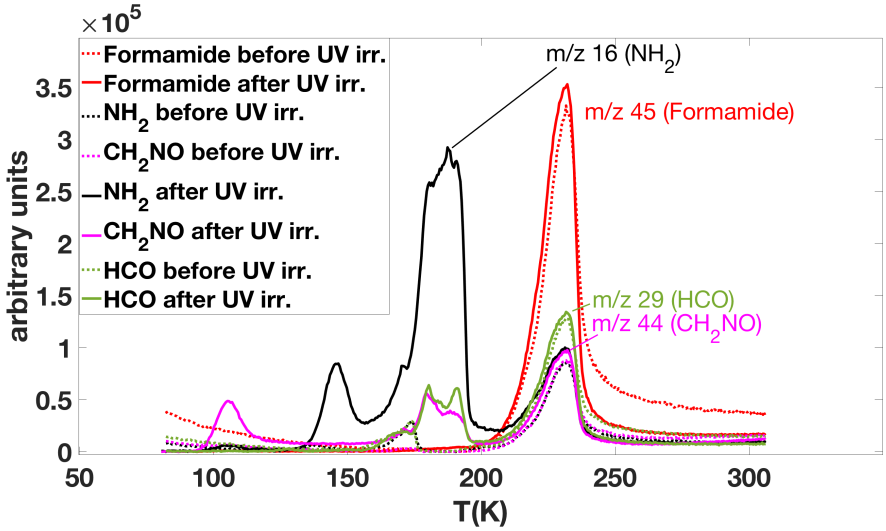

Figure 3.10: Temperature-programmed desorption curves of formamide (red line - m/z 45), NH_2 (black line - m/z 16), CH_2NO (purple line - m/z 44) and HCO (green line - m/z 29) before (dashed line) and after (continuous line) five hours of UV irradiation.

increase in the counts even at a lower temperature ∼100 K; this desorption feature is also present in the TPD curve of CH_2NO where it reached the value of $5 \cdot 10^4$ a.u. (Figure 3.10). We found that CH_2NO in the UHV regime desorbed at ∼100 K. Once desorbed, it split into its fragments for dissociation by mass spectrometry, and therefore the desorption feature of NH_2 at 100 K is due to the fragmentation of CH_2NO inside the mass spectrometer.

Going forward with our investigation, we reproduced the condensation, irradiation, and desorption experiments with a substrate of TiO_2 dust. Figure 3.11 shows the differences in TPD curves between pure formamide and in the presence of TiO_2 grains. We observed evidence for a change in desorption temperature between the two experiments. Formamide desorption from TiO_2 dust occurred at higher temperatures, that is, around 30 K above the temperature at which desorption takes place for pure formamide. A higher desorption temperature is direct evidence of the interaction described by the Van der Waals forces that were occurring between the molecule and the grains. The molecule interacts and diffuses into the grains and this is confirmed by the values of the binding energy. When formamide desorbed directly from the cold finger of the cryostat (copper chromate surface), the binding energy found was $(7.5 \pm 0.7) \cdot 10^3$K; while when it desorbed from TiO_2 dust, the binding energy found was higher $(1.18 \pm 0.07) \cdot 10^4$K, as reported

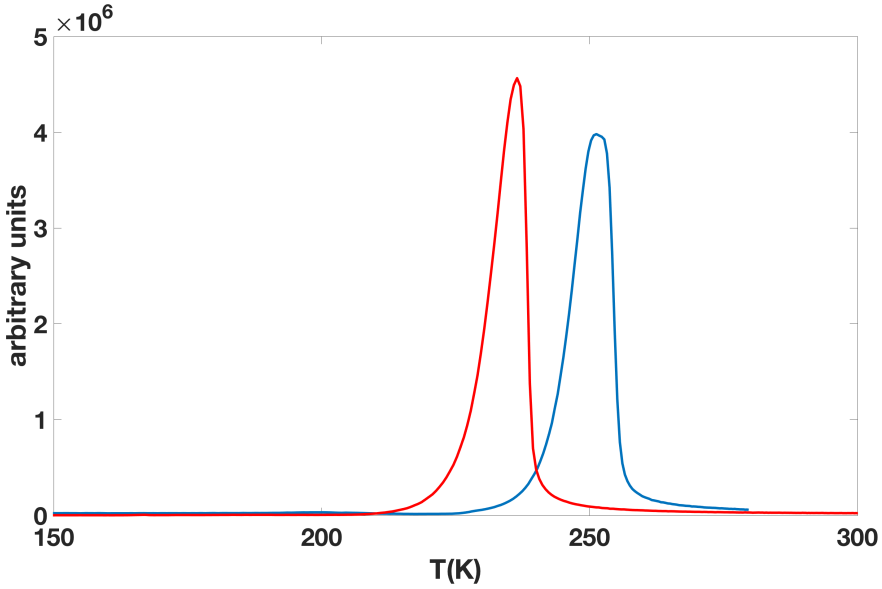

Figure 3.11: Red line: TPD curve of pure formamide condensed on the cold finger of cryostat; Blue line: TPD curve of formamide condensed on TiO_2.

Table 3.6: **Best-fit values of TPD curves**

	Before UV	After UV
Pure formamide	$E_d/R = (7.5 \pm 0.7) \cdot 10^3$K	$E_d/R = (5.9 \pm 0.3) \cdot 10^3$K
Formamide on TiO_2	$E_d/R = (1.18 \pm 0.07) \cdot 10^4$K	$E_d/R = (1.35 \pm 0.08) \cdot 10^4$K

in the second column of Table 3.6.

Temperature-programmed desorption curves of formamide and fragments condensed on TiO_2 before and after UV radiation are shown in Figure 3.12. Interestingly, in presence of TiO_2, all the TPD curves shifted towards higher temperatures after the irradiation experiment. Before UV radiation, formamide condensed on the surface of TiO_2 desorbed at 250.8 K (red dashed line Figure 3.12 a); after UV radiation it desorbed at 253.2 K (red continuous line Figure 3.12 a). Temperature-programmed desorption curves for major fragments reported in Fig.3.12 (b, c, and d) showed the same shift to the right.

Table 3.6 shows the values found for desorption energies before and after UV irradiation, evaluated with equation 1.17.

In recent years, formamide has been observed in low-mass star formation environments such as shocked regions by protostellar jets (e.g., Codella et al.

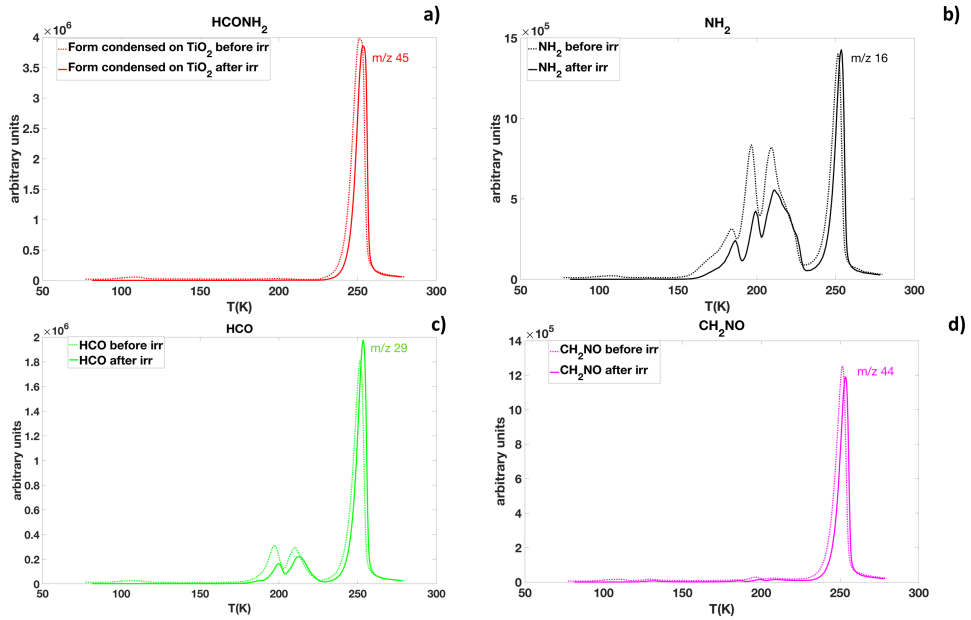

Figure 3.12: (a) TPD curves of formamide (m/z 45) condensed on TiO_2 before (dashed lines) and after (continuous lines) 4 hours UV irradiation; (b), (c), and (d): TPD curves of major fragments (NH_2, HCO and CH_2NO respectively) before (dashed lines) and after (continuous lines) 4 hours of UV radiation.

2017), where the presence of a large number of molecules is due to mechanical release by gas–grain collisions and grain–grain collisions (López-Sepulcre et al. 2019; Codella et al. 2017), and hot corinos (Kahane et al. 2013; López-Sepulcre et al. 2015; Marcelino et al. 2018; Imai et al. 2016; Oya et al. 2017; Lee et al. 2017), the inner, compact (< 100 AU), and hot (>100 K) regions of some Class 0 protostars (Ceccarelli 2004; Ceccarelli et al. 2007; López-Sepulcre et al. 2019). Formamide has only been detected in protostars that host a hot corino (Sakai et al. 2013; López-Sepulcre et al. 2019). This evidence implies that the presence of formamide is strictly linked to hot (>100 K) regions where thermal desorption is the responsible process for sublimation of frozen mantles into the gas phase. This is in very good agreement with our TPD analysis which requires a temperature of 220 K for thermal desorption of formamide (Figure 3.8). The desorption energies published by Wakelam et al., 2017, who proposed a new model to compute the binding energy of species to water ice surfaces, are adopted in the chemical model of Quénard et al., 2018, which shows that formamide needs environments with temperatures of greater than 200 K to be present in the gas phase, otherwise it remains frozen on dust grains. However, our experiments show that these energies, consistent with those we found for formamide desorbed directly from the cold finger, are greater when considering adsorption on grain surfaces: using TiO_2 grains, the binding energies increased (Table 3.6) and the sublimation temperature was 30 K higher than that found for pure formamide (Figure 3.11). Therefore, in the chemical models of sublimation, it is essential to take into account physisorption of iCOMs on grain surfaces and their diffusion in order to correctly describe the desorption process, that is, to constrain desorption temperatures and binding energies.

In a temperature - programmed desorption experiment, the temperature goes from low values to over 300 K in fifteen, twenty minutes. In these experiments, the heating rate was half kelvin per second. In a hot cores, the heating rates are much slower. The differences in time scales between the laboratory (minutes, hours) and space (centuries) lead to lower desorption temperatures in space. In the work of (Collings et al., 2004), the desorption profiles of water ice were simulated changing the heating rate. The authors found that the water desorption temperature can range from 180 K at a typical laboratory heating rate to 105 K at 1 K·century^{-1}, heating rate in hot cores. Following his work and starting from the TPD curve obtained in laboratory for pure formamide, we simulated the desorption profiles of formamide as the heating rate changes. Figure 3.13 shows that for pure formamide, the desorption temperature ranges from 220 K at a 0.6 K·sec^{-1} heating rate as measured in the laboratory, to 137 K at 1 K·century^{-1}, the typical heating rate of hot cores.

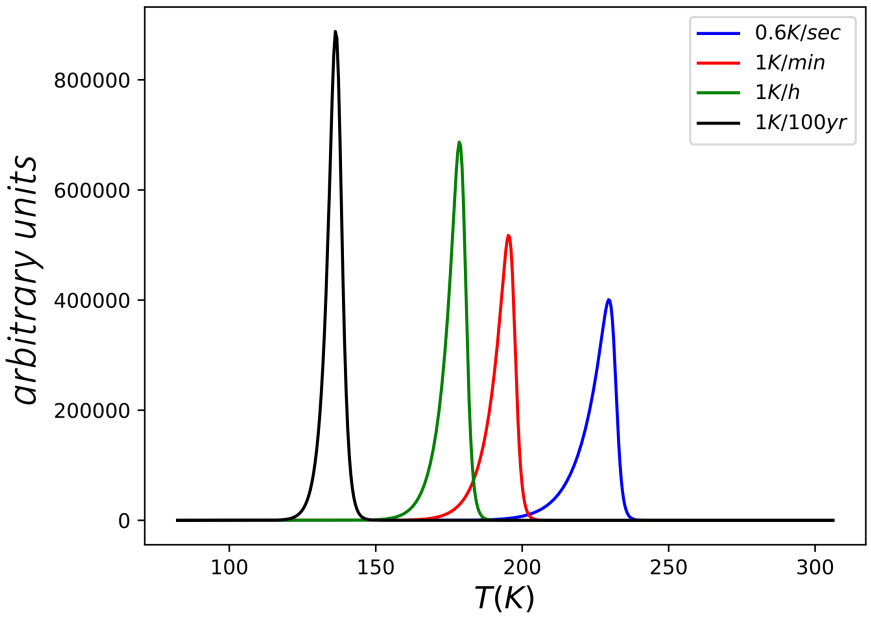

Figure 3.13: Desorption profiles of pure formamide as the heating rate changes.

Furthermore, our experiments show something more than the desorption temperature and the binding energy of formamide. The molecular fragments observed in the gas phase can be used to indirectly measure the presence of formamide: we found that during the desorption experiment, NH_2 counts reached the value of $3 \cdot 10^5$ a.u. at 180 K, six times higher than HCO and CH_2NO counts (Figure 3.10), and during the TiO_2 grain desorption experiment, NH_2 counts reached the value of $8 \cdot 10^5$ a.u. at 200 K, four times higher than HCO counts (Figure 3.12). Therefore, these ratios between the abundance of NH_2 and the abundance of HCO and CH_2NO (e.g., $[NH_2]/[HCO] \sim 4$) can be an indicator of the presence of formamide.

Chapter 4

Thermal desorption of acetaldehyde and acetonitrile from olivine dust

In the previous chapter, we simulated thermal desorption of formamide, a physical process responsible for its presence in the gaseous phase in hot regions (>100 K), such as hot corinos, where formamide has been observed several times. To date, formamide has not been detected in protoplanetary disks, but the next step for the scientific community is surely to search for formamide in this kind of object. Observing iCOMs in protoplanetary disks is a major challenge, as they are the place where planets are formed that could inherit their chemical complexity. In the introduction, we have already explained the difficulty to observe iCOMs in protoplanetary disks around low-mass Sun-like stars, since the region in which the temperature reaches the desorption values of water and iCOMs is very close to the star (less than 5 AU). This region is difficult to solve due to its small size and very high sensitivity observations will be required in the future. For these reasons to date, few iCOMs have been observed in protoplanetary disks, only methanol (Walsh et al. 2016), acetonitrile (e.g., Öberg et al. 2015), and formic acid (Favre et al. 2018). As announced in the introduction, the number of iCOMs detected in protoplanetary disks has increased thanks to observations of the protoplanetary disk around the star V883 Ori. In this type of disk, FU Ori disks, the young central star undergoes a sudden increase in brightness which leads to heating of the disk and to a quick expansion of the molecular snow lines to larger radii. In this type of object, the desorption of molecules is certainly thermal. Even if formamide was not observed, five iCOMs, thermally desorbed from the disk, were detected (Lee et al. 2019), including acetaldehyde and acetonitrile.

Acetaldehyde and acetonitrile are the two iCOMs investigated in the second part of my Ph.D. project. This chapter collects our results published on the "Thermal desorption of astrophysical relevant ice mixtures of acetaldehyde and acetonitrile from olivine dust" (Corazzi et al. 2021). These laboratory experiments are made in the framework of understanding how the solid phase interactions between molecules and grain surfaces can significantly influence the thermal desorption process and so the presence of molecular species in the gas phase. We simulated the thermal desorption process through TPD analysis. Up to now, TPD experiments have been carried out mainly from graphite and amorphous water ice surfaces (e.g., Collings et al. 2004, Hama et al. 2011, Shi et al. 2015, Chaabouni et al. 2017). Therefore as far as we know, TPD experiments from grain surfaces are lacking in the literature, but grain-molecule interaction is a fundamental aspect: mineral matrices can selectively adsorb, protect, and allow the iCOMS concentration on their surface. Molecules can interact on the mineral surface through Van der Waals-like forces and dipole-dipole interactions as it has been routinely demonstrated through vibrational spectroscopic methods such as infrared and Raman spectroscopy (Kloprogge, 2018). Moreover, molecules can diffuse inside the grains when the submicron interstellar grains begin to accrete into hundreds of microns fluffy dust. The presence of grains can therefore influence the desorption and release of the iCOMs in the gas phase and therefore, the molecule-grain interaction cannot be neglected in thermal desorption studies.

Through this work, we performed for the first time TPD experiments of acetonitrile and acetaldehyde both pure and mixed with water from micrometric grains of silicate olivine ($(Mg,Fe)_2SiO_4$) used as dust analog on which the icy mixtures were condensed at cryogenic temperatures.

4.1 Acetaldehyde and Acetonitrile

Acetaldehyde (CH_3COH, molecular weight of 44 a.m.u.) is one of the five complex molecules that are thermally desorbed by the FU Ori system V883 Ori (Lee et al., 2019). It was also observed in the interstellar medium, in low- and high-mass protostars (e.g.,Bianchi et al. 2019, Guzman et al. 2018), in hot corinos (e.g., Taquet et al. 2015, Codella et al. 2016) and comets (e.g., Biver et al. 2019). The reaction pathways involving the iCOMs described by the C_2H_nO formula, such as acetaldehyde (CH_3CHO), are still matter of debate (Chuang et al., 2020). Many works show how acetaldehyde can be synthesized directly on the grain surfaces (e.g., Garrod et al. 2006, Öberg et al. 2009) starting from HCO and CH_3 radicals on CO-rich ices (Lamberts et

al., 2019) or through surface chemistry at 10 K on C_2H_2 ices with H-atoms and OH-radicals (Chuang et al., 2020) or through UV photoprocessing of interstellar ice analogs (Martín-Doménech et al., 2020). Other works claimed that it is not clear whether acetaldehyde is formed on the icy surfaces of interstellar grains or through gas phase reactions (Enrique-Romero et al., 2016).

Acetonitrile (CH_3CN, molecular weight of 41 a.m.u.) was found in many regions both within and outside the Solar System: in the Titan atmosphere (e.g., Cordiner et al. 2015, Iino et al. 2020, Thelen et al. 2019), in the comet 67P / Churyumov-Gerasimenko (Goesmann et al., 2015), in the cometary coma of Hale - Bopp (Woodney et al., 2002), in the molecular cloud $SgrB_2(N)$ (e.g., Willis et al. 2020), in the high and low mass protostars (e.g., Taniguchi et al. 2020, Andron et al. 2018), in hot cores (e.g., Bogelund et al. 2019), in the protoplanetary disks (e.g., Öberg et al. 2015, Bergner et al. 2018) and it is among the five iCOMs desorbed by the frozen mantle of the circumstellar disk around the V883 Ori protostar (Lee et al., 2019). Moreover, it is among the most commonly detected organic molecules in disks (Le Gal et al., 2019). To explain the large abundance observed in the gas phase of acetonitrile, many works invoked chemical reactions occurring on the surface of the grains (Öberg et al. 2015, Loomis et al. 2018).

4.2 Laboratory procedure, samples preparation and thermal desorption diagnostic

In these thermal desorption experiments, we were able to reach ultra high vacuum (UHV) regimes. The obtained pressure in the chamber was of P$\sim 6.68 \cdot 10^{-10}$ mbar. The UHV chamber was assembled with feed-throughs for gas phase deposition from a pre-chamber (P $\sim 10^{-7}$ mbar) where the samples were prepared. The CH_3COH and CH_3CN molecules were purchased from Sigma Aldrich, Merck corporation with a purity 99.5%. Pure H_2O, CH_3CN, CH_3COH, and mixtures CH_3CN:H_2O (1:2), CH_3COH:H_2O (1:2), CH_3CN:CH_3COH (1:6), and CH_3CN:CH_3COH:H_2O (1:1:3) were prepared. To obtain the gas mixtures with the described proportions, the gas mixing was controlled by their partial pressures inside the pre-chamber. The chamber interfaces with the Hiden Analytical 3F RC 301 Pic Quadrupole Mass Spectrometer and with ARS closed cycle helium cryocooler able to get a temperature of 17 K.

We first studied the thermal desorption of the samples condensed directly on the cold finger of the cryostat at 17 K. Then, to simulate a process that

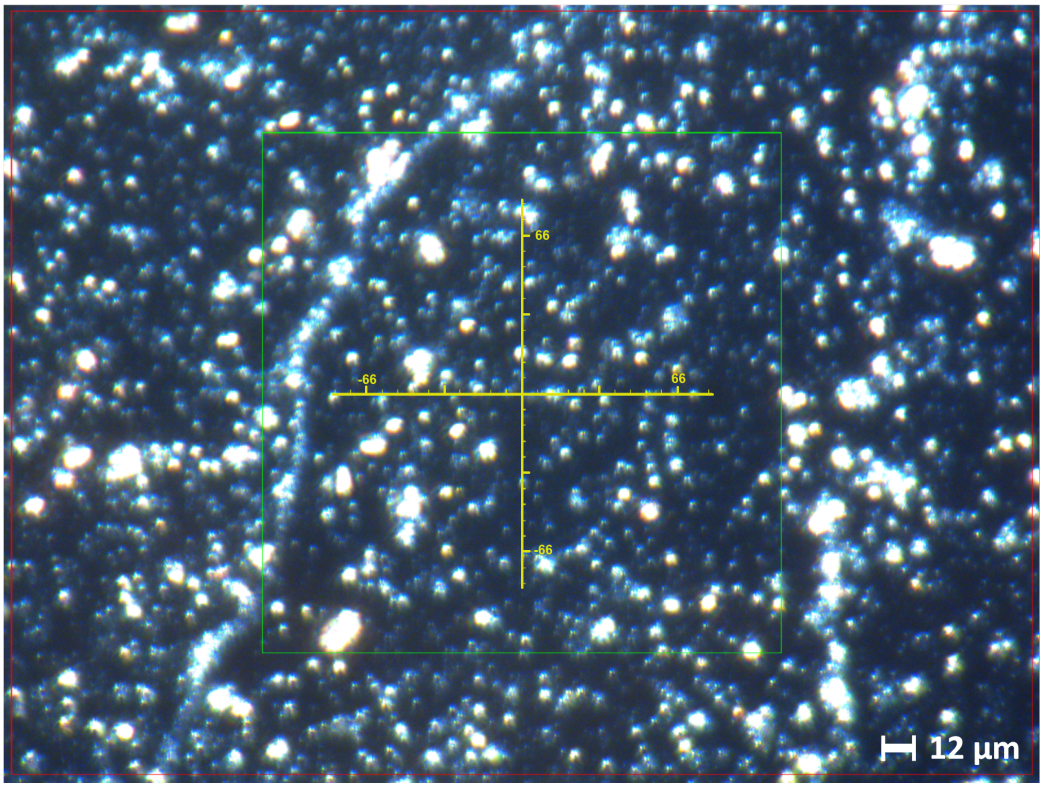

Figure 4.1: Olivine grains smaller than $5\mu m$. The image was obtained with the Hyperion microscope.

can realistically take place in hot star-forming regions, we carried out the thermal desorption experiments of pure molecules and mixtures condensed on micrometric grains of olivine. So, the cold finger was covered with hundreds micron thick layer of olivine grains with size smaller than 5 μm used as a substrate. To obtain in the laboratory substrate of suitable dimensions, terrestrial bulk olivine was first ground using a planetary mill Retsch PM 100. In this way, we obtained dust of different grain sizes. To select micrometric grains, two procedures were adopted: dry sieving to select grains with size d<20 μm and then a methanol sedimentation procedure to select grains with even smaller dimensions. The use of methanol as a solvent is justified by its high volatility, but also because it is a polar solvent able to remove organic contamination from the natural mineral. With sedimentation, grains with dimensions d<5 μm were selected. The grain size measurement was carried out with the Bruker Hyperion 1000 microscope. Figure 4.1 shows the image of micrometric olivine dust.

Once the gas mixture of iCOMs was prepared in the pre-chamber following the partial pressures, it was deposited through a valve system inside the UHV chamber on the cold finger cooled to 17 K (clean or covered with the olivine substrate). In all measurements during the gas mixtures deposition, we observed that the pressure in the UHV chamber increased from $6.68 \cdot 10^{-10}$ mbar without ever exceeding a maximum pressure of 10^{-8} mbar. The pressure maintained this maximum value for about 1 second. The surface exposure to a gas is generally measured by the Langmuir unit (L). Assuming a sticking coefficient equal to 1, i.e., each gas molecule that reaches the surface sticks to it, 1 L ($1L = 10^{-6}$torr$\cdot$ sec) results in the formation of a monolayer of gas molecules adsorbed on the surface. Since during the deposit the maximum pressure in the UHV chamber was 10^{-8} mbar for one second, we could say that we were in a regime of 0.01 L, so we were in a substrate regime. In the following sections, we report the amounts of the molecules adsorbed on the surface in partial pressure instead of L unit since the first one is a direct measure in our experimental apparatus.

After condensation, the sample was heated at a constant rate of 1.21 K$\cdot$ sec^{-1}. As the cold finger warmed, the condensed molecules desorbed, entered the mass spectrometer, and were detected. We followed the signal detected by the mass spectrometer as the temperature increased for selected masses from 1 to 300 m/z and so, the TPD curves were obtained. The desorption temperature (T_d) and the desorption energy (E_d) were measured by fitting the TPD curves with the Polanyi-Wigner equation (e.g., Attard et al. 1998). In the Polanyi-Wigner equation (see equation 1.17), we used a pre-exponential factor A of 10^{12} sec^{-1}, found as best fit value for both acetaldehyde and acetonitrile.

4.3 Thermal desorption from olivine grains results

In this section, we report the results obtained with the seven samples listed above.

Figures 4.2 and 4.3 show in detail the TPD curves of pure H_2O (18 m/z) and pure CH_3CN (41 m/z) desorbed both from the cold finger of the cryostat (blue curves) and from micrometric olivine grains (yellow curves). As visible in Figure 4.2, when the molecules desorbed directly from the cold finger of the cryostat, only one desorption peak was obtained. On the other hand, when the same number of molecules (i.e., same partial pressures) condensed on the micrometric grains of olivine, two different desorption peaks appeared.

Specifically, the first desorption peak was found at a temperature lower than that found in the absence of grains i.e., when desorption occurred from the smooth nickel-plated cold finger. Water-ice TPD measurement (blue curve in Figure 4.2) shows that as the temperature increased, the water molecules began to desorb at around 110 K until they reach the desorption peak at 141.2 K, with the counts detected by the mass spectrometer increasing from $6.6 \cdot 10^3$ to $5.2 \cdot 10^4$ counts·sec^{-1}. At 165 K, all of the water molecules deposited were desorbed, and as the temperature increased further, the counts decreased until they returned to the initial value. In the presence of the olivine substrate (Figure 4.2, yellow curve), we observed that 50% of the water molecules desorbed at 128.5 K where the signal at 18 m/z increased to $3.2 \cdot 10^4$ counts·sec^{-1}. The rest of the water ice desorbed in a wider temperature range, which shows a peak at 166.4 K. If in the absence of grains at 160 K the mass counts returned to the initial value, in presence of grains the counts were still higher than the background with a value of $2.2 \cdot 10^4$ counts·sec^{-1} at 207 K and $1.6 \cdot 10^4$ counts·sec^{-1} still at 300 K, showing a gradual and prolonged desorption of water molecules from the dust grains. This result reveals that the water remains trapped by the olivine grains showing a desorption drift.

We observed a similar desorption behavior for CH_3CN. In this case, the partial pressure of the pre-chamber was 1 mbar. Figure 4.3 shows that as the temperature increased, the CH_3CN molecules started to desorb from the cold finger at around 100 K, reaching the maximum peak at 124.0 K where the mass counts got the value of $1.27 \cdot 10^4$ counts·sec^{-1}. At higher temperatures, the counts decreased and returned to the initial value of the background already at 150 K. TPD curve shows a single desorption peak at 124.0 K where all the CH_3CN molecules deposited were desorbed from the cold finger of the cryostat and passed into the gas phase. Depositing the same amount of CH_3CN onto the olivine dust, the mass counts of the first peak of the yellow curve increased to $3.2 \cdot 10^4$ counts·sec^{-1} and 30% of molecules desorbed with a delay at 190.5 K. The yellow curve showed a second desorption peak of intensity $3 \cdot 10^3$counts·sec^{-1}.

So in both cases, H_2O and CH_3CN presented a first desorption peak followed by a second one at higher desorption temperatures, 166.4 K for H_2O and 190.5 K for CH_3CN, and hence with higher desorption energies. Table 4.1 shows the best-fit values for the desorption temperatures and energies obtained through the Polanyi - Wigner equation. Furthermore, during the water TPD measurement, the first peak preceded the desorption peak found in the absence of grains by more than 10 K, while during the desorption of CH_3CN we did not observe this shift.

Figures 4.4 and 4.5 show the thermal desorption of the ice mixture CH_3CN:H_2O (1:2). Figure 4.4 shows both the TPD curve of CH_3CN (signal at 41 m/z) desorbed from the smooth nickel-plated cold finger (blue curve) and that from olivine grains (yellow curve). In this experiment, CH_3CN was first mixed with water in the pre-chamber to obtain a 1:2 ratio and then deposited in the UHV chamber. Although acetonitrile was in a mixture with water, its TPD curves revealed similar results to those found when the molecule was deposited alone in the absence and presence of olivine. The blue curve (thermal desorption without grains) showed that the CH_3CN molecules started to desorb at 100 K reaching the maximum desorption peak at 121.4 K, and at higher temperatures, the signal decreased and returned to the initial value already at 150 K. The yellow curve shows the thermal desorption from olivine dust. It shows that 50% of the deposited acetonitrile molecules desorbed at the same temperature found in the absence of grains and 30% of molecules desorbed with a drift at 196.4 K and gradually dropping to the initial values. In presence of grains, 15% of molecules continued to desorb until 300 K, showing a gradual release of the molecules from the grains.

Figure 4.5 shows the counts detected at 44 m/z during the desorption of the mixture from the cold finger (blue curve) and from olivine grains (yellow curve). The blue curve showed only one desorption peak at 121.4 K. At this temperature, all molecules were already desorbed and at 150 K, the signal already returned to the initial value. The yellow curve, which is the desorption from grains, exhibited a first peak at the same position as the desorption peak found in the absence of grains, but lower in intensity, and a shoulder at a higher temperature. In the absence of grains, all molecules of molecular weight 44 m/z desorbed around 120 K (signal intensity of $1 \cdot 10^4$ counts·sec^{-1}). Instead, in the presence of grains, the first peak of intensity $5 \cdot 10^3$ was observed, so only 50% of the molecules desorbed from the grains. The second desorption peak was observed at 193.0 K.

The TPD curve at 44 m/z showed its desorption peak at the same temperature of acetonitrile and with higher peak intensity (the blue curves show an intensity of $3 \cdot 10^3$ counts·sec^{-1} at 41 m/z and of 10^4 at 44 m/z). The simplest assignment for 44 m/z is CO_2, a common contaminant. However, we also carried out different background measurements in which we followed the signals detected by the mass spectrometer from 1 to 300 a.m.u as the temperature increased. From the background measurements, we found a signal at 44 m/z lower than 10^2 counts·sec^{-1}, which is two orders of magnitude lower than the signal we observed during the mixture desorption. Even if we can not exclude that background CO_2 could contribute to the mass signal, its contribution can not justify the peak intensity observed. A possible

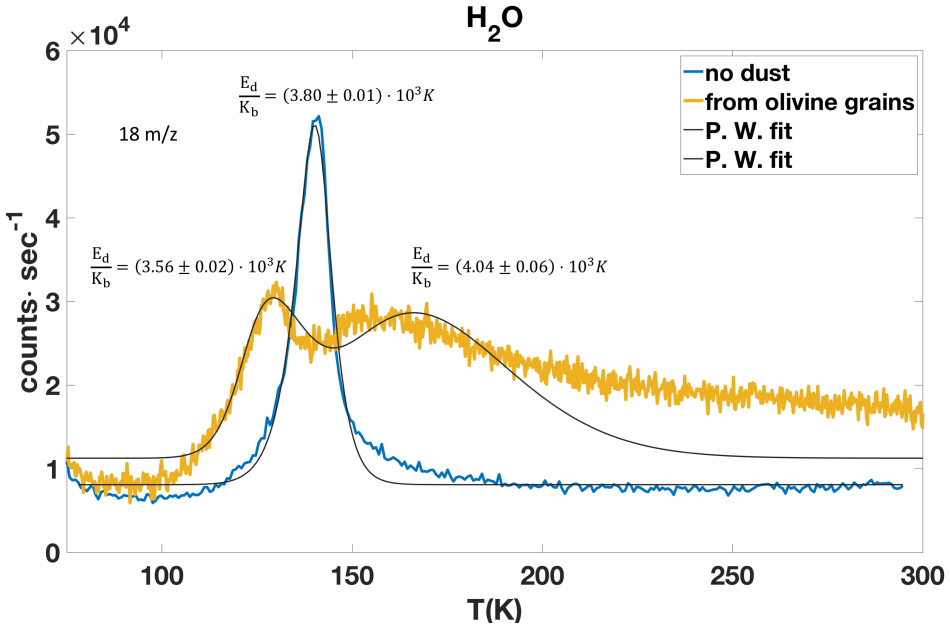

Figure 4.2: The figure shows two experiments. In both experiments, we deposited in the UHV chamber the same amount of water (partial pressure of water in the pre–chamber 0.68 mbar). **Blue curve**: water desorption directly from the cold finger of cryostat cooled to 17 K. **Yellow curve**: water desorption from olivine dust. In presence of olivine, we found a first desorption peak lower than that found in the absence of grains and then we found a second wider desorption peak. In presence of crystalline grains, the molecules did not desorb all together at T_{des}: some of them desorbed but others remained tied to the grains and desorbed with a delay at a higher temperature. This second desorption shows the interactions between the molecules and the grains. **Black lines**: the TPD curves were fitted through the Polanyi - Wigner equation.

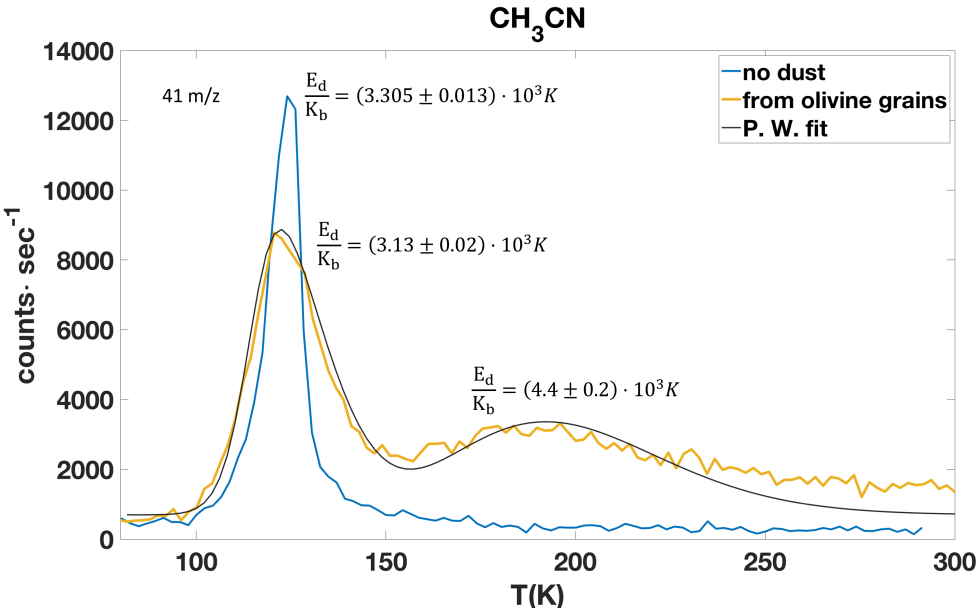

Figure 4.3: The figure shows two experiments. In both experiments, we deposited in the UHV chamber the same amount of acetonitrile CH_3CN (partial pressure of CH_3CN in the pre–chamber 1 mbar). **Blue curve**: CH_3CN desorption directly from the cold finger of cryostat cooled to 17 K. **Yellow curve**: CH_3CN desorption from olivine dust. In presence of olivine, we found a first desorption peak lower in intensity than that found in the absence of grains and then we found a second wider deosrption peak, that shows the interactions between the molecules and the grains. **Black line**: the double desorption was fitted through the Polanyi - Wigner equation.

Table 4.1: **Best-fit values of TPD curves**

	No dust		**Olivine grains**	
Ice mixture ratios	$\mathbf{T_d(K)}$	$\mathbf{E_d/K_b(K)}$	$\mathbf{T_d(K)}$	$\mathbf{E_d/K_b(K)}$
Pure water				
18 m/z	141.2	$(3.80 \pm 0.01) \cdot 10^3$	128.5	$(3.56 \pm 0.02) \cdot 10^3$
	...	...	166.4	$(4.04 \pm 0.06) \cdot 10^3$
CH_3CN				
41 m/z	124.0	$(3.305 \pm 0.013) \cdot 10^3$	124.6	$(3.13 \pm 0.02) \cdot 10^3$
	...	...	190.5	$(4.4 \pm 0.2) \cdot 10^3$
CH_3COH				
44 m/z	104.9	$(2.847 \pm 0.003) \cdot 10^3$	103.0	dissociated in HCO and CH_3
15m/z	...	...	103.0	$(2.665 \pm 0.014) \cdot 10^3$
	...	...	170.2	$(3.4 \pm 0.8) \cdot 10^3$
29m/z	...	...	103.0	$(2.673 \pm 0.010) \cdot 10^3$
	...	...	170.2	$(3.5 \pm 0.5) \cdot 10^3$
CH_3CN:H_2O (1:2)				
41m/z	121.4	$(3.257 \pm 0.007) \cdot 10^3$	126.2	$(3.36 \pm 0.03) \cdot 10^3$
	...	...	196.4	$(5.91 \pm 0.15) \cdot 10^3$
44 m/z	121.4	$(3.304 \pm 0.005) \cdot 10^3$	124.0	$(3.34 \pm 0.03) \cdot 10^3$
	...	...	193.0	$(4.80 \pm 0.07) \cdot 10^3$
CH_3COH:H_2O (1:2)				
44 m/z	107.5	$(3.079 \pm 0.011) \cdot 10^3$	108.2	dissociated
CH_3CN:CH_3COH (1:6)				
29 m/z	111.2	$(2.955 \pm 0.005) \cdot 10^3$	110.7	(2.89 ± 0.02)
	...	...	149.4	$(3.1 \pm 0.7) \cdot 10^3$
15 m/z	111.2	$(2.967 \pm 0.005) \cdot 10^3$	110.7	$(2.88 \pm 0.02) \cdot 10^3$
	...	...	149.4	$(3 \pm 1) \cdot 10^3$
41 m/z	130.7	$(3.380 \pm 0.012) \cdot 10^3$	122.9	$(3.26 \pm 0.04) \cdot 10^3$
	...	...	190.2	$(4.4 \pm 0.3) \cdot 10^3$
44 m/z	111.2-130.7	$(3.404 \pm 0.012) \cdot 10^3$	110.7-122.9	$(2.80 \pm 0.05) \cdot 10^3$
	...	...	190.3	$(4.3 \pm 0.2) \cdot 10^3$
CH_3CN:CH_3COH:H_2O(1:1:3)				
44m/z	121.9	$(3.275 \pm 0.018) \cdot 10^3$	123.0	$(3.33 \pm 0.04) \cdot 10^3$
	...	...	206.6	$(4.7 \pm 0.3) \cdot 10^3$
41 m/z	120.0	$(3.24 \pm 0.03) \cdot 10^3$	123.0	$(3.36 \pm 0.07) \cdot 10^3$
	...	...	207.5	$(5.1 \pm 0.5) \cdot 10^3$

Note: The first column shows the samples analyzed and the ratios between the ice mixture components. In the second, the temperature of the maximum desorption peak T_d and the desorption energy E_d/K_b of the ice mixtures condensed directly on the cold finger of the cryostat are reported. Third column is dedicated at the ice mixture desorption from olivine dust and here, the temperatures and desorption energies of the two observed peaks are reported. The desorption energies are given in kelvin, as E_d/K_b, where K_b is Boltzmann's constant.

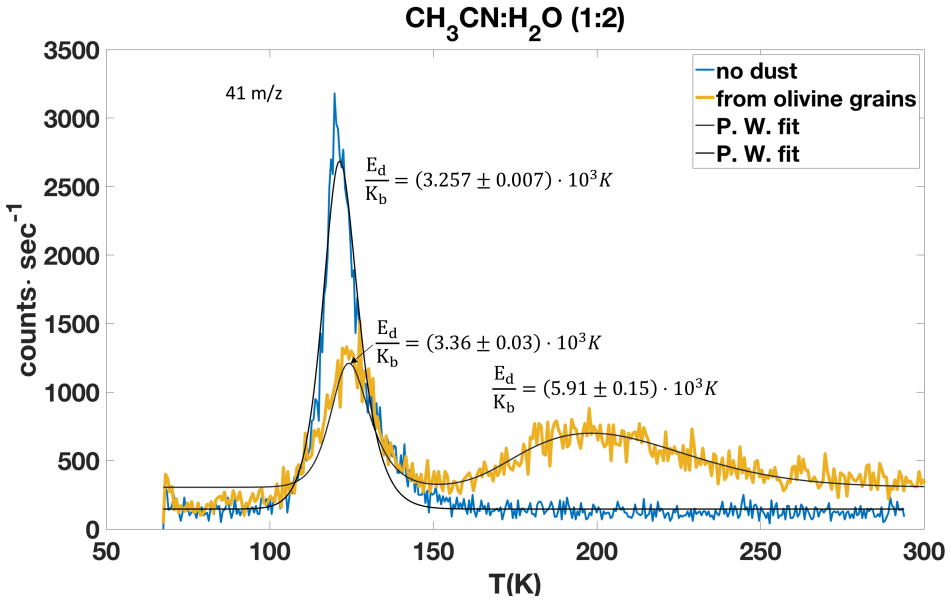

Figure 4.4: The figure shows two experiments. In both experiments, we deposited in the UHV chamber an ice mixture CH_3CN:H_2O (1:2). **Blue curve**: CH_3CN desorption directly from the cold finger of cryostat cooled to 17 K. **Yellow curve**: CH_3CN desorption from olivine dust. In presence of olivine, we found a first desorption peak lower in intensity than that found in the absence of grains and then we found a second wider desorption profile. During the gas deposition, molecules once colliding to the cold grain surface can diffuse through the grains occupying more energetic favorable regions within the dust layer. During the TPD process, such molecules are retained to higher temperatures before to be released to the gas phase. **Black lines**: the TPD curves were fitted through the Polanyi - Wigner equation.

interpretation of this intense signal at 44 m/z is that it could be associated with the cracking in the mass spectrometer of dimethylamine CH_3-NH-CH_3 (45 m/z). In support of this interpretation, we observed a signal at 45 m/z with the same ratio compared to the signals at 41 and 44 m/z as found on the National Institute of Standards and Technology (NIST) Chemistry Webbook. The presence of dimethylamine could be a consequence of acetonitrile hydrogenation (e.g., Nguyen et al. 2019), but this interpretation will need to be further investigated and verified.

Figure 4.6(a) exhibits two experiments: in both cases, the same amount of pure CH_3COH (partial pressure of 0.6 mbar) was deposited directly on

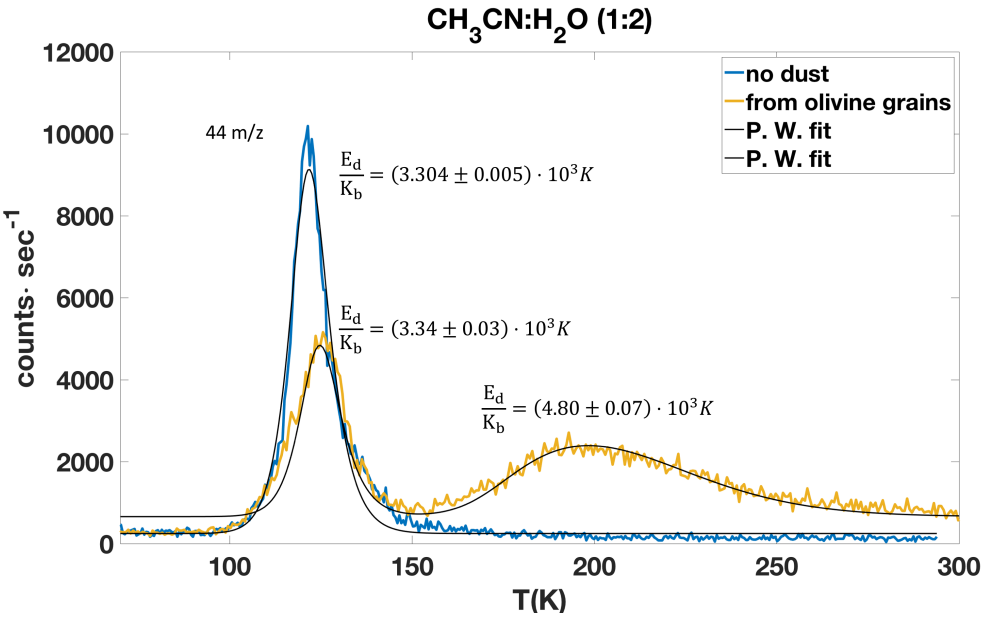

Figure 4.5: The figure shows two experiments. In both experiments, we deposited in the UHV chamber an ice mixture CH_3CN:H_2O (1:2). **Blue curve**: m/z 44 desorption directly from the cold finger of cryostat cooled to 17 K. **Yellow curve**: m/z 44 desorption from olivine dust. **Black lines**: the TPD curves were fitted through the Polanyi - Wigner equation.

the cold finger of the cryostat (blue curve) and on an olivine substrate (yellow curve), respectively. The blue curve shows us that as the temperature increased, the acetaldehyde molecules (signal at 44 m/z) already started to desorb around 90 K until reaching the desorption peak at 104.9 K (the counts detected by the mass spectrometer increased from $2 \cdot 10^2$ to $4.24 \cdot 10^3$ counts·sec^{-1}, one order of magnitude greater). At this temperature, all the acetaldehyde molecules deposited were already desorbed and at higher temperatures, the counts decreased until they returned to the initial value already around 130 K. So, a deposit of 0.6 mbar of CH_3COH on the cold finger of the cryostat in the ultra high vacuum regime provided a 44 m/z signal of $4.24 \cdot 10^3$ counts·sec^{-1} intensity at 104.9 K, showing that around 100 K all the molecules were already desorbed from the surface. On the other hand, when we deposited 0.6 mbar of CH_3COH on olivine dust (yellow curve), we found that the CH_3COH signal was significantly reduced. At the same temperature found without grains ($\sim$ 104 K), the yellow TPD curve revealed a slight increase in the intensity signal that ranged from $2 \cdot 10^2$ to $5.3 \cdot 10^2$ counts·sec^{-1}, i.e., compared to the case without grains, only 12.5% of the molecules desorbed and passed in the gas phase.

Figure 4.6(b) shows the signal at 15 m/z (associated with the methyl radical CH_3) and 29 m/z (associated with the formyl radical HCO) detected by the mass spectrometer during the acetaldehyde desorption from olivine grains. These signals, observed at the same desorption temperature of acetaldehyde, are associated with the cracking patterns of acetaldehyde in the head of the mass spectrometer. From the acetaldehyde mass spectra available on NIST, the most intense signal occurs at 29 m/z followed by the 44 m/z with signal intensity of 80%, and then by that at 15 m/z with 40%. However, in the presence of grains in addition to a notable decrease in the 44 m/z signal intensity (only $\sim$500 counts·sec^{-1} compared to $4.24 \cdot 10^3$ counts·sec^{-1} without grains), an increase in the 29 and 15 m/z signal intensity was observed (10^4 counts·sec^{-1} and $8 \cdot 10^3$ counts·sec^{-1}, respectively). In particular, the 15 m/z signal was nearly as intense as the 29 m/z signal, much higher than the expected amount of the cracking patterns. This may suggest that the presence of olivine catalyzes the carbon-carbon bond breaking in the acetaldehyde molecule. It was found in fact that the carbon-carbon bond of adsorbed acetaldehyde breaks easily, occurring at low potential (e.g., Lai et al. 2008). Both signals showed a double desorption: a first peak at 103.0 K (the same temperature of sublimation of acetaldehyde) followed by a shoulder showing its maximum intensity increase at 170.2 K.

Figure 4.7 presents the results obtained when acetaldehyde was deposited in the UHV chamber mixed with water. CH_3COH was first deposited with

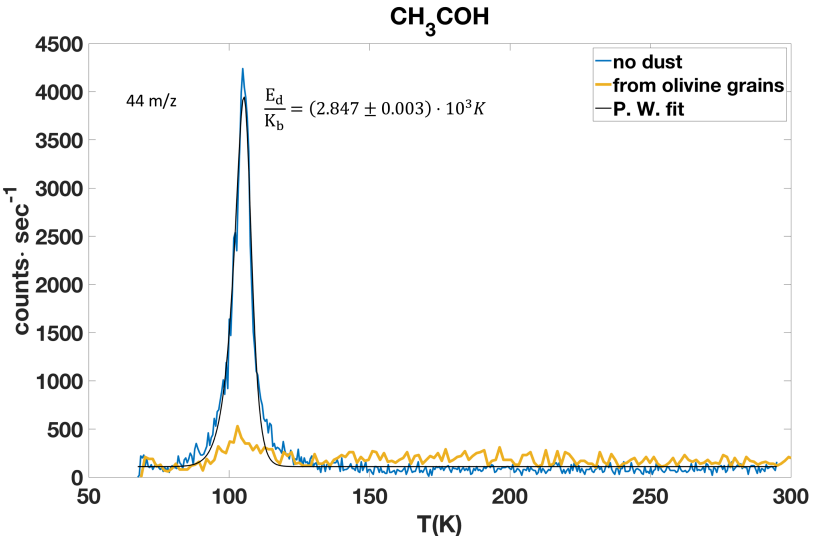

(a)

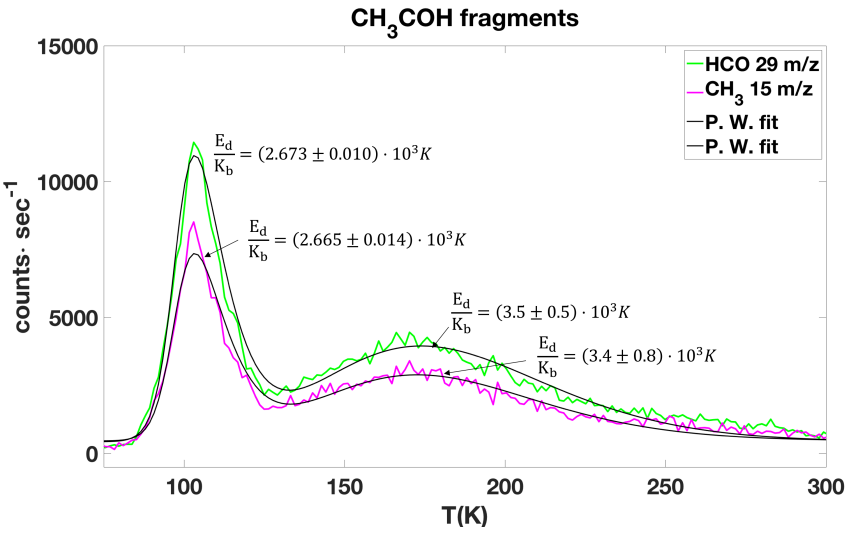

(b)

Figure 4.6: **(a)** The figure shows two experiments. In both experiments, we deposited in the **UHV** chamber the same amount of acetaldehyde CH_3COH (partial pressure of CH_3COH in the pre-chamber 0.68 mbar). **Blue curve**: CH_3COH desorption directly from the cold finger of cryostat cooled to 17 K. **Yellow curve**: CH_3COH desorption from olivine dust. In presence of olivine, acetaldehyde dissociates almost completely into its two components: HCO and CH_3, shown in panel (b). **Black line**: the acetaldehyde TPD curve was fitted through the Polanyi - Wigner equation. **Figure (b)** shows the signal detected at 29 m/z, molecular weight of HCO (green curve), and the signal detected at 15 m/z, molecular weight of CH_3 (purple curve), while acetaldehyde desorbed from olivine dust. These TPD curves in presence of grains show a first desorption peak followed by a shoulder, fitted through the Polanyi - Wigner equation (**Black lines**).

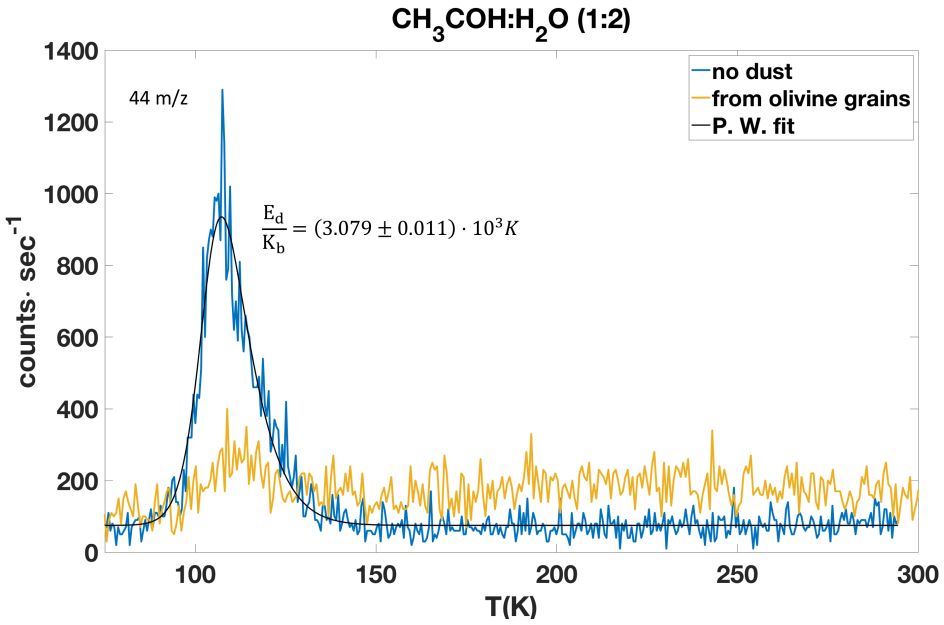

Figure 4.7: The figure shows two experiments. In both experiments, we deposited in the UHV chamber an ice mixture CH_3COH:H_2O (1:2). **Blue curve**: CH_3COH desorption directly from the cold finger of cryostat cooled to 17 K. **Yellow curve**: CH_3COH desorption from olivine dust. In presence of olivine, acetaldehyde dissociates almost completely. **Black line**: the acetaldehyde TPD curve was fitted through the Polanyi - Wigner equation.

water in the pre-chamber and we realized a mixture 1:2 in favor of water through the partial pressures. Then, the mixture was deposited in the UHV chamber first directly on the cold finger of the cryostat (blue curve) and then on olivine dust (yellow curve). Although acetaldehyde was in a mixture with water, its TPD curves showed similar results to those found when the molecule was deposited alone (Fig. 4.6). The blue curve (thermal desorption without grains) showed us that the CH_3COH molecules started to desorb at ∼90 K reaching the maximum desorption peak at 107.5 K and at higher temperature the signal decreased and returned to the initial value already at 130 K. When we deposited the same mixture on olivine dust (yellow curve), the 44 m/z intensity signal was significantly reduced and at the same temperature found without grains, we observed a slight increase in the intensity signal.

Through the experiments shown above, we found that acetaldehyde and

its radicals desorbed around 100 K (∼104 K when acetaldehyde was deposited alone Fig. 4.6, ∼107 K mixed with water Fig. 4.7). In the acetonitrile case, the desorption peak was found at higher temperatures (∼120 K) both when it was deposited alone or mixed with water (Figures 4.3 and 4.4). This difference in the desorption temperature between acetaldehyde and acetonitrile was also found when we deposited the two molecules together. Figure 4.8 presents the desorption of the ice mixture CH_3CN:CH_3COH (1:6) from the cold finger of the cryostat (Fig. 4.8(a)) and from the micrometric grains of olivine dust (Fig. 4.8(b)), respectively. In Fig. 4.8(a), we noted the acetaldehyde desorption peak, the signal at 44 m/z, at 111.2 K. Above the acetaldehyde curve at the same temperature of sublimation, we found the TPD curves of its fragments: the methyl radical CH_3 (signal at 15 m/z) and formyl radical HCO (29 m/z). From the figure, we observed that the intensity of the radicals signal was an order of magnitude greater than that of acetaldehyde. At a higher temperature (130.7 K), we recognized the peak of acetonitrile (signal at 41 m/z). In correspondence with the desorption profile of acetonitrile, the signal at 44 m/z showed a new peak. The peak of the 44 m/z signal at 130 K is linked to acetonitrile. This is supported by the evidence that during the experiments with only acetonitrile and water, we observed a desorption peak corresponding to the 44 m/z signal at the same temperature of sublimation of acetonitrile and of greater intensity than the acetonitrile curve itself (Figs. 4.4 and 4.5). In Figure 4.8(a), the peaks at 130 K, therefore, describe the acetonitrile desorption (partial pressure of 0.3 mbar). The leftmost part of the graph instead describes the acetaldehyde desorption (partial pressure 1.8 mbar, six time higher than the acetonitrile amount). We also carried out this experiment in the presence of the olivine substrate (Fig. 4.8(b)). In this case, all the TPD curves showed a shoulder when the temperature reached and exceeded the temperature of ∼200 K. In the presence of the grains, acetaldehyde molecules did not dissociate in favor of their radicals as in the experiments shown above. It must be considered that the amount of acetaldehyde deposited in this experiment was 6 times that of the acetonitrile (partial pressure of acetaldehyde 1.8 mbar), i.e., the amount of acetaldehyde deposited was greater than that deposited in the previous experiments.

Figure 4.9 displays the TPD of the ice mixture CH_3CN:CH_3COH:H_2O (1:1:3). Figure 4.9(a) shows the TPD curve of the ice mixture deposited directly on the cold finger of the cryostat. The desorption temperature at 108.7 K is associated with the acetaldehyde radicals formyl at 29 m/z (yellow curve) and methyl 15 m/z (orange curve). However, at this temperature, we did not observe the acetaldehyde peak at 44 m/z (light blue curve). This

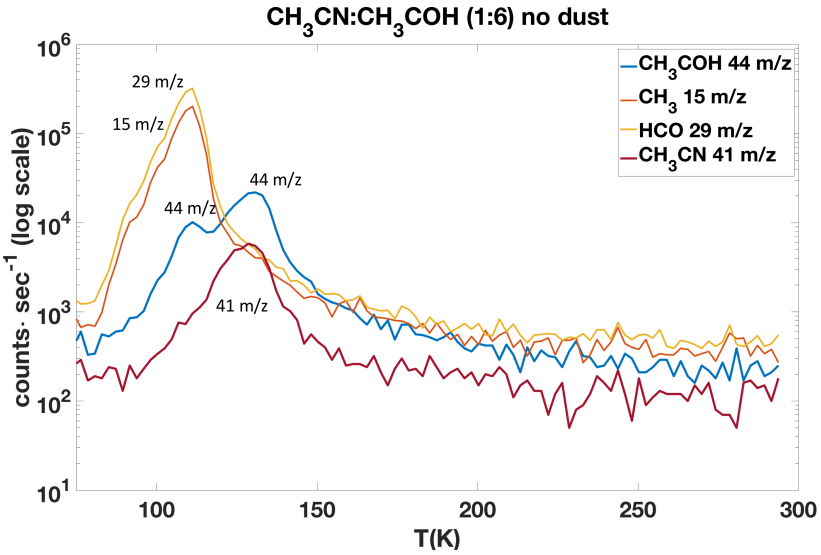

(a)

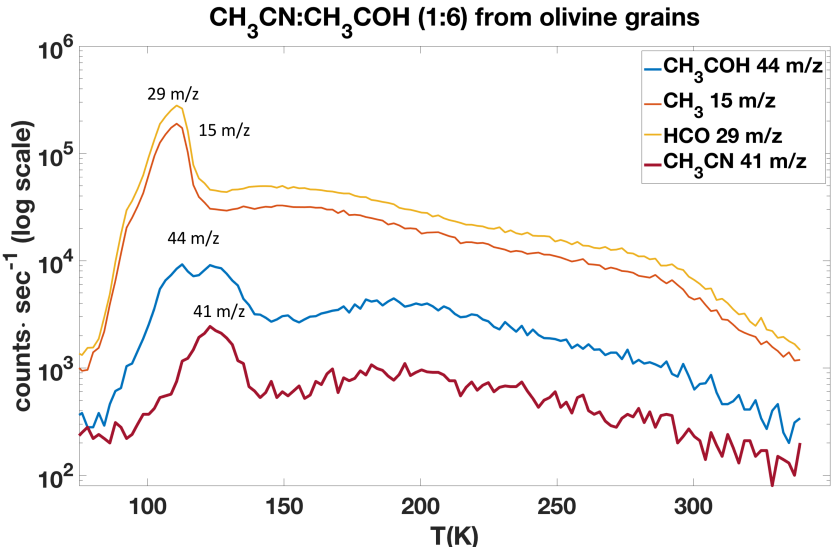

(b)

Figure 4.8: The figures show two experiments. In both experiments, we deposited in the UHV chamber an ice mixture CH_3CN:CH_3COH (1:6). **Panel (a)**: ice mixture desorption directly from the cold finger of cryostat cooled to 17 K. **Panel (b)**: ice mixture desorption from olivine dust.

is due to acetaldehyde dissociation by the mass spectrometer in favor of its radicals. The experiments described above shown that acetonitrile desorbs at a higher temperature than acetaldehyde. Even in this case, we found a CH_3CN peak (41 m/z) (red curve) at a higher temperature, that is, 120.0 K. At this temperature, a peak at 44 m/z (light blue curve) is observed. H_2O (the highest blue curve) desorbed at 135.2 K, a higher temperature than the other two molecules of the mixture. Figure 4.9(b) shows the TPD of the same mixture when deposited on olivine grains. What is noticed is that all the TPD curves showed a second peak at ∼200 K.

In Figure 4.10, the desorption of the signal at 44 m/z from the cold finger (blue curve) and from olivine dust (yellow curve) is compared. The blue curve shows that the desorption started at ∼100 K reaching the maximum at 121.9 K (the signal intensity increased to $6.49 \cdot 10^3$ counts·sec^{-1}). At a temperature higher than 121 K, the signal decreased and returned to the initial value at 150 K. The yellow curve shows that when we deposited the same mixture on olivine dust, 50% of the counts are measured at the same temperature previously found, ∼123 K, where the intensity of the yellow curve reached the value of $3.38 \cdot 10^3$ counts·sec^{-1}, and about 30% of the counts are observed at ∼200 K. In the same way, the blue curve of Figure 4.11 (CH_3CN desorption from the cold finger of the cryostat) showed only one desorption peak at 120.0 K: the signal started to desorb at 100 K, reached its maximum signal intensity at 120.0 K and then started immediately to decrease and returned to its initial value already at 150 K. The yellow curve instead (CH_3CN desorption from olivine dust) shows up that 60% of the acetonitrile molecules desorbed at the same temperature found in the absence of grains and the others molecules gradually desorbed as the temperature increased. Thus, during both 44 m/z and 41 m/z desorption from olivine experiments, we found a first desorption peak occurring at the same temperature than that found without grains but lower in intensity followed by a second desorption at higher temperature and hence, at higher desorption energy.

Table 4.1 summarizes the best fit values obtained through the Polanyi - Wigner equation for the desorption temperatures and energies both from cold finger and from olivine grains of pure and mixed molecules.

4.4 Discussion and astrophysical implication

4.4.1 Interaction with water

A first result from our experiments concerns the desorption temperatures and energies found for CH_3CN and CH_3COH. Figures 4.3, 4.4, 4.6(a), and 4.7

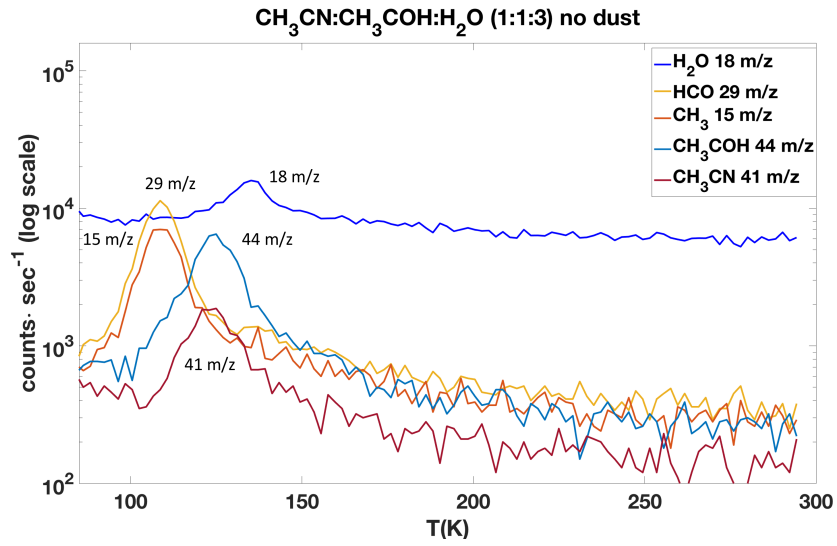

(a)

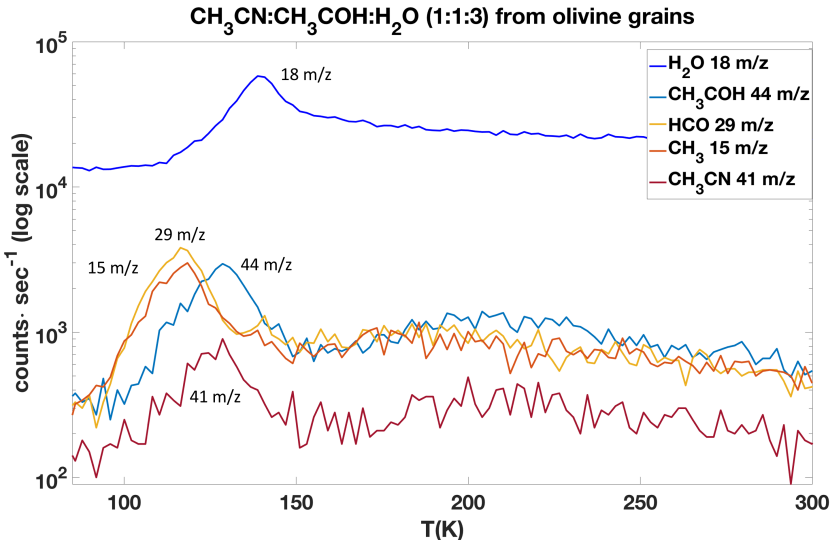

(b)

Figure 4.9: The figure shows two experiments. In both experiments, we deposited in the UHV chamber an ice mixture CH_3CN:CH_3COH:H_2O (1:1:3). **Panel (a)**: ice mixture desorption directly from the cold finger of cryostat cooled to 17 K. **Panel (b)**: ice mixture desorption from olivine dust.

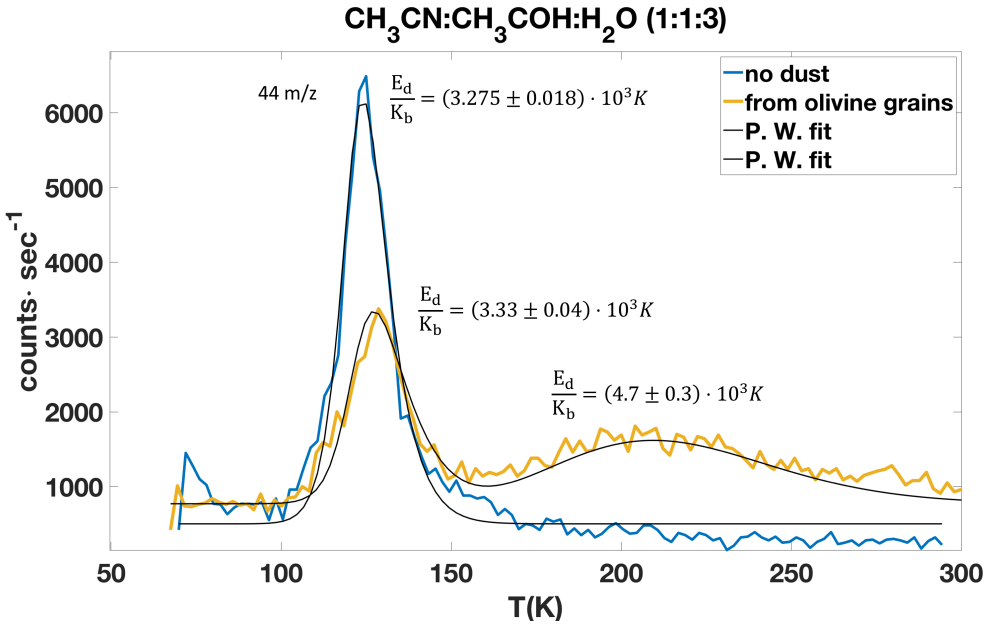

Figure 4.10: The figure shows two experiments. In both experiments, we deposited in the UHV chamber an ice mixture CH_3CN:CH_3COH:H_2O (1:1:3). **Blue curve**: 44 m/z desorption directly from the cold finger of cryostat cooled to 17 K. **Yellow curve**: 44 m/z desorption from olivine dust. In presence of olivine, we found a first desorption peak at the same temperature found in absence of grains but lower in intensity and then the curve shows a second wider desorption peak. **Black lines**: the TPD curves were fitted through the Polanyi - Wigner equation.

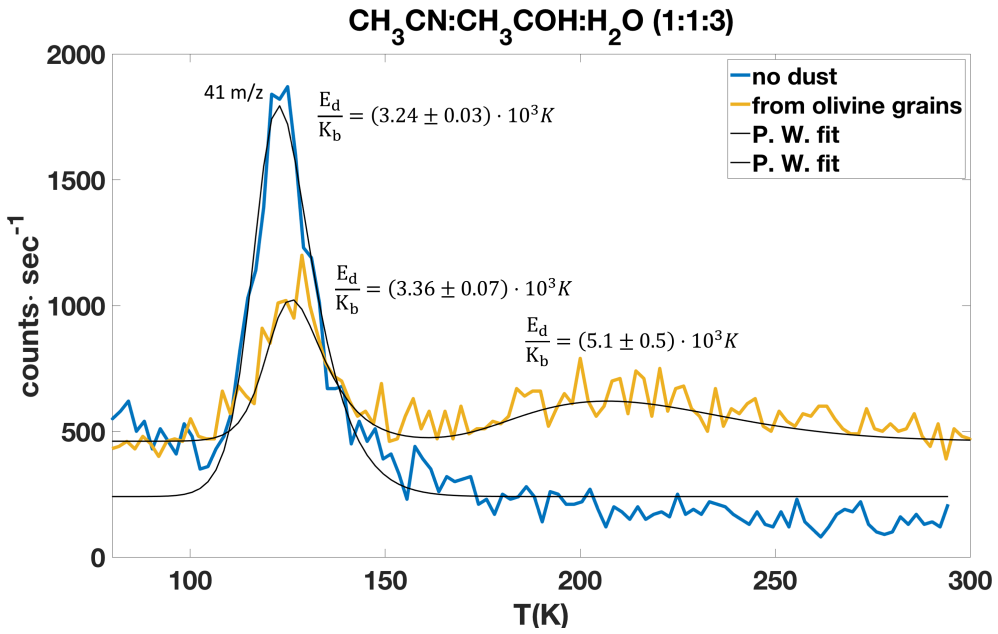

Figure 4.11: The figure shows two experiments. In both experiments, we deposited in the UHV chamber an ice mixture CH_3CN:CH_3COH:H_2O (1:1:3). **Blue curve**: 41 m/z desorption directly from the cold finger of cryostat cooled to 17 K. **Yellow curve**: 41 m/z desorption from olivine dust. **Black lines**: the TPD curves were fitted through the Polanyi - Wigner equation.

show the desorption from the cold finger (blue curves) and from olivine grains (yellow curves) both when the molecules of acetonitrile and acetaldehyde were deposited pure and mixed with water. Table 4.1 reports the values obtained by the Polanyi - Wigner equation for the desorption temperatures T_d and energies E_d/K_b. As reported, we obtained similar results for T_d and E_d/K_b of acetonitrile both when it was deposited alone (Fig. 4.3) and in mixture with water (Fig. 4.4), see Table 4.1. Although, as we will see later, the shape of the TPD changes in the presence of the olivine substrate (yellow curve compared to the blue one), the position of the first desorption peak does not change. The T_d and E_d/K_b values for the first peak are comparable even in the presence of grains, both in the experiments without the presence of water in the deposit phase and in the experiments with the water mixture. A similar comparison can be made for acetaldehyde, and once again, the results of T_d and E_d/K_b are comparable both in the experiment with the pure molecule and in a mixture with water (Figs. 4.6(a), 4.7, and Table 4.1). Moreover, we found that acetaldehyde and its radicals CH_3 and HCO desorb at about 100 K, while acetonitrile desorbs at slightly higher temperatures $T_d = 120$ K. The difference in desorption temperature between acetaldehyde and acetonitrile was also found when we deposited the two molecules together (Fig. 4.8 (a) and (b)), and in mixture with water (Fig. 4.9 (a) and (b)).

Many experimental works studied the release in the gaseous phase of gas mixtures and molecules trapped in amorphous water ice showing as the release of the most volatile component of the ice mixture occurs for discrete temperature ranges associated with changes in ice (e.g., Bar-Nun et al. 1988, Sandford et al. 1988 and Hudson et al. 1991). Although the ability of water to trap molecules with lower sublimation temperatures is thought to be one of the responsible processes for the release in the gaseous phase of the most volatile species contributing to the gas phase composition of the interstellar medium (e.g., Ángel Satorre Aznar et al. 2010, Hassel 2004), in our experiments, water does not appear to play such a role in the molecules' desorption. The molecules and their radicals desorb at a different T_d characteristic of each molecular species regardless of the presence of water in the deposit. However, we must take into account that in space the amount of water compared to other molecules is much greater than the 1:2 ratio used in this work. Through spectroscopic surveys, CH_3CN was detected in more than 10 comets and its molecular abundance relative to water is 0.01% (Mumma et al., 2011). In comet 67P/Churyumov-Gerasimenko, the deduced bulk abundances of the major volatile species, obtained with the ROSINA instrument on board the Rosetta orbiter, show CH_3CN/H_2O=0.0059% (so a ratio $\sim$ 1:16000) and CH_3COH/H_2O=0.047% (1:2000) (Rubin et al., 2019). In comet Lovejoy, the amount of acetaldehyde is 0.1% compared to water

(Val-Borro et al., 2018), which is a 1:1000 ratio. In the laboratory, we could not use these ratios due to experimental needs. We were forced to maintain the total pressure in the pre-chamber below 2 mbar, to avoid the risk of compromising the mass spectrometer detector. At this pressure, for example, the amount of acetaldehyde needed to stay in a 1:1000 ratio is 10^{-3} mbar, a quantity too low to obtain a clear TPD curve. The fact that in interstellar ices the amount of H_2O compared to other species is much greater than the ratio used in the experiments may influence the role played by water in the desorption of other species. Another experimental limit is represented by grains. In the ISM, the grains are micrometric fluffy amorphous silicate grains while in our measurements, we worked with a 100 μm dust layer thick made of crystalline olivine grains with sizes smaller than 5 μm. This aspect can change the conditions of interactions between water and the other molecules.

4.4.2 The role of grains

The results obtained in this work show how the interactions between the molecules and the surface of the grains can drive the presence of iCOMs in the gaseous phase in environments where thermal heating has a dominant role. Comparing the TPD curves of pure water, acetonitrile, and acetaldehyde from olivine grains (yellow curves), we notice that they show a similar shape: a first sharp desorption peak followed by a second wider peak at a higher temperature. The first peak is associated with the first-order desorption of each molecule interacting with the surface atoms of the mineral assemblage.

However, the presence of two TPD peaks suggests that two different processes take place when molecules desorb from dust grains. In fact, all the TPD measurements from the smooth nickel-plated cold finger do not show the second peak. This means that the second peak is related to the presence of olivine grains. In the next future, we should thoroughly investigate the physicochemical processes that could cause this change in TPD curves. In our experiment, we deposited the molecular species on a layer about 100 μm thick made of olivine grains smaller than 5 μm in size. Molecules during the vacuum deposition process diffuse through the dust layer occupying all the available active adsorption sites on olivine grains in a random process. During the TPD process, the adsorbate, once thermally excited with kinetic energies approaching the desorption barrier, will be free to move on the surface until it thermalizes again due to the action of dissipation forces. At temperatures corresponding to the desorption energy or higher, the molecules begin to leave the adsorption sites and desorb. The molecules placed on the surface exposed to vacuum desorb producing the first TPD peak observed at a lower

temperature. This process is described by the Polanyi-Wigner equation. On the other hand, molecules adsorbed on the surfaces of grains placed deeper into the layer, once desorbed, will collide with the next grain surface by thermalizing again. Multiple hoping will be made before molecules are released to vacuum: molecules have to travel a longer path within the dust layer due to multiple desorption/adsorption processes on olivine grain surfaces thus, they are released to the gas phase with a delay. Hence, those diffusing molecules will yield the second wider desorption peak at a higher temperature.

Such diffusion phenomenon may become important in protoplanetary disks, where the submicron interstellar grains present in the parent molecular cloud start to accrete into hundreds of microns fluffy dust (e.g., Testi et al. 2014). Our experiments show that in protoplanetary regions with T $\geq$100 K, where we expect to no longer have acetonitrile and acetaldehyde in the solid phase because they are already desorbed, a fraction of these molecules can instead survive on fluffy grains and can be desorbed at temperatures of about 200 K. The ratio between the intensity of the two desorption peaks depends on the thickness of the dust layer and can provide hints on the fraction of molecules released at different temperatures in, e.g., protoplanetary disks. We observed a ratio between the peaks of about 0.4, obtained by dividing the intensity of the second peak (maximum number in counts·sec^{-1}) by the first most intense peak for each TPD curve of a given m/z. Specifically, this ratio is 0.38 for the acetonitrile (Fig.4.3), and 0.36 for the radicals HCO and CH_3 (Fig.4.6 (b)). This means that porous grains of about 100 μm size, which are the result of coagulation of micrometer size grains, could retain 40% of the molecules at temperatures of about 200 K in contrast with the typical assumption that all molecules are desorbed at temperatures higher than 100 K. Hence, the diffusion by large porous grains is a valuable process which may enable the delivery of molecules to regions at high temperatures.

From astronomical observations, we know that protoplanetary disks are dynamic objects. The mass is transported continuously and accreted by the central star over a period of millions of years. It is essential to understand the effects of this evolution on the primitive materials it contains. The distribution of water and water-carried species in the disk undergoes condensation, growth, transport, and vaporization (e.g., Ciesla et al. 2006). In addition to these processes, our TPD experiments show that volatiles ices rich in oxygen, nitrogen, and carbon can survive in the innermost part of the disk inside the snowlines of O-, N-, and S-bearing molecules. The diffusion is therefore a process enabling the delivery of water to Earth-like planets which form close to their star, ensuring the permanence of volatiles in the innermost part of the disk and shifting inward the position of the snowlines.

Another interesting aspect that was observed during the desorption from

olivine grains is that the intensity of the signals of the two acetaldehyde radicals CH_3 and HCO increase compared to the cold finger desorption (Fig. 4.6 (a) and (b)) and compared to the amounts expected for cracking patterns in the mass spectrometer. Olivine could therefore accelerate the carbon-carbon bond breaking of acetaldehyde in favor of HCO and CH_3. If confirmed, this behavior may have implications in the astrophysical context where episodic warm-ups interspersed with a colder period can occur (for example a Fu Ori system between two different outbursts). In this condition, it could be possible that acetaldehyde is first desorbed from an icy grain, then adsorbed again in the colder region, and finally definitively desorbed to the gas phase (new FU Ori outburst). From our experiment, we foresee that only a small fraction of acetaldehyde will desorb from the grains since it will be almost completely dissociated into HCO and CH_3 through multiple desorption-adsorption processes.

4.4.3 Comparison with the observed abundance ratios

CH_3COH and CH_3CN are detected at all stages of formation of a Sun-like star. It is interesting to compare the observed abundance ratios in the different evolutionary stages with our laboratory results. From our experiments, it is not immediate to find an abundance ratio between CH_3COH and CH_3CN, because we found that acetonitrile itself provides a contribution also to 44 m/z, the same molecular weight of acetaldehyde. If we look at Figure 4.9 (b), we see that at 108.7 K only the acetaldehyde radicals are present, while at 120.0 K (T_d of acetonitrile) acetonitrile provides a signal to 44 m/z . From the ratio between the abundance of the 44 m/z signal at 120.0 K and the radical signals at 108.7 K, we can infer an abundance ratio CH_3COH/CH_3CN $\sim$1; indeed, we did not observe segregation of the molecules during the desorption process and the ratios present in the solid phase are kept in the gas phase. Therefore, in the case of thermal desorption, these laboratory studies tell us that the observed ratios between the molecules in the gas phase reflect the molecular composition of the grain surface.

From the observations, we know that in the protostellar shock L1157-B1 along the outflow driven by the low-mass Class 0 protostar L1157-mm, the CH_3COH/CH_3CN abundance ratio varies depending on the region of the shock: CH_3COH/CH_3CN is $\sim$1 in the region where previous observations indicate that the chemistry is dominated by the release of molecules from grains, instead, the abundance ratio is $\sim$ 0.1 in the region where gas-phase chemistry is likely to dominate (Codella et al. 2009; Codella et al. 2015; Codella et al. 2017, and Podio et al. 2017). In hot-corinos around Class 0 protostars ($\sim 10^4$ yr), the CH_3COH/CH_3CN abundance ratio ranges

from ∼0.5 to 5 (e.g., Belloche et al. 2020), while the only available estimates for the disk around the young outbursting star V883 Ori indicate a CH_3COH/CH_3CN abundance ratio of ∼25 (Lee et al., 2019). Similarly to a hot corino, the molecules covering the icy grains of the disk are thermally desorbed following the outburst of the star. However, acetaldehyde is 25 times more abundant than acetonitrile, a much higher ratio than that found in protostellar objects, both in hot corinos where thermal desorption occurs and in the protostellar shocks where desorption is not thermal. This suggests that the molecular composition of the ices inherited by the early protostellar stages, once incorporated into the disk, may undergo a chemical reprocessing.

4.4.4 Highlighted results

In this chapter, we investigated the desorption of ice mixtures from silicate olivine, simulating a process that realistically takes place in star-forming regions. We can summarize the found results in two fundamental points:

- The TPD experiments show how the interactions between the molecules and the surface of the grains can drive the presence of molecules in the gaseous phase. In the presence of grains, the TPD curves show a first sharp desorption peak at about 100 K and 120 K for acetaldehyde and acetonitrile, respectively, followed by a second wider peak at higher temperature and with about 40% intensity with respect to the first peak. So, 40% of the molecules are retained by fluffy grains of the order of 100 μm up to temperatures of ∼200 K. This may be important in protoplanetary disks where the submicrometric interstellar grains begin to agglomerate into fluffy grains of hundreds of microns. The diffusion of molecules on the silicate surface is a valuable process enabling the permanence of the ices in the inner part of the disk. This implies that O-rich and N-rich volatiles ice can survive up to ∼200 K, broadening the snowlines of O- and N-bearing molecules, such as CH_3CN and CH_3COH. The presence of olivine can therefore determine the approach of the snowlines to the star and the presence of water and volatile species in Earth-like planets forming close to their star.

- During the desorption process, we did not observe the segregation of the molecules and so, the abundance ratios present in the solid phase are kept in the gas phase. This result implies that the observed abundance ratios in the gas phase reflect the molecular composition of the grain surface, if the observed molecules in the gas phase are the result of the thermal desorption process as in the case of the hot corinos or the disk around the young outbursting star V883 Ori. The fact

that the CH_3COH/CH_3CN ratio in the disk is $\sim$25 while in the hot corinos around Class 0 protostars ranges from $\sim$0.5 to 5 suggests that the molecular composition of ices inherited from the early protostellar stages is reprocessed and undergoes formation and destruction processes.

Chapter 5

Photoprocessing of acetaldehyde and acetonitrile ices mixed with olivine

In the previous chapter, through TPD experiments of ice mixtures of acetaldehyde and acetonitrile from micrometric grains of olivine, we studied how solid-phase interactions between molecules and grain surfaces can influence the desorption process and, hence, the presence and abundance of molecular species in the gas phase. We found that the presence of grains modifies the gas phase release of the molecules. Only a fraction of acetaldehyde and acetonitrile desorbs respectively at about 100 K and 120 K, while 40% of the molecules are retained by physisorption forces of grain surfaces up to temperatures of 200 K. Thus, the grains can allow the permanence of the volatile molecules in the inner part of the disk. The presence of the dust can therefore determine the approaching of the snow lines to the star and therefore drive the presence of water and volatile species in the formation regions of Earth-like planets.

In the introduction, we underlined how photoprocessing is one of the mechanisms responsible for chemical evolution in space promoting photochemical reactions particularly on surfaces of dust grains, which can act as photocatalysts. Moreover, relatively high abundances of iCOMs such as acetonitrile and acetaldehyde are observed in photon-dominated regions (PDRs) and in the UV-exposed atmospheres of planet-forming disks (Le Gal et al., 2019).

In this chapter, acetonitrile and acetaldehyde mixtures were subjected to in situ UV irradiation to study their photolysis or the formation of more complex molecules. Monolayers of pure acetaldehyde, pure acetonitrile, and mixture CH_3CN:CH_3COH (1:6) were deposited on micrometric grains of olivine

at 17 K in the UHV chamber and subjected to UV irradiation in situ. We reported both the TPD curves of the irradiated molecules and photoproducts and the mass spectra from 1 to 300 m/z.

In section 1, we will describe the results of thermally desorbed acetaldehyde, acetonitrile, and ice mixtures after UV irradiation. The results obtained will be discussed in section 2.

The experiments and results shown in this chapter were recently submitted to the Astrophysical Journal, in the paper "Photo-processing and thermal desorption of acetaldehyde and acetonitrile ices mixed with olivine".

5.1 Results

5.1.1 UV irradiation of acetonitrile and acetaldehyde

Acetaldehyde CH_3COH Figure 5.1 shows the acetaldehyde thermal desorption from the cold finger of the cryostat in the non-irradiated case (blue line with fit overlapped) and in the case in which the sample was subjected to 8 hours of UV irradiation (purple line). The figure displays that, although the same amount of acetaldehyde was deposited on the cold finger of the cryostat (partial pressure in the pre-chamber of 0.68 mbar), the intensity of the peak in counts·sec^{-1} was 60% lower in the irradiated case. The counts decreased from the value of 4000 counts·sec^{-1} in the non-irradiated case to 2500 in the presence of radiation. However, there was not only a reduction in the height of the peak but a change in the shape of the curve. In the irradiated case, the width half-height of the curve was wider. This broadening was due to the presence of two peaks: a first intense peak of 2500 counts·sec^{-1} at the same temperature as the non-irradiated case (104 K) and to a second intense peak of 2000 counts·sec^{-1}.

After UV irradiation, the 44 m/z (molecular weight of acetaldehyde) signal intensity in counts·sec^{-1} was reduced, instead, the intensity of the acetaldehyde fragments increased, i.e., the signals at 15 m/z (CH_3) and 29 m/z (HCO). Figure 5.2 shows through a histogram graph the signal at 15 m/z (figure a) and 29 m/z (figure b) detected by the mass spectrometer during the acetaldehyde desorption (44 m/z) in the non-irradiated case and after UV irradiation. The x-axis reports integers, which are the number of cycles during which the thermal desorption of the molecules from the cold finger took place as the temperature increased. The figure shows that both in the non-irradiated case (fluorescent histograms) and irradiated case (dark colors), the molecules desorbed in the same temperature range between 92 and 138 K, values in agreement with the TPD shown in the previous chapter,

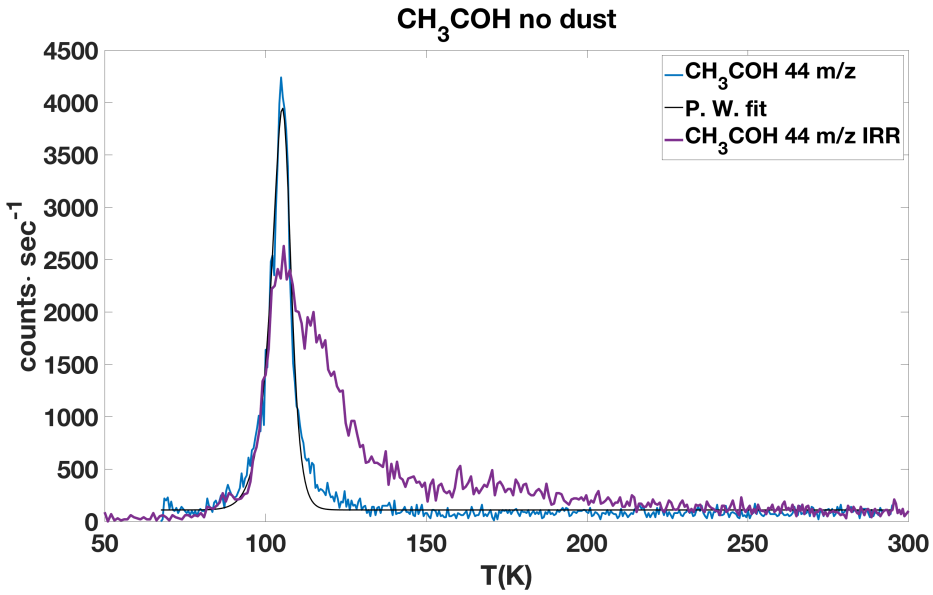

Figure 5.1: TPD curves of CH_3COH (44 m/z) before (blue line) and after (purple line) 8 hours of UV irradiation.

which showed a desorption peak for acetaldehyde and its fragments without the presence of grains at 104.9 K (see, Table 4.1). Therefore, the desorption temperatures did not vary as a result of UV irradiation, and the fragments desorbed at the same temperature as the parent molecule.

Since the fragments desorbed at the same temperature as the acetaldehyde even in the irradiated case, they are associated with the cracking patterns of acetaldehyde dissociation due to the mass spectrometer. As described in the previous chapter, from the acetaldehyde mass spectra available on NIST, the most intense signal occurs at 29 m/z followed by the 44 m/z with a signal intensity of 80%, and then by that at 15 m/z with 40%. According to NIST data, in the non-irradiated case, the signal at 29 m/z was the most intense ($12{\cdot}10^4$ counts·sec^{-1}, green fluorescent histogram corresponding to cycle 5 in Figure 5.2 b), while the 15 m/z signal was lower, $5{\cdot}10^4$ counts·sec^{-1} (fuchsia histogram corresponding to cycle 5 in Figure 5.2 a). After UV irradiation, the intensity of the signal at 29 m/z was comparable to the non-irradiated case (dark green histogram corresponding to cycle 5 in Figure 5.2 b), while the intensity of the 15 m/z signal increased passing from $5{\cdot}10^4$ counts·sec^{-1} to $8{\cdot}10^4$ counts·sec^{-1} (dark purple histogram corresponding to cycle 5 in Figure 5.2 a). In the non-irradiated case, the 29 m/z signal was 2.4 times greater than at 15 m/z while in the irradiated case,

the difference between the two signals decreased and that at 29 m/z was 1.5 times greater than that at 15 m/z. So, in the presence of UV radiation, in addition to a widening of the 44 m/z TPD curve and a decrease in its signal intensity (Fig. 5.1), an increase in the 15 m/z signal intensity was observed. In particular, the 15m/z signal was nearly as intense as the 29 m/z signal, much higher than the expected amount of the cracking patterns.

Figure 5.3 reports the complete acetaldehyde mass spectrum from 1 to 300 m/z in the non-irradiated case (blue histograms) and in the irradiated case (red histograms).

Acetonitrile CH_3CN Figure 5.4 shows the thermal desorption of acetonitrile and its fragments before UV irradiation (solid lines) and after 8 hours of UV irradiation (dashed lines). In the irradiated case, the T_{des} were shifted towards higher temperatures. The figure shows that without UV irradiation (continuous lines), acetonitrile (41 m/z) desorbed at 124 K and its signal is 1.5 $\cdot 10^4$ counts$\cdot$sec^{-1} (blue continuous line) and at the same temperature, also the signals at 40 m/z (CH_2CN green line), 27 m/z (HCN yellow line), and 44 m/z (red line) increased. This last signal was the most intense, 3.5$\cdot 10^4$ counts$\cdot$sec^{-1}. In the previous chapter and work Corazzi et al., 2021, we already observed that acetonitrile provides a very intense 44 m/z signal (not justifiable only with CO_2 contamination). We suggested as a possible interpretation that the 44 m/z signal could be associated with the cracking in the mass spectrometer of dimethylamine CH_3-NH-CH_3 (45 m/z), whose presence could be a consequence of acetonitrile hydrogenation (e.g., Nguyen et al. 2019). After UV irradiation, we observed the same signals with intensity comparable to the non-irradiated case, i.e., 44 m/z is the most intense signal (4$\cdot 10^4$ counts$\cdot$sec^{-1} dashed red line), followed by the 41 m/z signal (1$\cdot 10^4$ counts$\cdot$sec^{-1} dashed blue line) and then by the 40 and 27 m/z signal (dashed green and yellow line respectively). However, the desorption temperature was no longer 124 K, but 130 K, i.e., all the TPD curves were shifted to the right by a few kelvins.

Figure 5.5 shows two experiments (blue and red histograms respectively). For each experiment, the figure reports the acetonitrile mass spectrum detected during the thermal desorption of molecules when the temperature was rising between 256 and 292 K. The mass spectrum displays the observed signal between 50 and 300 m/z, i.e., molecular weights higher than acetonitrile (41 m/z) and its fragments. To better visualize the signals detected by the spectrometer, the mass spectrum was divided into 3 ranges: Figure a) shows the range 50-100 m/z, Figure b) shows the range 100-150 m/z, and Figure

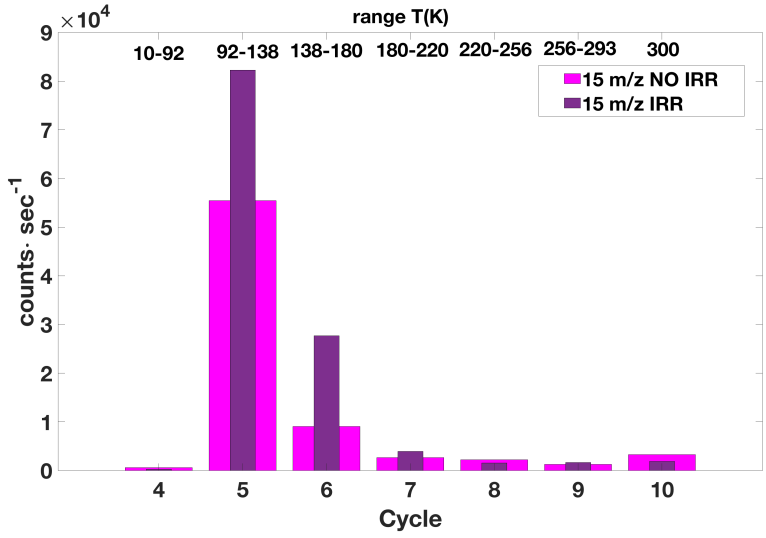

(a)

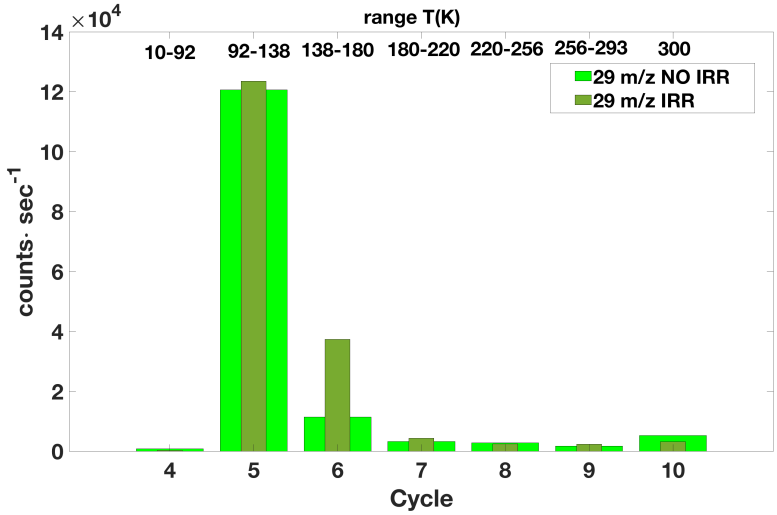

(b)

Figure 5.2: Both the above figure and the below one show two experiments: the thermal desorption of pure acetaldehyde and subjected to UV irradiation. In both experiments (without and in presence of UV radiation), we deposited in the UHV chamber the same amount of acetaldehyde CH_3COH (partial pressure of CH_3COH in the pre-chamber 0.68 mbar). **Figure (a)**: the first figure shows the 15 m/z signal detected by the mass spectrometer during the acetaldehyde thermal desorption. The fuchsia histograms display the 15 m/z thermal desorption in the non-irradiated case, while the dark violet histograms are the case in which acetaldehyde was subjected to irradiation. The x-axis shows the number of cycles during which the thermal desorption of the molecules took place as the temperature increased. The temperature range of each cycle is shown on the x-axis at the top. **Figure (b)**: the second figure shows the 29 m/z signal detected by the mass spectrometer during the acetaldehyde thermal desorption before UV irradiation (fluorescent green histograms) and after UV irradiation (dark green histograms). In both irradiated and non-irradiated cases, the molecules desorb in the same temperature range, i.e., during the 5th cycle (T_{des} between 92 and 138 K).

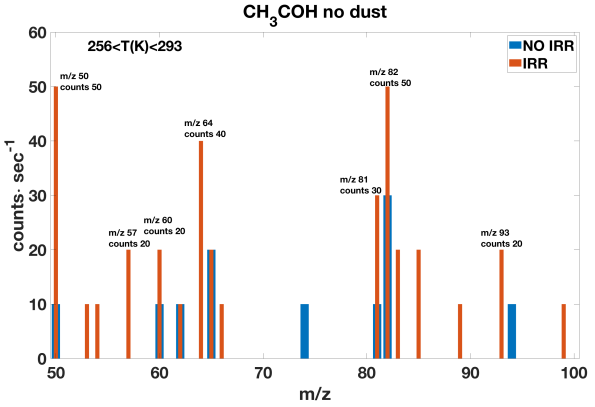

(a)

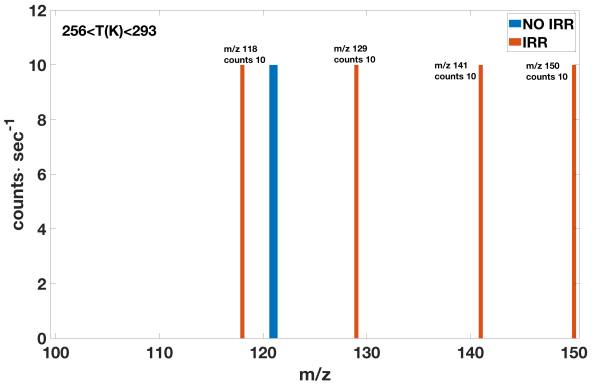

(b)

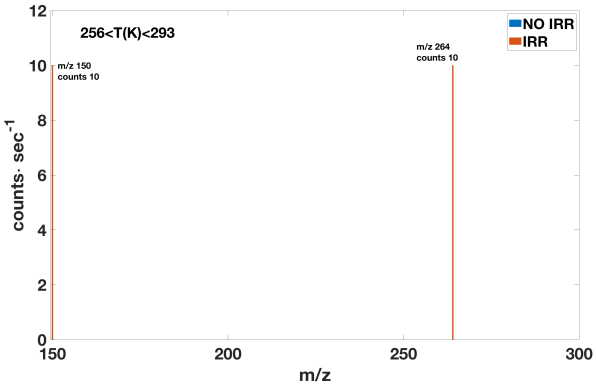

(c)

Figure 5.3: In all Figures, two experiments are reported. For both experiments, the figures show the acetaldehyde mass spectrum between 50 and 100 m/z (Fig. a), 100 and 150 m/z (Fig. b), and between 150 and 300 m/z (Fig. c) during the molecules desorption when the temperature was rising from 256 to 292 K. The blue histograms show the acetaldehyde mass spectrum without the effects of UV irradiation, while the red histograms show how the acetaldehyde mass spectrum changed after 8 hours of UV irradiation.

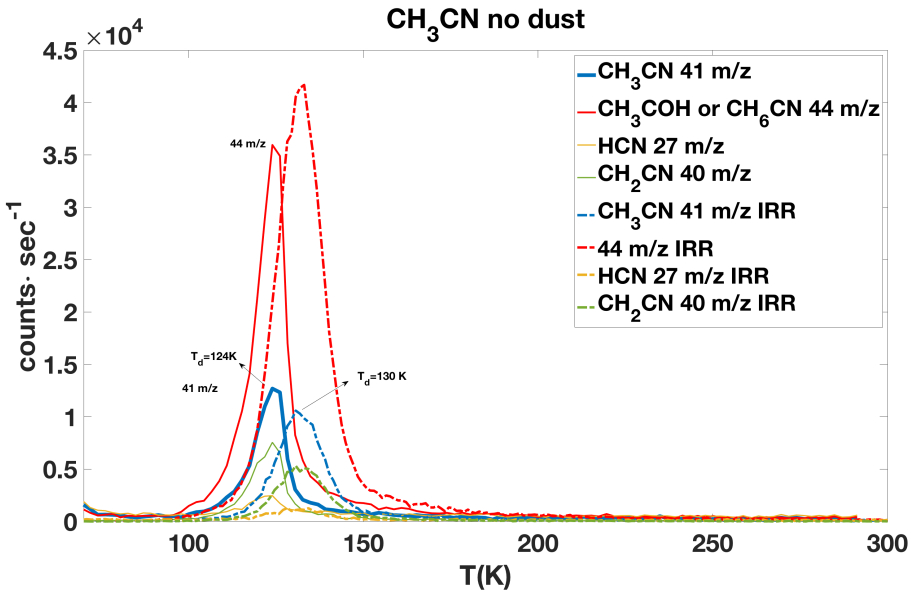

Figure 5.4: TPD curves at 41 m/z (blue curves - CH_3CN), 44 m/z (red curves - a possible interpretations for this 44 m/z signal is that it could be associated with the cracking in the mass spectrometer of the signal at 45 m/z which presence could be due to acetonitrile hydrogenation), 40 m/z (green curves - CH_2CN), and 27 m/z (yellow curves - HCN) before (continuous curves) and after (dashed curves) 8 hours of UV irradiation.

c) shows the higher molecular weights between 150 and 300 m/z. The histograms in blue describe the pure acetonitrile mass spectrum non-irradiated. The histograms in red, on the other hand, describe how the spectrum changed after 8 hours of UV irradiation. In this second experiment, the same amount of acetonitrile was deposited on the bare cold finger in the UHV chamber at 17 K, then it was subjected to 8 hours of UV irradiation in situ at 17 K, and then thermally desorbed.

Figure 5.5 immediately shows greater counts in the irradiated case than the non-irradiated sample. This supports the fact that the irradiation formed new species and we no longer are observing a pure acetonitrile ice thermal desorption. Between 50 and 100 m/z (Fig. a) in the non-irradiated case (blue histograms), only the signals corresponding to 62 m/z (10 counts·sec^{-1}), and 85 m/z (20 counts·sec^{-1}) were observed. In the irradiated case (red histograms), the mass spectrometer revealed signals for almost all m/z including a 70 counts·sec^{-1} signal intensity at 50 m/z, 140 counts·sec^{-1} signal intensity at 65 m/z (C_3N_2H), 30 counts·sec^{-1} signal intensity at 78 m/z ($C_4N_2H_2$), and 20 counts·sec^{-1} signal intensity at 81 m/z ($C_4N_2H_5$). This trend was also observed in the part of the spectrum between 100 and 150 m/z (Fig. b). In the non-irradiated case (blue histograms), only two signals of 10 counts·sec^{-1} intensity corresponding to 110 and 115 m/z were observed. In the irradiated case instead (red histograms), signals were observed at 101, 102, 118, 131, 133, 134, and 138 m/z. Then, irradiating pure acetonitrile ice, signals corresponding to new m/z appeared. This effect appears to be greater with acetonitrile than in the case of acetaldehyde (Fig. 5.3) where the UV radiation role seems to mainly provide the two radicals HCO and CH_3 (Fig. 5.2).

ice mixture CH_3CN:CH_3COH (1:6) Figure 5.6 shows the thermal desorption from the bare cold finger of the cryostat of the mixture CH_3CN:CH_3COH (1:6) in the non-irradiated case (solid lines) and in the case in which the mixture was subjected to 8 hours of UV irradiation (dashed lines). The blue curves in the figure show the TPD curves at 44 m/z, the molecular weight of acetaldehyde. As we have already seen in the previous chapter and work Corazzi et al., 2021, in the case of the acetonitrile - acetaldehyde mixture, the signal at 44 m/z shows two peaks: a first peak at about 100 K (temperature of sublimation found for acetaldehyde, so it is acetaldehyde peak) and a second one at ∼120 K, the same temperature of acetonitrile desorption. This second peak could be due to the cracking in the mass spectrometer of dimethylamine CH_3-NH-CH_3 (45 m/z) due to the acetonitrile hydrogenation. In the same position of the second 44 m/z peak, we found the TPD curves

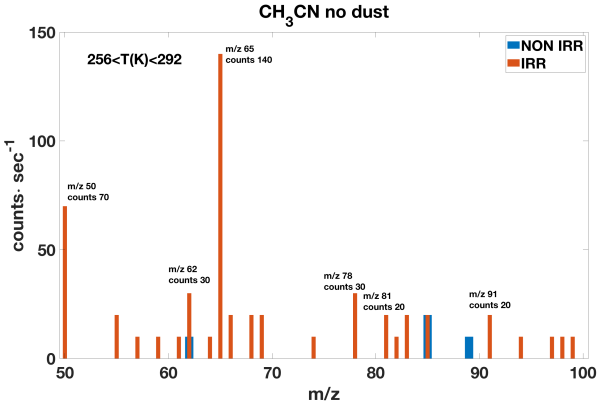

(a)

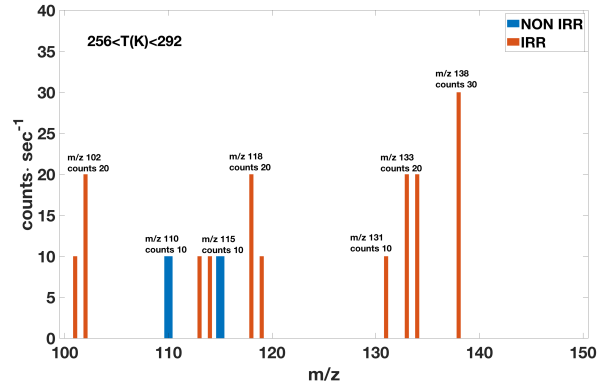

(b)

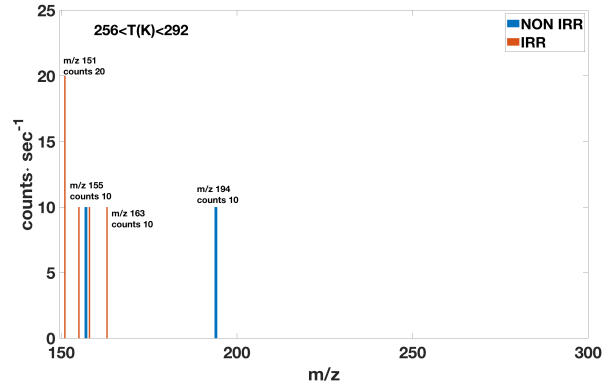

(c)

Figure 5.5: In all Figures, two experiments are reported. For both experiments, the figures show the acetonitrile mass spectrum between 50 and 100 m/z (Fig. a), 100 and 150 m/z (Fig. b), and between 150 and 300 m/z (Fig. c) during the molecules desorption when the temperature was rising from 256 to 292 K. The blue histograms show the acetonitrile mass spectrum without the effects of UV irradiation, while the red histograms show how the acetonitrile mass spectrum changed after 8 hours of UV irradiation.

of acetonitrile (41 m/z - bordeaux curves). While at the same temperature as the first 44 m/z peak (associated with acetaldehyde), we found the signals corresponding to the two acetaldehyde radicals: HCO (29 m/z - yellow curves) and CH_3 (15 m/z - orange curves).

In the case of acetonitrile, we found that after UV irradiation, the desorption peaks were shifted towards higher temperatures (Fig. 5.4), while this shift was not observed in the acetaldehyde case (see Fig. 5.2, where the acetaldehyde radicals desorbed at the same temperature range both before and after UV irradiation). Mainly in the case of acetonitrile, the mass spectrum between 0 and 300 m/z (Fig. 5.5) showed that UV irradiation increased the signals to different m/z (therefore it produced new species).

Figure 5.6 does not show a rightward shift in desorption temperatures after UV irradiation. We can notice, however, that all the dashed curves (TPD curves after UV irradiation) are greater in intensity than the continuous ones, mainly in the case of the HCO and CH_3 radicals. The orange curves of CH_3 (m/z 15) increased from $2{\cdot}10^5$ counts·sec^{-1} before UV irradiation (continuous curve) to $3{\cdot}10^6$ counts·sec^{-1} after irradiation (dashed curve). This increase due to UV radiation is also greater than that found in the case of the pure molecule when the counts after photo processing went from $5{\cdot}10^4$ counts·sec^{-1} to $8{\cdot}10^4$ counts·sec^{-1} (Fig. 5.2 a). In the case of the pure molecule, the HCO counts (29 m/z) remained comparable after irradiation (Fig. 5.2 b). In the case of the mixture, on the other hand, Figure 5.6 evidences an increase in the intensity of the HCO signal (yellow curves) which passed from $3{\cdot}10^5$ counts·sec^{-1} to $4.6{\cdot}10^6$ counts·sec^{-1} after irradiation. After UV irradiation, the intensity of the signals corresponding to 15 and 29 m/z increased, and in particular, the 15 m/z signal intensity is greater than that expected from the cracking patterns of the acetaldehyde in the head of the mass spectrometer and reported by NIST.

Furthermore, Figure 5.6 reveals another aspect. The half-height width of the TPD curves seems to increase after UV irradiation. The shape of the dashed TPD curves (case in which the mixture was photoprocessed) is different and wider from that of the continuous curves. When the ice mixture was deposited on the cold finger and then directly thermally desorbed, the TPD curves showed a desorption peak at a given T_{des}, i.e., as the temperature increased, the molecules began to desorb and the signal reached a peak at the specific desorption temperature. In the irradiated case, the desorption temperature at which the maximum signal was observed did not change, but the curves widened as if the molecules no longer desorbed all at the same T_{des}. The figure could be the result of the convolution of multiple contributions as if the desorption occurred over a larger temperature range. This change in shape and the increase in the half-height width of the TPD curves after

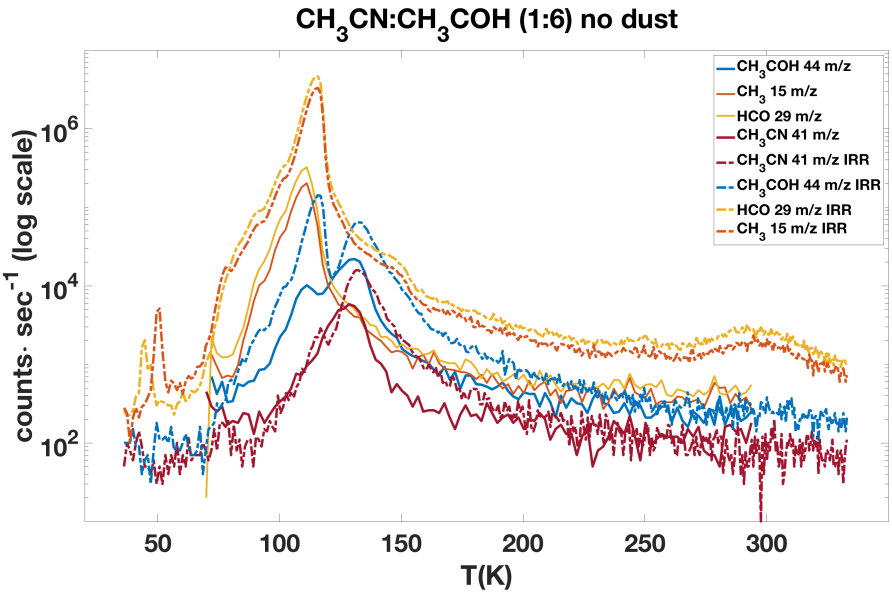

Figure 5.6: TPD curves at 44 m/z (blue curves - we associated the first peak at lower temperature to acetaldehyde CH_3COH, while a possible interpretations for the second peak at the same temperature of acetonitrile could be the cracking in the mass spectrometer of the 45 m/z signal which presence could be due to acetonitrile hydrogenation), 41 m/z (bordeaux curves - CH_3CN), 29 m/z (yellow curves - HCO), and 15 m/z (orange curves -CH_3) before (continuous curves) and after (dashed curves) 8 hours of UV irradiation.

irradiation was also found in the case of pure acetaldehyde (see Fig. 5.1).

Figure 5.7 reports the ice mixture spectrum from 1 to 150 m/z in the non-irradiated case (blue histograms) and the irradiated case (red histograms).

5.1.2 UV irradiation of acetonitrile and acetaldehyde in presence of olivine grains

A second set of experiments deals with UV irradiation of CH_3COH, CH_3CN, and the ice mixture CH_3CN:CH_3COH (1:6) in the presence of olivine grains. The purpose is to investigate if olivine grains could play a catalytic role during photo-processing.

Acetaldehyde CH_3COH Figures 5.8 and 5.9 show the full acetaldehyde mass spectrum up to 300 m/z. The spectral range between 0 and 50 m/z

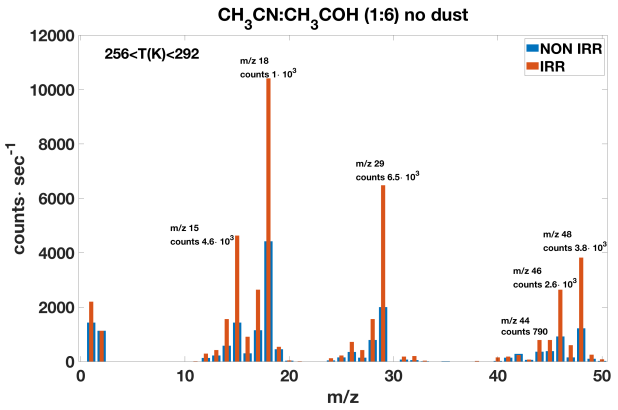

(a)

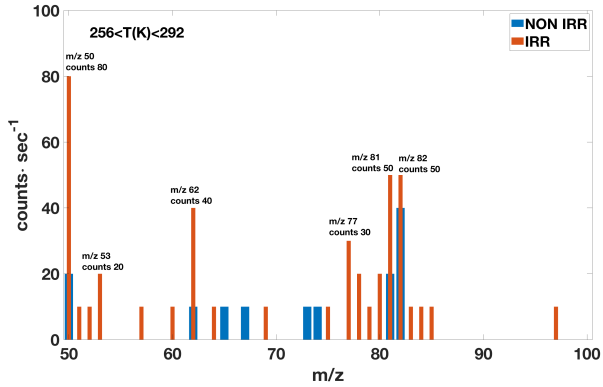

(b)

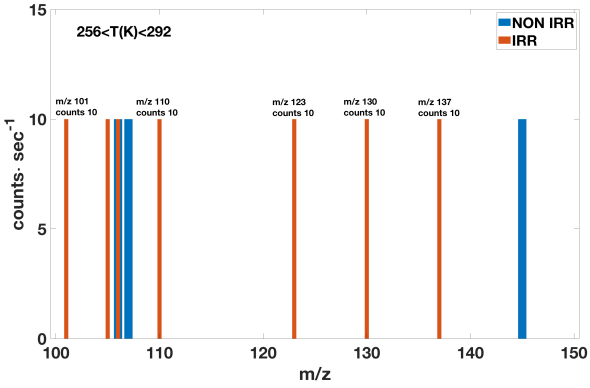

(c)

Figure 5.7: In all Figures, two experiments are reported. For both experiments, the figures show the CH_3CN:CH_3COH (1:6) mixture mass spectrum between zero and 50 m/z (Fig. a), 50 and 100 m/z (Fig. b), and between 100 and 150 m/z (Fig. c) during the thermal desorption between 256 and 292 K. The blue histograms show the ice mixture mass spectrum without the effects of UV irradiation, while the red histograms show how the mass spectrum changed after 8 hours of UV irradiation.

and between 50 and 100 m/z is shown in Figure 5.8 (a) and (b) respectively, while the spectrum at larger masses between 100 and 150 m/z and between 150 and 300 m/z is shown in Figure 5.9 (a) and (b). In both the experiment described by the blue and red histograms, the pure acetaldehyde after being deposited in the UHV chamber was subjected to 8 hours of UV irradiation at 17 K. The figures show the mass spectrum obtained during the thermal desorption of the irradiated acetaldehyde when the temperature was rising between 256 and 292 K.

The difference between the two experiments is that the blue histograms describe the mass spectrum of the irradiated acetaldehyde in the case in which it was condensed and desorbed directly by the nickel cold finger of the cryostat, while the red histograms describe the case in which the molecules were deposited on the micrometric grains of olivine used as substrate. The four Figures 5.8 and 5.9 (a) and (b) clearly show how the red histograms (desorption from olivine grains) are greater both in intensity and in counts (signals from new m/z) than the blue histograms.

After the same UV irradiation, in the presence of olivine grains, we can observe desorption of new species. For masses greater than 50 m/z and in the case in which the desorption occurred directly from the bare cold finger (blue histograms), Figures 5.8 (b) and 5.9 (a, and b) show peaks with greater intensity at least at 10 counts·sec^{-1} only at 50, 57, 60, 64, 81, 82, 118, 129, and 150 m/z. In all these cases, the intensity of the histograms never exceeded the value of 50 counts·sec^{-1}. On the other hand, for masses greater than 50 m/z and in the presence of olivine grains, the mass spectrum shows signals at almost all m/z values. The peak at 50 m/z increased from a value intensity of 50 counts·sec^{-1} in the absence of grains to almost 100 counts·sec^{-1} in presence of olivine, the one at 57 m/z grew from 20 to 70 counts·sec^{-1}, the one at 62 m/z from 10 to 140 counts·sec^{-1}, the one at 65 m/z from 20 to 440 counts·sec^{-1}, and those at 81 and 82 m/z reached the values of 70 and 90 counts·sec^{-1} respectively (Fig. 5.8 (b) and 5.9 (a, and b)). Species with masses at 69, 78, 84, 94, 97, 101, 102, 103, 105, 107, 110, 117, 121, 133, 142, 144, 145, 158, 163, 175, 176, 182, 191, 211, 214, and 271 m/z showed a signal only in the presence of the olivine substrate. In particular, in presence of olivine, the 102 m/z signal passed from a value of zero to 90 counts·sec^{-1}, the 105 m/z signal reached the value of 70 counts·sec^{-1}, and 107, 117, and 145 m/z reached the value of 50 counts·sec^{-1}. This result is the first evidence of the catalytic role played by olivine silicate in a dense molecular cloud simulated environment.

Moreover, Figure 5.8 (a) shows interesting results about the acetaldehyde signal at 44 m/z and that of its two radicals at 15 m/z (CH_3) and 29 m/z (HCO). While the 44 m/z signal was comparable between the two

experiments, the 15 m/z signal increased, passing from the value of $1.7{\cdot}10^3$ counts·sec^{-1} in the case of the bare cold finger (blue histogram) to the value of $1.9{\cdot}10^4$ counts·sec^{-1} in presence of olivine (red histogram), and the 29 m/z signal increased from the value of $2.3{\cdot}10^3$ counts·sec^{-1} (blue histogram) to the value of $2.7{\cdot}10^4$ counts·sec^{-1} in presence of olivine (red histogram).

Therefore, with the same UV irradiation, the intensity of the CH_3 and HCO signals increased when the desorption occurred from olivine grains. This result was already found in the previous experiments reported in chapter 4 and Corazzi et al., 2021 work. In that case, the molecules were not irradiated and we found that the 15 and 29 m/z signal intensity increased during the acetaldehyde thermal desorption from olivine grains. These signals desorbed at the same temperature as acetaldehyde and therefore, under a first analysis, they were associated with the cracking patterns of the parent molecule in the head of the mass spectrometer. However, we noticed a notable increase in the 29 and 15 m/z signal intensity, and in particular, the 15 m/z signal was nearly as intense as the 29 m/z signal, much higher than the expected amount of the cracking patterns. This result suggested that the presence of olivine catalyzes the carbon-carbon bond breaking of acetaldehyde molecule, as the carbon-carbon bond of adsorbed acetaldehyde breaks easily (e.g., Lai et al. 2008). This set of experiments also showed that olivine catalyzes the acetaldehyde dissociation into HCO and CH_3.

Acetonitrile CH_3CN Figures 5.10 and 5.11 show the full acetonitrile mass spectrum up to 300 m/z. The spectral range between 0 and 50 m/z and between 50 and 100 m/z is shown in Figure 5.10 (a) and (b) respectively, while the mass spectrum between 100 and 150 m/z and between 150 and 300 m/z is shown in Figure 5.11 (a) and (b). In both the experiment described by the blue and red histograms, the pure acetonitrile after being deposited in the UHV chamber was subjected to 8 hours of UV irradiation at 17 K and then heated at a constant rate of 1.21 K·sec^{-1} and desorbed. The Figures show the mass spectrum obtained during the thermal desorption of the irradiated acetonitrile in the temperature range between 256 and 292 K.

In agreement with the previous experiment, the blue histograms describe the mass spectrum of the irradiated acetonitrile in the absence of grains and the red histograms describe how the mass spectrum changed in presence of micrometric grains of olivine used as substrate. Even in the acetonitrile case, the four Figures 5.10 and 5.11 (a) and (b) clearly show how the red histograms (desorption from olivine grains) are greater both in intensity and in number than the blue histograms. Also in this case, the mass spectrum of acetonitrile desorbed from olivine grains shows signals at new m/z compared

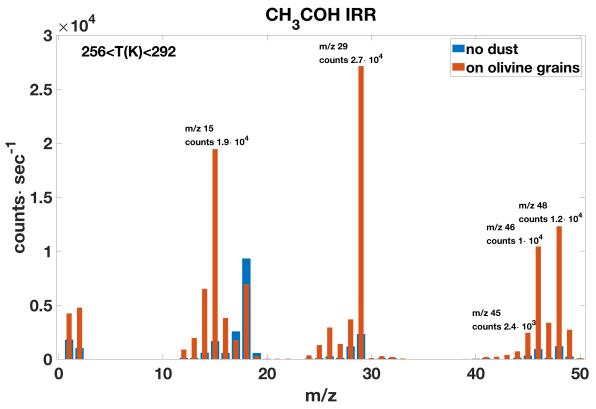

(a)

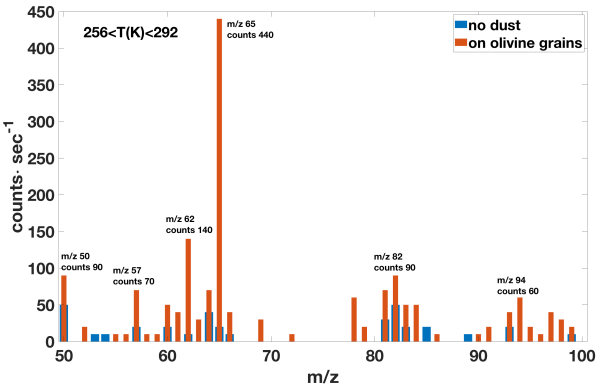

(b)

Figure 5.8: All Figures show two experiments. For both experiments, the figures display the acetaldehyde mass spectrum between zero and 50 m/z (Fig. a) and 50 and 100 m/z (Fig. b) after 8 hours of UV irradiation detected by the mass spectrometer during the molecules desorption when the temperature was rising from 256 to 292 K. The blue histograms describe the first experiment, i.e., the acetaldehyde mass spectrum obtained after UV irradiadtion without the mineral presence. So in that case, CH_3COH was deposited directly on the cold finger of the cryostat and subjected to UV irradiation. Red histograms show the results obtained when CH_3COH was deposited on olivine dust and then subjected to the same irradiation experiment (same UV flux and irradiation time, so same irradiation energy).

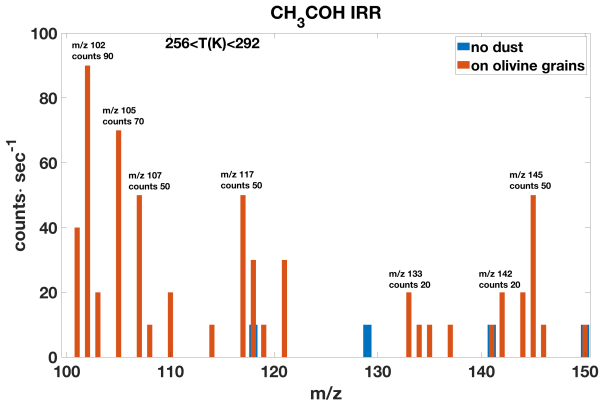

(a)

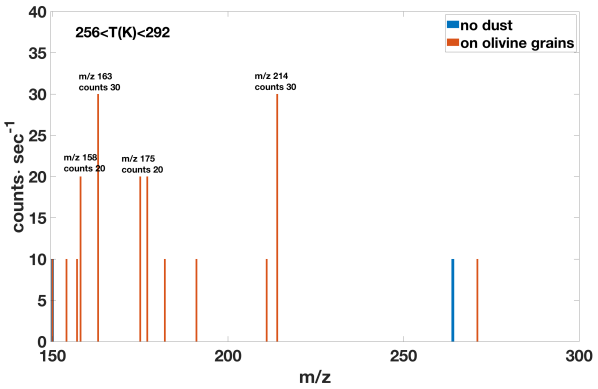

(b)

Figure 5.9: All Figures show two experiments. For both experiments, the figures display the acetaldehyde mass spectrum between 100 and 150 m/z (Fig. a) and 150 and 300 m/z (Fig. b) after 8 hours of UV irradiation detected by the mass spectrometer during the molecules desorption when the temperature was rising from 256 to 292 K. The blue histograms describe the first experiment, i.e., the acetaldehyde mass spectrum obtained after UV irradiadtion without the mineral presence. So in that case, CH_3COH was deposited directly on the cold finger of the cryostat and subjected to UV irradiation. Red histograms show the results obtained when CH_3COH was deposited on olivine dust and then subjected to the same irradiation experiment (same UV flux and irradiation time, so same irradiation energy).

to the cold finger case, so the spectrum reveals the presence of new species. With the same UV irradiation, the mass spectrum of acetonitrile confirms a catalytic role played by the mineral.

When the acetonitrile irradiation and desorption occurred from micrometric grains of olivine (red histograms), the mass spectrum shows more intense signals for almost all m/z values compared to the blue histograms (Figures 5.10 (a), and b) and 5.11 (a, and b)). For example, the acetonitrile peak at 41 m/z increased from a value intensity of 10^2 counts·sec^{-1} in the absence of grains to 10^3 counts·sec^{-1} in presence of olivine, the one at 44 m/z grew from $\sim 10^2$ to $2.7 \cdot 10^3$ counts·sec^{-1}, the one at 57 m/z increased from 20 to 170 counts·sec^{-1}, the one at 62 m/z passed from 30 to 390 counts·sec^{-1}, the one at 64 m/z from 10 to 210 counts·sec^{-1}, the one at 65 m/z from 140 to 690 counts·sec^{-1}, the one at 69 m/z from 20 to 120 counts·sec^{-1}, those at 81 and 82 m/z reached the value of 150 counts·sec^{-1}, the one at 97 m/z increased from 10 to 100 counts·sec^{-1}, the peaks at 101 and 102 m/z reached the value of 90 and 160 counts·sec^{-1} respectively, those at 131 and 133 m/z increased to 120 and 180 counts·sec^{-1} respectively, and the peak at 134 m/z grew from 20 to 60 counts·sec^{-1}.

With the same UV radiation, the masses at 63, 70, 73, 75 (signal intensity of 20 counts·sec^{-1}), 93, 100, 105, 107, 109, 110, 121, 122, 126, 141, and 150 m/z showed a signal only in the presence of the olivine substrate. Figure 5.11 (b) shows only the mass spectrum in the range between 150 and 300 m/z. From this figure, we can realize that the blue histograms (absence of grains) are only 4 (corresponding to 151, 155, 158, and 163 m/z). On the other hand, the red histograms are clearly in greater number. Among these, we can note the signals at 150, 175, 177, and 190 m/z.

Ice mixture CH_3CN:CH_3COH (1:6) Figures 5.12 and 5.13 (a, and b) show the mass spectrum up to 300 m/z of the ice mixture CH_3CN:CH_3COH (1:6) subjected to 8 hours of UV irradiation when the desorption occurred from the bare cold finger of the cryostat (blue histograms) and olivine grains (red histograms). Even with the mixture, the same trend found with single molecules was observed. The red histograms are greater both in number and intensity than the blue ones.

Figure 5.12 (a) reveals that, with the same UV irradiation, the intensity of the CH_3 (15 m/z) and HCO (29 m/z) signals increased in presence of olivine grains (red histograms). The 15 m/z signal grew from the value of $4.6 \cdot 10^3$ counts·sec^{-1} during the cold finger experiment (blue histogram) to the value of $1.7 \cdot 10^4$ counts·sec^{-1} during the olivine experiment (red histogram), and the 29 m/z signal increased from $6.5 \cdot 10^3$ counts·sec^{-1} to $1.98 \cdot 10^4$ counts·sec^{-1}.

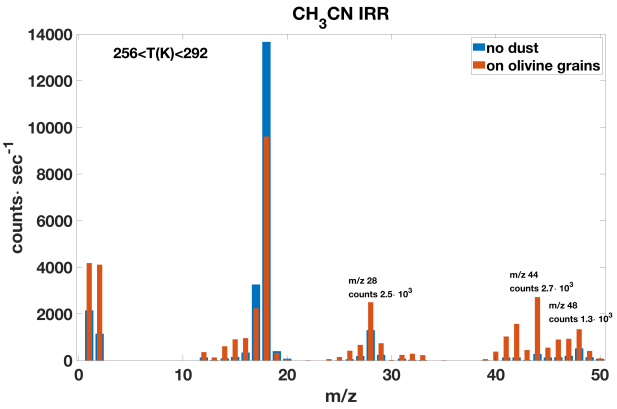

(a)

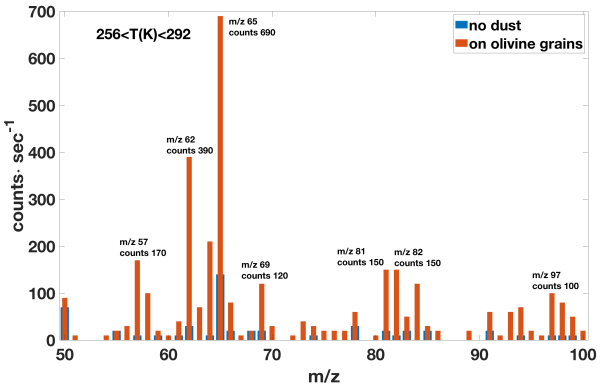

(b)

Figure 5.10: All Figures show two experiments. For both experiments, the figures display the acetonitrile mass spectrum between zero and 50 m/z (Fig. a) and 50 and 100 m/z (Fig. b) after 8 hours of UV irradiation detected by the mass spectrometer during the molecules desorption when the temperature was rising from 256 to 292 K. The blue histograms describe the first experiment, i.e., the acetonitrile mass spectrum obtained after UV irradiadtion without the mineral presence. So in that case, CH_3CN was deposited directly on the cold finger of the cryostat and subjected to UV irradiation. Red histograms show the results obtained when CH_3CN was deposited on olivine dust and then subjected to the same irradiation experiment (same UV flux and irradiation time, so same irradiation energy).

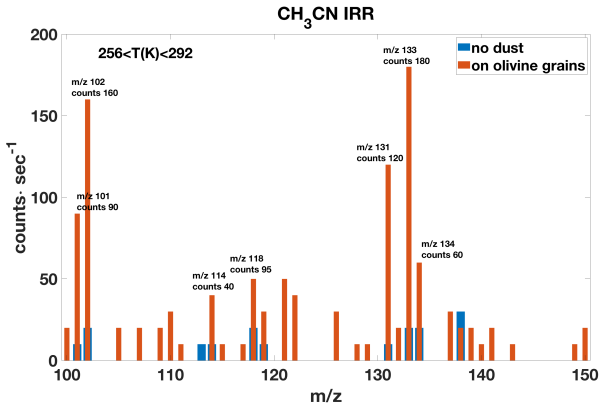

(a)

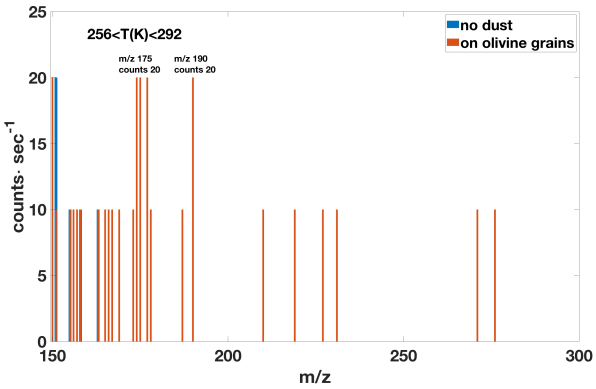

(b)

Figure 5.11: All Figures show two experiments. For both experiments, the figures display the acetonitrile mass spectrum between 100 and 150 m/z (Fig. a) and 150 and 300 m/z (Fig. b) after 8 hours of UV irradiation detected by the mass spectrometer during the molecules desorption when the temperature was rising from 256 to 292 K. The blue histograms describe the first experiment, i.e., the acetonitrile mass spectrum obtained after UV irradiadtion without the mineral presence. So in that case, CH_3CN was deposited directly on the cold finger of the cryostat and subjected to UV irradiation. Red histograms show the results obtained when CH_3CN was deposited on olivine dust and then subjected to the same irradiation experiment (same UV flux and irradiation time, so same irradiation energy).

So, the signals associated with the two acetaldehyde radicals are about three times higher in the presence of the silicate. This result confirms what was found in the case of pure acetaldehyde (Fig. 5.8 (a)), i.e., the dust plays an active role.

Moreover, the ice mixture spectrum shows that the intensity of all signals between 0 and 50 m/z increased in the presence of olivine (5.12 (a)). The peak at 50 m/z passed from a value of 70 counts·sec^{-1} to 130 counts·sec^{-1}, the one at 57 m/z reached the value of 200 counts·sec^{-1}, the signals at 62 and 64 m/z got the value of 120 counts·sec^{-1}, the one at 69 m/z increased to 130 counts·sec^{-1}, and those at 81 and 84 m/z got the values of 100 and 70 counts·sec^{-1} respectively (Fig. 5.12 (b)). We also note that with the same UV radiation, many new mass signals were observed only in the presence of olivine substrate. Specifically, the 65 m/z showed a signal only with olivine reaching a value of 310 counts·sec^{-1}, like those at 102 m/z (110 counts·sec^{-1}), 107 (50 counts·sec^{-1}), 129 m/z (40 counts·sec^{-1}), 145 m/z (70 counts·sec^{-1}), and those at 158 and 163 m/z (30 counts·sec^{-1}).

5.1.3 UV radiation and olivine grains

In this subsection, we will compare the mass spectra of the molecules desorbed from grains before UV irradiation and after being photo-processed.

Acetaldehyde CH_3COH Figures 5.14, and 5.15 show how the mass spectrum of the acetaldehyde deposited on the olivine grains changed after 8 hours of UV irradiation. Also, in this case, the blue and red histograms describe two experiments respectively. For both experiments, the same amount of acetaldehyde was deposited at 17 K on the cold finger covered with olivine grains and then desorbed by heating it at a constant rate. The figures show the full acetaldehyde spectrum up to 300 m/z detected by the mass spectrometer during the thermal desorption when the temperature was rising from 258 to 294 K. The spectral range between 0 and 100 m/z is shown in Figure 5.14 (a, and b), while the spectral range between 100 and 300 m/z is reported in Figure 5.15 (a, and b). The first experiment described by the blue histograms concerns the acetaldehyde thermal desorption from olivine grains without the UV radiation presence. The red histograms, on the other hand, show how the spectrum changed after 8 hours of UV irradiation. Now, the blue histograms (thermal desorption without UV radiation) are greater both in number and in intensity than the red ones even for large m/z values (see Fig. 5.15 (b)).

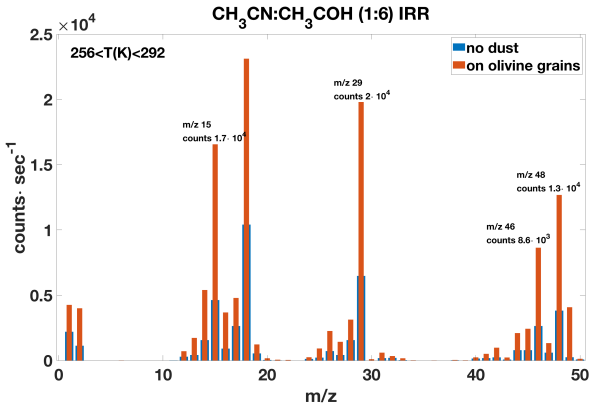

(a)

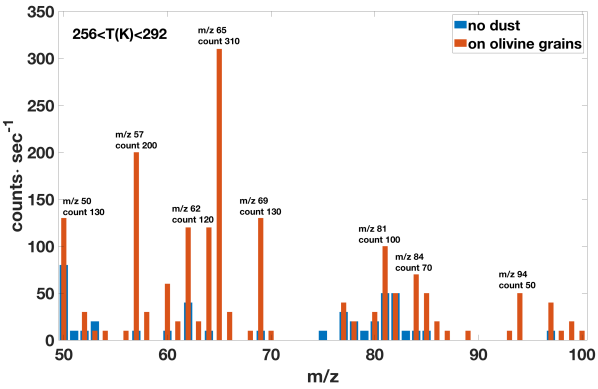

(b)

Figure 5.12: All Figures shows two experiments. For both experiments, the figures display the ice mixture CH_3CN:CH_3COH (1:6) mass spectrum between zero and 50 m/z (Fig. a) and 50 and 100 m/z (Fig. b) after 8 hours of UV irradiation detected by the mass spectrometer during the thermal desorption (the temperature was rising from 256 to 292 K). The blue histograms describe the first experiment, i.e., the mass spectrum after UV irradiadtion without the mineral presence. In that case, the ice mixture was deposited directly on the cold finger of the cryostat and subjected to UV irradiation. Red histograms show the results obtained when the ice mixture was deposited on olivine dust and then subjected to the same irradiation experiment (same UV flux and irradiation time, so same irradiation energy).

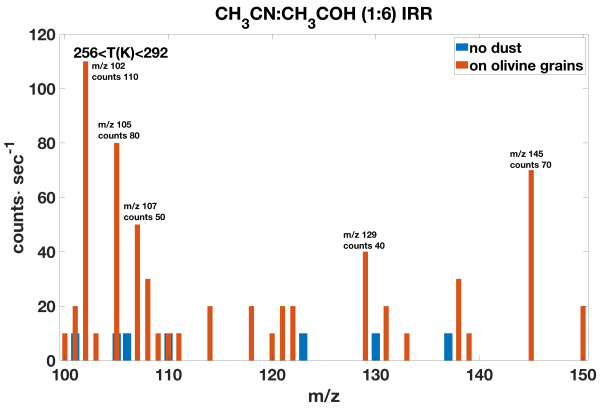

(a)

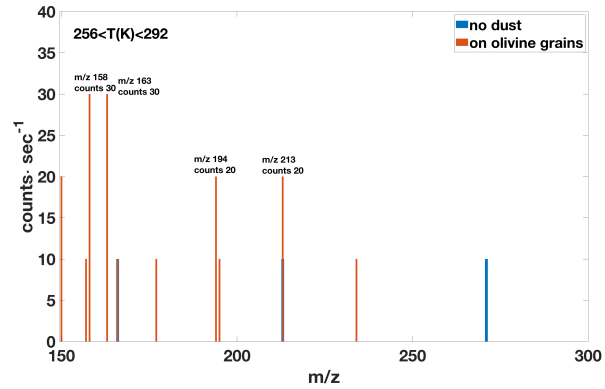

(b)

Figure 5.13: All Figures show two experiments. For both experiments, the figures display the ice mixture CH_3CN:CH_3COH (1:6) mass spectrum between 100 and 150 m/z (Fig. a) and 150 and 300 m/z (Fig. b) after 8 hours of UV irradiation detected by the mass spectrometer during the thermal desorption (the temperature was rising from 256 to 292 K). The blue histograms describe the first experiment, i.e., the mass spectrum after UV irradiadtion without the mineral presence. In that case, the ice mixture was deposited directly on the cold finger of the cryostat and subjected to UV irradiation. Red histograms show the results obtained when the ice mixture was deposited on olivine dust and then subjected to the same irradiation experiment (same UV flux and irradiation time, so same irradiation energy).

Figures 5.3, 5.5, and 5.7 showed how the mass spectra of both the single molecules and the mixture were enriched with new signals even for large values of m/z after UV irradiation, i.e., the experiments showed a UV radiation role in producing new species. Those measurements were done on the bare cold finger without the presence of the mineral olivine. By repeating the same measurements with acetaldehyde deposited on olivine grains used as a substrate, UV radiation no longer plays a catalytic role in forming new species. In fact, for masses greater than 50 m/z (Fig. 5.14 (b), and 5.15 (a, and b)), the signal obtained without irradiation (blue histograms) was always greater than the signal obtained after irradiation. For example, the signal at 50 m/z did not change after irradiation, the one at 64 m/z decreased from 230 counts·sec^{-1} to 70 counts·sec^{-1} after irradiation, the one at 65 m/z decreased from 470 to 440 counts·sec^{-1}, the one at 84 m/z reduced its value from 270 to 50 counts·sec^{-1}, and the one at 102 m/z from 160 to 90 counts·sec^{-1}. Furthermore, the masses at 153, 192, 193, 206, and 250 m/z showed a signal only in the non-irradiated case. Instead, the acetaldehyde fragments (signals at 15 and 29 m/z) increased their signal after irradiation. The methyl radical CH_3 signal increased its intensity from the value of $1{\cdot}10^4$ to $2{\cdot}10^4$ counts·sec^{-1} and that formyl radical HCO increased from $1.2{\cdot}10^4$ to $2.7{\cdot}10^4$ counts·sec^{-1}.

Acetonitrile CH_3CN Concerning acetaldehyde, by comparing the thermal desorption from olivine grains in the case in which the molecules were pure and irradiated, any increase in the signal after irradiation was observed. UV radiation did not appear to play a role in the formation of new species in the case of acetaldehyde deposited at 17 K on olivine. Now, we will make a comparison between the mass spectrum before and after UV irradiation in the case of acetonitrile deposited on olivine grains. Figures 5.16, and 5.17 show how the mass spectrum of acetonitrile condensed at 17 K on olivine grains changed after 8 hours of UV irradiation.

In the case of acetonitrile, the red histograms (acetonitrile thermal desorption from olivine grains after UV irradiation) are visibly greater in both number and intensity than the blue histograms (non-irradiated samples). After UV irradiation, the 41 m/z signal (acetonitrile molecular weight) increased from 420 to 1030 counts·sec^{-1}, the 42 m/z signal from 690 to 1570 counts·sec^{-1}, and the 44 m/z signal (associated with tracking in the mass spectrometer of the 45 m/z signal due to the hydrogenation of acetonitrile) from 1220 to 2720 counts·sec^{-1}. With the same presence of the olivine substrate, the signals between 40 and 44 m/z doubled their intensity after the sample was subjected to UV irradiation. The 45 m/z signal grew from 90 to

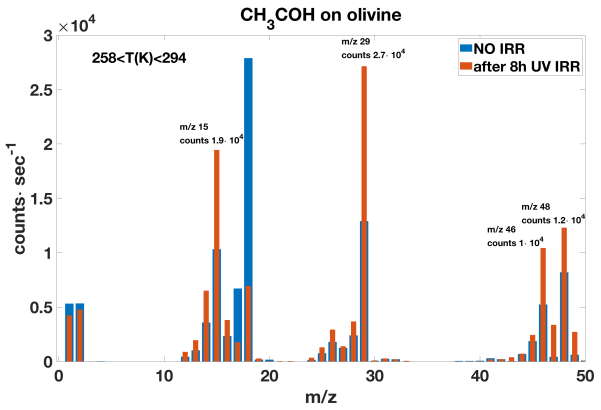

(a)

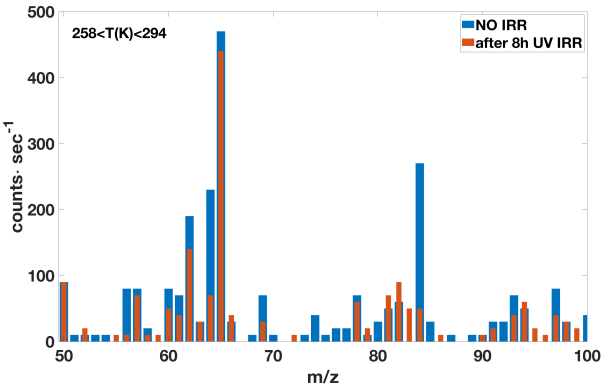

(b)

Figure 5.14: All Figures show two experiments. For both experiments, acetaldehyde was first deposited on olivine grains at 17 K and then heated at a constant rate. The figures display the acetaldehyde mass spectrum between zero and 50 m/z (Fig. a) and between 50 and 100 m/z (Fig. b) obtained during the molecules desorption when the temperature was rising from 258 to 294 K. The blue histograms describe the first experiment, i.e., the acetaldehyde thermal desorption from olivine grains without the UV radiation presence. The red histograms show the signal obtained after 8 hours of UV irradiation.

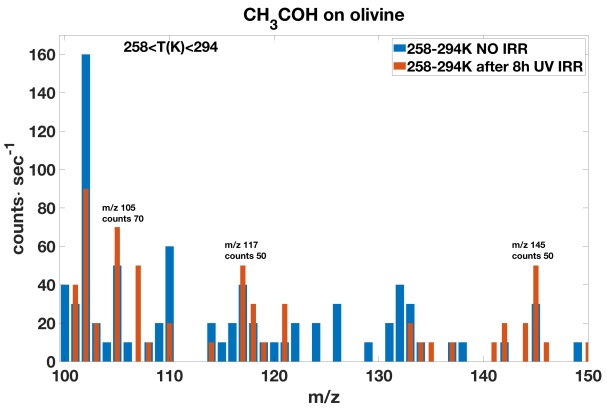

(a)

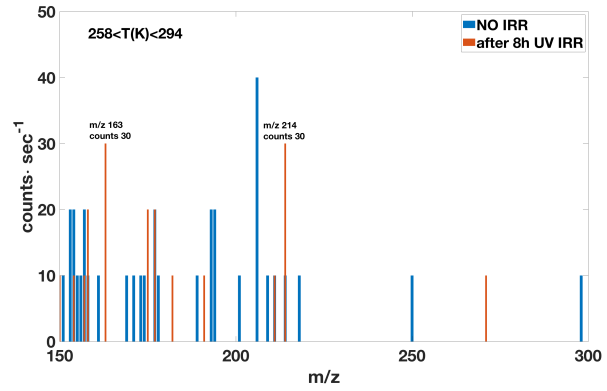

(b)

Figure 5.15: All Figures show two experiments. For both experiments, acetaldehyde was first deposited on olivine grains at 17 K and then heated at a constant rate. The figures display the acetaldehyde mass spectrum between 100 and 150 m/z (Fig. a) and between 150 and 300 m/z (Fig. b) obtained during the molecules desorption when the temperature was rising from 258 to 294 K. The blue histograms describe the first experiment, i.e., the acetaldehyde thermal desorption from olivine grains without the UV radiation presence. The red histograms show the signal obtained after 8 hours of UV irradiation.

550 counts·sec^{-1}, the 47 m/z signal from 90 to 930 counts·sec^{-1}, and the 48 m/z signal from 280 to 1340 counts·sec^{-1} (Fig. 5.16 (a)). The same trend was confirmed by Figure (b). For example, the 57 m/z signal increased in intensity from a value of 40 counts·sec^{-1} to 170 after irradiation, that one at 62 m/z from 30 to 390, that one at 64 m/z from 70 to 210, that one at 65 m/z from 100 to 690, that one at 81 m/z from 60 to 150, that one at 82 m/z from 40 to 150, that one at 84 m/z from 30 to 120, and that at 97 m/z from 20 to 100. The highest m/z part of the mass spectrum (Figure 5.17 (a) and (b)) confirmed the catalytic action of UV radiation. After irradiation, the 101 m/z signal appeared reaching a value of 90 counts·sec^{-1}, the one at 131 m/z reached an intensity of 120 counts·sec^{-1}, the one at 133 m/z got a value of 180, and the one at 134 m/z got a value of 60. Moreover, only after irradiation, the signals at 174, 175, and 190 m/z appeared.

During the bare cold finger experiments, we found that the UV radiation role in producing signals at new m/z and increasing their intensity was more evident with acetonitrile than with acetaldehyde, where the UV radiation role appeared to be primarily to boost the signal of the two radicals. This aspect is even more evident in this set of measurements in the presence of olivine. In fact, these experiments in which the single molecules were condensed on olivine grains and then subjected to UV irradiation showed that the action of the radiation was more relevant in the case of acetonitrile (Figs. 5.16 and 5.17) than acetaldehyde (Figs 5.14 and 5.15). In the case of acetaldehyde on olivine, the counts did not increase after irradiation (blue histograms appeared greater than reds). Thus, when the molecules were already condensed on the mineral, the action of the radiation mainly concerned acetonitrile.

Ice mixture CH_3CN:CH_3COH (1:6) Finally, Figures 5.18 and 5.19 show the mass spectrum obtained when the CH_3CN:CH_3COH (1:6) mixture thermally desorbed from olivine grains (blue histograms) and how this spectrum changed after 8 hours of UV irradiation (red histograms). Again, the red histograms dominate over the blue ones. Previous experiments with single molecules condensed on olivine grains showed that UV radiation primarily changed the acetonitrile mass spectrum relative to acetaldehyde. In the case of the mixture, therefore, we can infer that the increase of the signal after irradiation was due to the interaction between the radiation and acetonitrile both in terms of new masses observed and of increase of peaks intensities. The role of acetaldehyde was mainly to provide the radicals HCO and CH_3.

Indeed, Figure 5.18 (a) shows the ice mixture mass spectrum between 0 and 50 m/z. The first thing we notice is the increase after irradiation of the

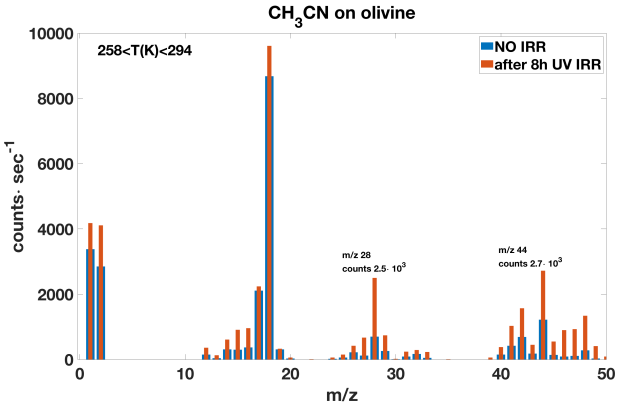

(a)

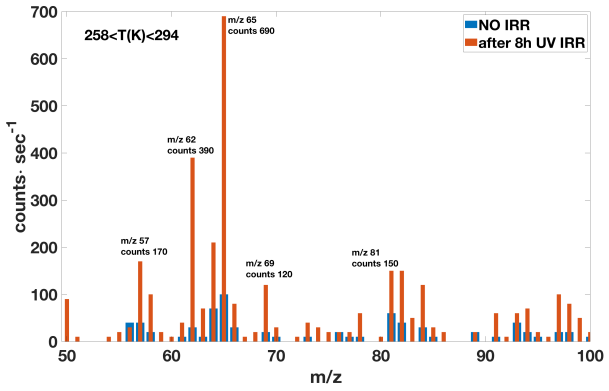

(b)

Figure 5.16: All Figures show two experiments. For both experiments, acetonitrile was first deposited on olivine grains at 17 K and then heated at a constant rate. The figures display the acetonitrile mass spectrum between zero and 50 m/z (Fig. a) and 50 and 100 m/z (Fig. b) obtained during the molecules desorption when the temperature was rising from 258 to 294 K. The blue histograms describe the first experiment, i.e., the acetonitrile thermal desorption from olivine grains without the UV radiation presence.The red histograms show the signal after 8 hours of UV irradiation.

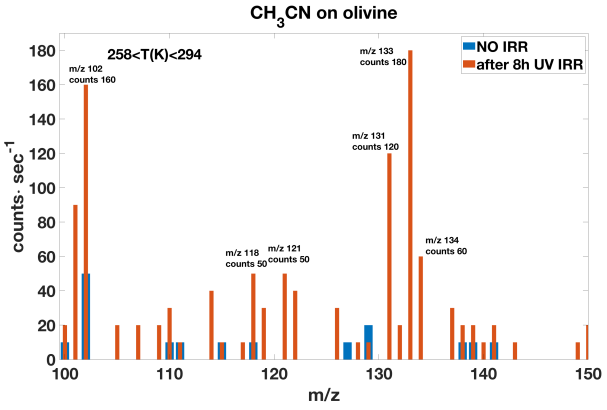

(a)

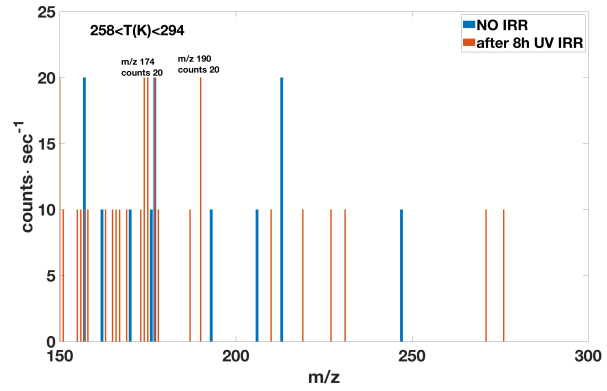

(b)

Figure 5.17: All Figures show two experiments. For both experiments, acetonitrile was first deposited on olivine grains at 17 K and then heated at a constant rate. The figures display the acetonitrile mass spectrum between 100 and 150 m/z (Fig. a) and 150 and 300 m/z (Fig. b) obtained during the molecules desorption when the temperature was rising from 258 to 294 K. The blue histograms describe the first experiment, i.e., the acetonitrile thermal desorption from olivine grains without the UV radiation presence. The red histograms show the signal after 8 hours of UV irradiation.

signals at 15 and 29 m/z (CH_3 and HCO respectively). The intensity of CH_3 signal increased from 4450 to 16560 counts·sec^{-1} (almost four times), while that of HCO from 5940 to 19800 counts·sec^{-1} (three times). In the case of acetonitrile (Fig 5.16 (a)), despite a general increase in the signal of all masses after irradiation, signals at 15 and 29 m/z showed no such increment. We can therefore associate these two signals to the two radicals provided by acetaldehyde. The other peaks instead reflect the results provided by acetonitrile. After UV irradiation, the 41 m/z acetonitrile signal went from an initial value of 200 counts·sec^{-1} to a final value of 510 counts·sec^{-1}, comparable to the acetonitrile mass spectrum desorbed from olivine. The 44 m/z signal increased from 520 to 2100 counts·sec^{-1}, which is quadrupled. In the case of acetonitrile alone, the 44 m/z signal from olivine was doubled after UV irradiation, but now the peak at 44 m/z was not only given by the tracking of the 45 m/z signal due to acetonitrile but also from the acetaldehyde signal itself. The 46 m/z signal increased from 1760 to 8640 counts·sec^{-1}, and the 48 m/z signal from 2280 to 12680 counts·sec^{-1} (Fig. 5.18 (a)).

After UV irradiation, larger m/z peaks appeared, such as the signal at 50 m/z (130 counts·sec^{-1}), 57 m/z (200 counts·sec^{-1}), 62 and 64 m/z (120 counts·sec^{-1}), 65 m/z (310 counts·sec^{-1}), 69 m/z (130 counts·sec^{-1}), 84 m/z (70 counts·sec^{-1}), and the signals at 81 and 82 m/z are both incremented from 20 counts·sec^{-1} to 100 and 50 counts·sec^{-1} respectively (Fig. 5.18 (b)). Signals relating to masses greater than 100 m/z (Fig. 5.19) appeared only after UV irradiation (red histograms). For example, the signals at 102, 105, 107, 145, e 163 m/z were observed only after irradiation.

5.2 Discussion and astrophysical implication

5.2.1 The effects of UV radiation and iCOMS in PDRs

Mass spectra of pure acetaldehyde deposited on the bare cold finger after 8 hours of UV irradiation at 17 K showed that there was an increase of the signal at 15 m/z, which was associated with the radical CH_3 due to the cracking patterns of dissociation of the acetaldehyde inside the mass spectrometer. This signal almost doubled its intensity after UV irradiation, rising from 5 to $8{\cdot}10^4$ counts·sec^{-1} and became almost as intense as the 29 m/z signal, associated with the formyl radical. Such an intense 15 m/z signal is greater than that predicted by the cracking patterns and spectra available on NIST. Although the most evident role of UV radiation on acetaldehyde is to favor the formation of the two radicals HCO and CH_3, new peaks at greater masses are observed especially in the range from 50 to 100 m/z (Fig.

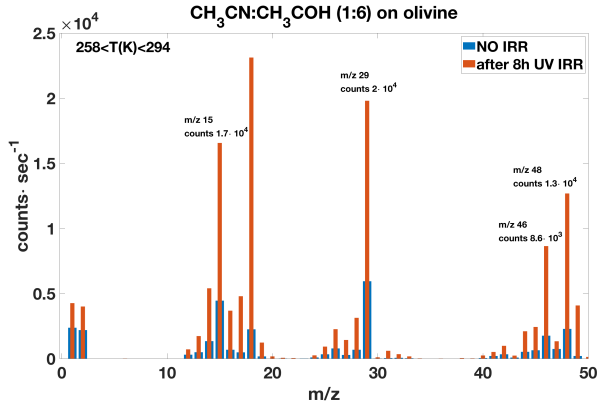

(a)

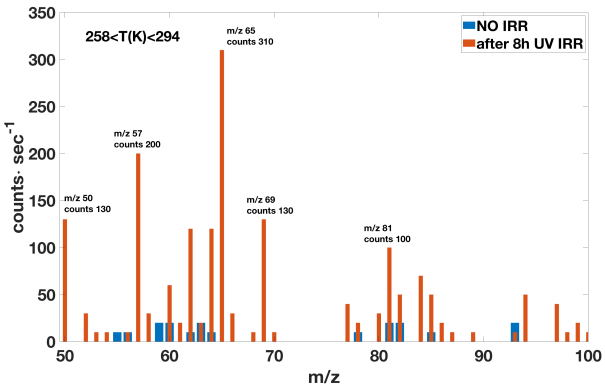

(b)

Figure 5.18: All Figures show two experiments. For both experiments, acetonitrile and acetaldehyde were deposited in the pre-chamber where the ice mixture with the ratio 1:6 was obtained following the partial pressures of the molecules. Then the ice mixture was deposited in the UHV chamber and condensed on micrometric grains of olivine at 17 K. After condensation, the sample was heated at a constant rate of 1.21 K· sec^{-1}. As the cold finger warmed, the condensed molecules desorbed, entered the mass spectrometer, and were detected. The figures display the ice mixture mass spectrum in the range between zero and 50 m/z (Fig. a) and 50 and 100 m/z (Fig. b) detected by the mass spectrometer during the thermal desorption when the temperature was rising from 258 to 294 K. The blue histograms describe the first experiment, i.e., the ice mixture thermal desorption from olivine grains without the UV radiation presence. The red histograms show the signal after 8 hours of UV irradiation.

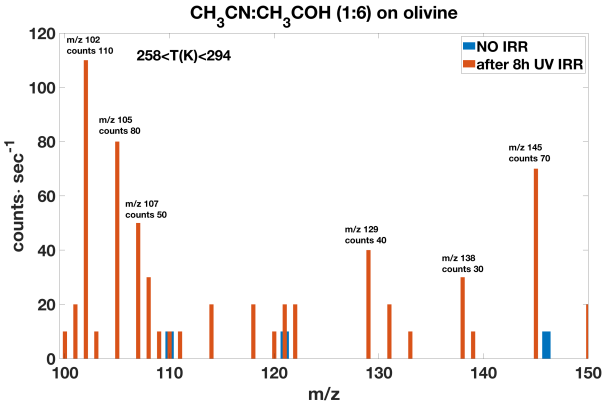

(a)

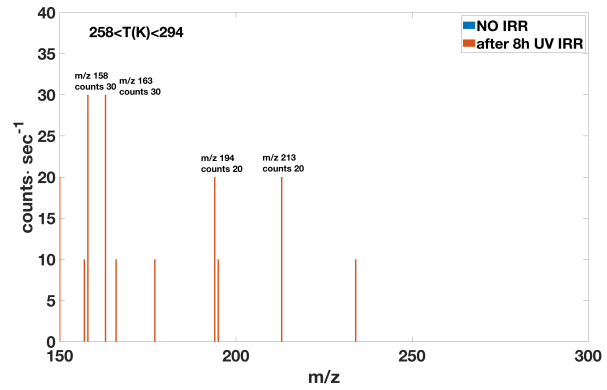

(b)

Figure 5.19: All Figures show two experiments. For both experiments, acetonitrile and acetaldehyde were deposited in the pre-chamber where the ice mixture with the ratio 1:6 was obtained following the partial pressures of the molecules. Then the ice mixture was deposited in the UHV chamber and condensed on micrometric grains of olivine at 17 K. After condensation, the sample was heated at a constant rate of 1.21 K· sec^{-1}. As the cold finger warmed, the condensed molecules desorbed, entered the mass spectrometer, and were detected. The figures display the ice mixture mass spectrum in the range between 100 and 150 m/z (Fig. a) and 150 and 300 m/z (Fig. b) detected by the mass spectrometer during the thermal desorption when the temperature was rising from 258 to 294 K. The blue histograms describe the first experiment, i.e., the ice mixture thermal desorption from olivine grains without the UV radiation presence. The red histograms show the signal after 8 hours of UV irradiation.

5.3 a).

In the case of pure acetonitrile, we observed that the T_{des} increased and shifted towards higher values after UV irradiation (Fig. 5.4). One of the possible interpretations for this shift could be that UV radiation released energy to the acetonitrile and thus the ice settled into a new more stable geometric configuration. Otherwise, one might think that UV irradiation formed new species and that we are therefore witnessing thermal desorption no longer from a matrix of acetonitrile alone. In support of this second hypothesis, Bulak et al., 2020 studied in laboratory pure CH_3CN ices at 20 K subjected to UV irradiation with a flux of $1.6{\cdot}10^{17}$ photons·cm^{-2}. They verified that 35% of the parent species was photoconverted. Figure 5.5 confirms that hypothesis.

By depositing CH_3CN:CH_3COH (1:6), before irradiation, we measured the ratios [HCO]/[CH_3CN] $\sim$ 14 and [CH_3]/[CH3CN] $\sim$ 11. In the presence of olivine without any UV irradiation, new ratios are [HCO]/[CH_3CN] $\sim$ 26 and [CH_3]/[CH_3CN] $\sim$ 19, almost double than that of the case without grains. This confirms the result found in our work Corazzi et al. 2021. The presence of olivine catalyzes the breakdown of the carbon-carbon bond of the acetaldehyde molecule, since the carbon-carbon bond of the adsorbed acetaldehyde is easily broken (e.g., Lai et al. 2008). In the case of photoprocessing of ice mixtures both pure and deposited on olivine, the ratios are similar and increased to [HCO]/[CH_3CN] $\sim$ 43 and [CH_3]/[CH_3CN] $\sim$ 31, confirming the photodissociation of acetaldehyde. A large amount of iCOMS are observed in photon-dominated regions (PDRs), e.g., (Kemper et al. 1999, Wyrowski et al. 2000, Savage et al. 2004), and in the UV-exposed atmospheres of planet-forming disks (Le Gal et al. 2019). In these environments, a high [HCO]/[CH_3CN] ratio is expected from our experiments. This expectation is confirmed by the values observed by the HARP instrument on the JCMT, which revealed 63 molecular species in the 330-373 GHz range in the W49A star-forming region. In this environment, the chemistry is driven by UV irradiation mainly in the northern clump, eastern tail, and southwest clump regions where [HCO]/[CH_3CN] $\sim$ 100 was observed (Nagy et al. 2015). From our results, this high ratio would be evidence of the presence of photoprocessing of acetaldehyde ice.

5.2.2 The catalytic role of olivine and the high masses observed

We studied the mass spectra of acetaldehyde, acetonitrile, and of the mixture CH_3CN: CH_3COH (1:6) subjected to 8 hours of UV irradiation on the bare

cold finger and micrometric grains of olivine. The aim was to see, with the same UV radiation, how the mass spectra changed in the presence of grains. Both in the case of simple molecules and of the mixture, the mass signals increased both in number (peaks relative to new m/z) and intensity when desorption occurred in the presence of olivine (red histograms of Figs. 5.8, 5.9, 5.10, 5.11, 5.12, 5.13). We noticed that olivine is efficient in producing new species at higher m/z values.

Two complementary roles are envisaged where the mineral is the catalyst of addition reactions of the aldolic type, while the UV radiation acts as an activator, increasing the acidity in the excited state of the compounds. Through addition reactions of the aldolic type, it is possible to explain the presence of some observed high m/z signals, such as the signals at 126, 206, 81, and 190 m/z. Combining the UV radiation which acts as an activator and the mineral which acts as a catalyst, an addition reaction between acetaldehyde and acetonitrile could give rise to CH_3-COH-CH_3-CN (85 m/z). This last molecule with an addition reaction with acetonitrile gives rise to CH_3-COH-CH_2-CNH-CH_3-CN ($C_6H_{10}N_2O$ 126 m/z) (first line of the sketch shown in Figure 5.20). Again, through addition reactions, the 126 m/z signal gives rise with two acetonitrile molecules to $C_{10}H_{16}N_4O$ molecule (208 m/z), which produces the 206 m/z signal observed losing two hydrogen atoms (column left of the sketch shown in Figure 5.20). Once the signal at 126 m/z is obtained through addition reactions, it can produce a signal at 108 m/z ($C_6H_8N_2$) by losing a water molecule. The $C_6H_8N_2$ molecule in turn can explain the signal observed at 81 m/z by losing an HCN molecule and forming C_5H_7N. Moreover, the $C_6H_8N_2$ molecule at 108 m/z can give rise to the 190 m/z signal ($C_{10}H_{14}N_4$) through an addition reaction with two acetonitrile molecules (column on the right of the sketch shown in Figure 5.20). As far as we know, there are no observations of such high molecular masses in space. However, our experiments show that molecules with high mass such as 190 or 206 m/z must be present in star-forming regions where acetaldehyde and acetonitrile have been observed and where UV radiation and silicates are playing an active role.

We can summarize the main results obtained with the three sets of experiments:

- By depositing CH_3CN:CH_3COH (1:6), the value of the [HCO]/[CH_3CN] measured ratio tripled following the photoprocessing of the mixture, confirming the photodissociation of the acetaldehyde. Hence, our experiments show that the presence of acetaldehyde ice photoprocessing contributes to the high [HCO]/[CH_3CN] ratios observed in star-forming

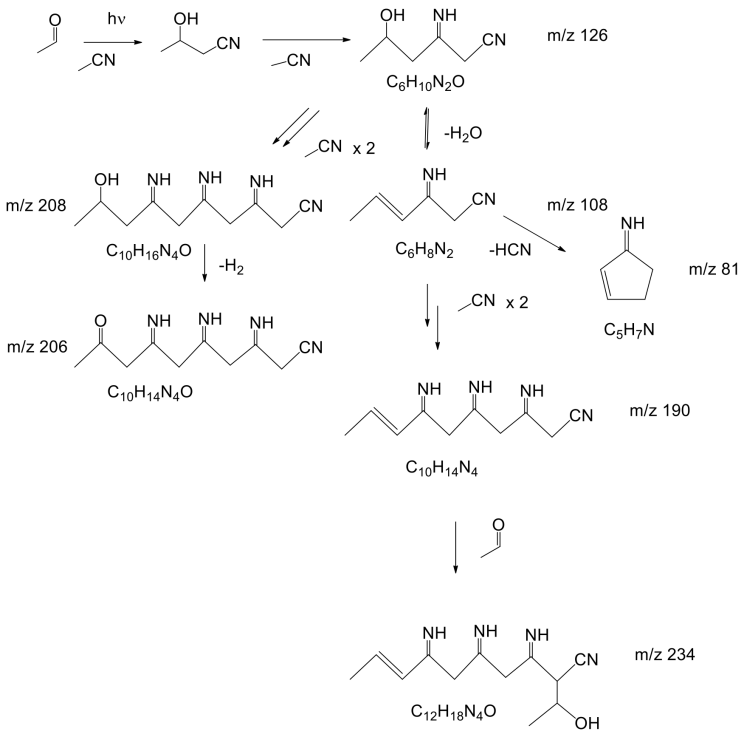

Figure 5.20: The figure shows the aldol type addition reactions that can occur between acetonitrile and acetaldehyde following UV irradiation.

regions (Nagy et al. 2015).

- Our experiments show that olivine is efficient in producing new species at higher m/z values. Through addition reactions of the aldolic type in which the mineral acts as a catalyst and the radiation as an activator, we can explain some of the signals observed at high values of m/z (example 126, 206, 81, 190 m/z). Although, as far as we know, there are no observations of such high molecular masses in space, we expect these signals to be present in star-forming regions where acetaldehyde and acetonitrile have been observed and where UV radiation and silicates are involved in an active role.

Chapter 6

Conclusions

This thesis work addresses the main activities of my three-year Ph.D. project carried out at the Department of Physics and Astronomy of the University of Florence in collaboration with the INAF-Arcetri Astrophysical Observatory. The project was developed as part of the research projects "Space life-OPPS" and "Reservoirs for Planetary Atmospheres". My Ph.D. focused on laboratory studies on photoprocessing and thermal desorption of iCOMs such as formamide, acetonitrile, and acetaldehyde in simulated space conditions.

In the introduction, we highlighted how an ever-increasing number of iCOMs are continuously detected along the formation process of a Sun-like star thanks to millimeter and centimeter observations. About 200 different molecular species have been detected in the interstellar and circumstellar medium, and 40 new iCOMs have been detected for the first time in the last two years. Thus, the number of revealed iCOMs and their chemical complexity is expected to grow over the years. Large interferometers in the (sub)mm range, such as IRAM-NOEMA and ALMA, showed the presence of iCOMs from the early stages of star formation such as pre-stellar dense cores (e.g., Bacmann et al. 2012), to protoplanetary disks (Walsh et al. 2016), the place where planets form. The discovery of new complex molecules in different space environments leads us to ask how organic chemistry works in space, how individual elements such as carbon, hydrogen, oxygen, and nitrogen are found in the form of complex organic molecules, how the chemical complexity we observe today originated, what is the chemistry that occurs along the formation process of stars and planets like ours.

In laboratory, it is possible to simulate interstellar ices analogs, formed by molecules mixed with grains, to process them, and to study their evolution, degradation, and preservation. To study the evolution in simulated space conditions of interstellar ice analogs subjected to UV irradiation, we used infrared spectroscopy. We were able to determine parameters such as

the degradation cross section (the probability that the chemical bonds of the iCOMs adsorbed on the grains are broken by the photons), and the average life of interstellar ices. To simulate the thermal desorption of photoprocessed iCOMS deposited on interstellar grains, we performed temperature programmed desorption (TPD) experiments. As described in Chapter 2, for this second type of experiment, we assembled a UHV chamber capable of reaching a pressure of $6.68 \cdot 10^{-10}$ mbar with feedthroughs for gas phase deposition from a pre-chamber where the mixtures were prepared controlling their partial pressures. The UHV chamber was interfaced with the Quadrupole mass spectrometer and with a closed-cycle helium cryocooler to simulate cryogenic temperatures. The assembly of the experimental apparatus, its calibration, and continuous implementation were an integral part of my Ph.D.

In Chapter 3, photoprocessing and thermal desorption studies of pure formamide ice and adsorbed on minerals are reported. Initially, ice samples of pure formamide were subjected to UV irradiation in situ and analyzed by FTIR spectroscopy. We observed that pure formamide ice showed no significant degradation even after 5 hours of UV irradiation, suggesting that formamide is highly stable to radiation under the conditions simulated in our experiment. However, pure solid-state formamide is unlikely to be found in space. It is more plausible that formamide is present in a mixture with other iCOMs as an icy mantle on dust grains. The same UV irradiation experiments were therefore repeated on samples of formamide adsorbed on different minerals. In the presence of the minerals, we found that the stability of the molecule to UV radiation is compromised. Our results show that both hydrated silicates such as antigorite and anhydrates such as forsterite offer formamide an order of magnitude greater level of protection from UV degradation than mineral oxides. When formamide was adsorbed by silicates, from the kinetic analysis of the degradation process, we evaluated a degradation cross section σ of 10^{-20} cm^2 for the bands due to NH_2 stretching, CH stretching, and CO stretching. On the other hand, when formamide was adsorbed by both TiO_2 and spinel, the degradation process took place with a cross section σ of 10^{-19} cm^2, i.e., an order of magnitude greater than the cross section found for the silicates. So, in the experimental conditions with which the photostability of formamide was studied, we found that silicates, which are ubiquitous in space, are more effective in protecting formamide from UV degradation than mineral oxides.

The formamide work did not concern only the study of its stability and survival on silicates and mineral oxides processed by UV irradiation, but also its thermal desorption through TPD experiments. Formamide was detected only in protostars hosting a hot corino (T>100 K). This evidence implies

that the presence in gas phase of formamide is closely linked to hot regions where thermal desorption is the process responsible for the sublimation of frozen mantles. Observations of formamide only in protostars hosting a hot corino show that formamide needs high temperatures to thermally desorb. We calculated a desorption temperature of 220 K in accordance with this evidence. By fitting the TPD curves of formamide using the Polanyi Wigner equation (equation 1.17), we calculated the binding energy of ∼7000 K (in Table 3.6, the energy values before and after UV irradiation are reported). These numbers are in agreement with the energies present in the literature obtained by both theoretical models and experimental works (e.g., Wakelam et al. 2017, Quénard et al. 2018, Chaabouni et al. 2017). However, our experiments show that these energies are greater when considering the adsorption on the grain surfaces. We reproduced the condensation, irradiation, and desorption experiments of formamide using a TiO_2 powder substrate. We found that in the presence of TiO_2, the formamide desorption occurred at a temperature 30 K higher than that found during bare cold finger experiments. In presence of TiO_2, the binding energy increased from $(7.5 \pm 0.7)\cdot10^3$ K to $(1.18 \pm 0.07)\cdot10^4$ K, as reported in the second column of Table 3.6. Therefore, in the chemical models of sublimation, it is essential to take into account the physisorption of the iCOMs on the grain surfaces and their interaction to correctly describe the desorption process, that is, to constrain the desorption temperatures and energies.

The binding energies are crucial parameters for astrochemical models that aim to reproduce the iCOMs observed in the gas phase, their abundances, and the evolution of chemistry. The presence of a molecule in the gas or solid phase depends on its binding energy. In general, in astrochemical models, a single binding energy value is inserted for a given molecule, either deduced through laboratory experiments or theoretical calculations. Recently, models of periodic surfaces of both crystalline and amorphous nature to mimic interstellar water ice mantles show that each molecule does not have a single binding energy value, but a distribution of values (Ferrero et al. 2020). These models show that, due to the complexity of the ice surfaces, each molecule can experience multiple binding energies values. Our TPD experiments experimentally demonstrated and quantified for the first time an increase in binding energy and a shift in desorption temperature. These results have important astrophysical implications, especially as regards the position and width of the snow lines in protoplanetary disks (radial distance from the central star where molecules are frozen in the disk). Considering interstellar ice surfaces as realistic as possible is critical to have reliable parameters to be included in astrochemical models. It is therefore mandatory to consider the presence of interstellar grains and the interactions between iCOMs and

grain surfaces.

In my second Ph.D. work, reported in Chapter 4, we performed TPD experiments of ice mixtures of acetaldehyde and acetonitrile from micrometric grains of silicate olivine. In general, most TPD studies of ices are performed from graphite and amorphous water ice surfaces. As far as we know, TPD experiments from grain surfaces are lacking in the literature.

We simulated for the first time the thermal desorption of samples of pure acetaldehyde, pure acetonitrile, and mixtures deposited on a 100 μm thick layer of olivine grains smaller than 5 μm. In the presence of grains, the TPD curves showed a first sharp desorption peak at around 100 K and 120 K for acetaldehyde and acetonitrile respectively (same desorption temperatures found in the absence of grains), followed by a second wider peak at higher temperature and with an intensity of about 40% compared to the first peak.

In protoplanetary disks, submicrometric interstellar grains begin to agglomerate into fluffy aggregates of hundreds of microns. Our work shows how layers of about 100 μm, resulting from the coagulation of micrometric-sized grains, could retain 40% of the deposited molecules up to temperatures of about 200 K. This implies that in protoplanetary regions with T$\geqslant$100 K, where we expect to no longer have acetonitrile and acetaldehyde in the solid phase, a fraction of these molecules can instead survive on the grains and can be desorbed at higher temperatures. The presence of porous grains is a precious process that can allow the delivery of molecules at high temperature regions, such as the innermost part of the disks with direct consequences on the presence of iCOMs in Earth-like planet forming region. Our studies, in fact, show that the presence of the grains can determine the broadening of the snow lines of water and molecules containing O and N, such as CH_3CN and CH_3COH. The snow lines should therefore be thought of as "snow regions", regions in which the presence of dust grains let the molecules survive in the solid phase at higher temperatures than those commonly obtained for pure ices.

In Chapter 5, the role of UV photons irradiation was investigated. Monolayers of pure acetaldehyde, pure acetonitrile, and mixture CH_3CN:CH_3COH (1:6) were deposited on micrometric grains of olivine at 17 K and subjected to UV irradiation in situ to study photolysis or the formation of complex molecules. These experiments show that by depositing CH_3CN:CH_3COH (1:6), the measured value of the ratio [HCO]/[CH_3CN] tripled as a result of the UV irradiation, confirming the acetaldehyde photodissociation. Thus, the presence of acetaldehyde ice photoprocessing may contribute to the high [HCO]/[CH_3CN] ratios observed in star-forming regions. Moreover, these experiments show that olivine is efficient in producing new and more complex species. The obtained mass spectra, in fact, showed new signals at high

m/z values compared to the spectra obtained during the desorption from the bare cold finger. Having ascertained the catalytic role of the mineral, through aldolic addition reactions in which the mineral acts as a catalyst and the radiation as an activator, we were able to explain some masses that we observed at high values of m/z (such as 126, 206, 81, 190 m/z). Although, as far as we know, there are no observations of such high molecular masses in space, we expect these signals to be present in star-forming regions where acetaldehyde and acetonitrile have been observed and where UV radiation and silicates are involved in an active role.

The Ph.D. project led to the publication of two papers as first author ("Photoprocessing of formamide ice: route to prebiotic chemistry in space", Corazzi et al. 2020, and "Thermal desorption of astrophysical relevant ice mixtures of acetaldehyde and acetonitrile from olivine dust", Corazzi et al. 2021) and a third paper as first name recently submitted to the Astrophysical Journal entitled "Photo-processing and thermal desorption of acetaldehyde and acetonitrile ices mixed with olivine".

These results hopefully will help to understand the chemistry that goes along with the formation process of stars and planets. Laboratory experiments in synergy with astrochemical models are fundamental for interpreting the ever-increasing number of iCOMs and their observed abundances along the formation process of a Sun-like star. Studies on the photoprocessing of ice samples by FTIR spectroscopy show the evolution and degradation of crucial prebiotic molecules in the presence of grains. TPD studies, in addition to providing fundamental parameters for astrochemical models such as binding energies, provide us information on how the molecules fragmented. During the formamide TPD experiments, we found relationships between the abundance of NH_2 and the abundance of HCO and CH_2NO of $[NH_2]/[HCO]$ $\sim$4. So, the molecular fragments observed in the gas phase can be used to indirectly measure the presence of formamide in the solid phase. Going forward, TPD experiments from olivine micrometer grains have shown how the interactions between the molecules and the surface of grains can modify the shape of the TPD curve, that is, can drive and influence the release and therefore the presence of iCOMs in the gaseous phase in environments where the thermal heating plays a dominant role, providing information on the fraction of molecules released at different temperatures with direct consequences in protoplanetary disks.

These kinds of studies and experiments are increasingly important in view of the exciting new discoveries of organic molecules that we expect from the next launch of the James Webb Space Telescope (JWST or Webb), which will complement and extend the discoveries of the Hubble Space Telescope.

It will study every phase of the history of our Universe, the formation of solar systems capable of supporting life on planets such as Earth, and the evolution of our Solar System. It will be able to visualize disks around young stars which may indicate the start of planetary systems, and, particularly important from our point of view, it will be able to study organic molecules that are important for the development of life. The scientific community will also await new discoveries regarding the search for water and organic molecules essential for life as we know it from the launch of SPHEREx expected on June 17, 2024. SPHEREx is a future near-infrared space observatory that will carry out a survey across the sky to measure the near-infrared spectra of some 450 million galaxies. SOFIA, the joint program between NASA and the German Aerospace Center (DLR), shows how topics of astrobiology and astrochemistry are increasing of interest to the scientific world. SOFIA will be able to carry out observations on board an aircraft. It is composed of a Boeing 747SP modified to house a 2.5 meter gyrostabilized telescope capable of making observations impossible even for the largest terrestrial telescopes on the highest peaks. Many of SOFIA's target observations are directly relevant to the astrobiology program, such as studying the formation of new solar systems and identifying complex molecules. Laboratory experiments on interstellar analogs of iCOMs and grains will continue in synergy with astrochemical models and observations with the confidence that exciting new discoveries will come.

Acknowledgements

I would like to express my gratitude to my main advisor, Prof. John Robert Brucato for having always believed in me and accompanying me in this experience. I am grateful to him for the opportunity received, for his help and advice. I would also like to thank Dr. Davide Fedele who assisted and guided me in this project.

Bibliography

Abou Mrad, N., F. Duvernay, T. Chiavassa, and G. Danger (2016). In: *MNRAS* 458, Issue 2, pp. 1234–1241.

Ábrahám, P., A. Kóspál, L. Chen, and A. Carmona (2020). In: *Proceedings of the International Astronomical Union* 345.

Agarwal, V. K., W. Schutte, J. M. Greenberg, J. P. Ferris, R. Briggs, S. Connor, C. P.E. M. van de Bult, and F. Baas (1985). In: *Origins of Life and Evolution of the Biosphere* 16, Issue 1, pp. 21–40.

Aikawa, Y., S. M. Miyama, T. Nakano, and T. Umebayashi (1996). In: *ApJ* 467, p. 684.

Aikawa, Y. and E. Herbst (1998). In: *A&A* 351, pp. 233–246.

— (1999). In: *A&A* 351, pp. 233–246.

Andrade, D. P. P., M. L. M. Rocco, and H. M Boechat-Roberty (2010). In: *MNRAS* 409, Issue 3, pp. 1289–1296.

Andron, I., P. Gratier, L. Majumdar, T. H. G. Vidal, A. Coutens, J. Loison, and V. Wakelam (2018). In: *MNRAS* 481, Issue 4.

Ángel Satorre Aznar, M. and J. Leliwa-Kopystynki (2010). In: *38th COSPAR Scientific Assembly.*

Arce, H. G., J. Santiago-García, J. K. Jørgensen, M. Tafalla, and R. Bachiller (2008). In: *ApJL* 681, Issue 1.

Attard, G. and C. Barnes (1998). "Surfaces". In: *Oxford chemistry primers* 59.1, ALL–ALL.

Bachiller, R. and M. Pérez Gutiérrez (1997). In: *ApJ* 487, Issue 1, pp. L93–L96.

Bacmann, A., V. Taquet, A. Faure, C. Kahane, and C. Ceccarelli (2012). In: *A&A* 541, id.L12.

Bar-Nun, A., I. Kleinfeld, and E. Kochavi (1988). In: *Physical Review B: Solid State* 38, Issue 11.

Baratta, G. A., D. Chaput, H. Cottin, L. Fernandez Cascales, M. E. Palumbo, and G. Strazzulla (2015). In: *Planetary Space Science* 118, pp. 211–220.

Basalgéte, R., R. Dupuy, G. Féraud, C. Romanzin, L. Philippe, X. Michaut, J. Michoud, L. Amiaud, A. Lafosse, J. H. Fillion, and M. Bertin (2021). In: *A&A* 647, id.A35.

Belloche, A., A. J. Maury, S. Maret, S. Anderl, A. Bacmann, P. André, S. Bontemps, S. Cabrit, C. Codella, M. Gaudel, F. Gueth, C. Lefévre, B. Lefloch, L. Podio, and L. Testi (2020). In: *A&A* 635, id.A198.

Bergantini, A., S. Pilling, H. Rothard, P. Boduch, and D. P. P. Andrade (2014). In: *MNRAS* 437, Issue 3, pp. 2720–2727.

Bergner, J. B., V. G. Guzman, K. I. Öberg, R. A. Loomis, and J. Pegues (2018). In: *ApJ* 857, Issue 1.

Bernstein, M. P., S. A. Sandford, L. J. Allamandola, S. Chang, and M. A. Scharberg (1995). In: *ApJ* 454.

Bertin, M., C. Romanzin, M. Doronin, L. Philippe, P. Jeseck, N. Ligterink, H. Linnartz, X. Michaut, and J. Fillion (2016). In: 817, Issue 2, article id. L12.

Beuther, H., C. Kramer, B. Deiss, and J. Stutzki (2000). In: *A&A* 362, pp. 1109–1121.

Bianchi, E., C. Codella, C. Ceccarelli, F. Vazart, R. Bachiller, N. Balucani, M. Bouvier, M. De Simone, J. Enrique-Romero, C. Kahane, B. Lefloch, A. Lopez-Sepulcre, J. Ospina-Zamudio, L. Podio, and V. Taquet (2019). In: *MNRAS* 483, Issue 2.

Biver, N. and D. Bockelee-Morvan (2019). In: *ACS Earth and Space Chemistry* 3, issue 8.

BjäRnborg, K. and B. Schmitz (2013). In: *Meteoritics and Planetary Science* 48, pp. 180–194.

Blake, G. A., E. C. Sutton, C. R. Masson, and T. G. Phillips (1987). In: *ApJ* 315.

Bockelée-Morvan, D., D. C. Lis, J. E. Wink, D. Despois, J. Crovisier, R. Bachiller, D. J. Benford, N. Biver, P. Colom, J. K. Davies, E. Gerard, B. Germain, M. Houde, D. Mehringer, R. Moreno, G. Paubert, T. G. Phillips, and H. Rauer (2000). In: *A&A* 353, pp. 1101–1114.

Bockelée-Morvan, D., G. Rinaldi, S. Erard, C. Leyrat, F. Capaccioni, P. Drossart, G. Filacchione, A. Migliorini, E. Quirico, S. Mottola, G. Tozzi, G. Arnold, N. Biver, M. Combes, J. Crovisier, A. Longobardo, M. Blecka, and M. T. Capria (2017). In: *MNRAS* 469.

Boekel, R. van, M. Min, C. Leinert, L. B.F. M. Waters, A. Richichi, O. Chesneau, C. Dominik, W. Jaffe, A. Dutrey, U. Graser, T. Henning, J. de Jong, R. Köhler, A. de Koter, B. Lopez, F. Malbet, S. Morel, G. Paresce F.and Perrin, and T. Preibisch (2004). In: *Nature* 432, Issue 7016, pp. 479–482.

Bogelund, E. G., B. A. McGuire, M. R. Hogerheijde, E. F. van Dishoeck, and N. F. W. Ligterink (2019). In: *A&A* 624, id.A82.

Bohren, C. F., D. R. Huffman, and Z. Kam (1983). In: *Nature* 306, Issue 5943, p. 625.

Boruah, M. J., A. Gogoi, B. C. Nath, and G. A. Ahmed (2017). In: *J. Quantitative Spectroscopy and Rad. Trasfer* 196.

Brownlee, D. E. and S. M. Team (2006). In: *Bullettin AAS* 38.

Brucato, J. R., G. A. Baratta, and G. Strazzulla (2006). In: *A&A* 455, pp. 395–399.

Bulak, M., D. M. Paardekooper, G. Fedoseev, and H. Linnartz (2020). In: *A&A* 636, id.A32, p. 13.

Caplan, C. E., G. R. Huss, H. A. Ishii, J. P. Bradley, B. Schmitz, and K. Nagashima (2017). In: *80th Annual Meeting of the meteoritical society* held july 23-28 2017 in Santa Fe, New Mexico.

Caselli, P. and C. Ceccarelli (2012). In: *A&A* Review 20.

Cazaux, S., A. G.G. M. Tielens, C. Ceccarelli, A. Castets, V. Wakelam, E. Caux, B. Parise, and D. Teyssier (2003). In: *ApJ* 593, Issue 1, pp. L51–L55.

Ceccarelli, C. (2004). In: *Star Formation in the Interstellar Medium: In Honor of David Hollenbach, Chris McKee and Frank Shu, ASP Conference Proceedings* 323, Edited by D. Johnstone, F.C. Adams, D.N.C. Lin, D.A. Neufeld, and E.C. Ostriker. San Francisco: Astronomical Society of the Pacific.

Ceccarelli, C., P. Caselli, E. Herbst, A. G.G. M. Tielens, and E. Caux (2007). In: *Protostars and Planets V* University of Arizona Press, Tucson, pp. 47–62.

Cesaroni, R., A. Samnchez-Monge, M. T. Beltran, L. T. Johnston K. G.and Maud, L. Moscadelli, J. C. Mottram, A. Ahmadi, V. Allen, H. Beuther, T. Csengeri, S. Etoka, G. A. Fuller, and D. Galli (2017). In: *A&A* 602.

Chaabouni, H., S. Diana, T. Nguyen, and F. Dulieu (2017). In: *Astronomy and Astrophysics manuscript*.

Charnley, S. B., M. E. Kress, A. G.G. M. Tielens, and T. J. Millar (1995). In: *ApJ* 448.

Chen, P. S., X. H. Wang, and J. H. He (2000). In: *Astrophysics and Space Science* 271.

Chuang, K. J., G. Fedoseev, D. Qasim, S. Ioppolo, C. Jager, T. Henning, M. E. Palumbo, E. F. van Dishoeck, and H. Linnartz (2020). In: *A&A* 635, id.A199.

Ciaravella, A., G. Muñoz Caro, A. Jiménez Escobar, C. Cecchi-Pestellini, S. Giarrusso, M. Barbera, and A. Collura (2010). In: *ApJL* 722, Issue 1, pp. L45–L48.

Ciaravella, A., G. M. Muñoz Caro, A. Jiménez-Escobar, C. Cecchi-Pestellini, L. Hsiao, C. Huang, and Y. Chen (2020). In: *Proceedings of the National Academy of Sciences* 117, issue 28.

Ciesla, F. J. and J. N. Cuzzi (2006). In: *Icarus* 181, Issue 1, pp. 178–204.

Cieza, L. A., S. Casassus, J. Tobin, S. P. Bos, J. P. Williams, S. Perez, Z. Zhu, C. Caceres, H. Canovas, M. M. Dunham, A. Hales, J. L. Prieto, D. A. Principe, M. R. Schreiber, D. Ruiz-Rodriguez, and A. Zurlo (2016). In: *Nature* 535, Issue 7611, pp. 258–261.

Codella, C., M. Benedettini, M. T. Beltrán, F. Gueth, S. Viti, R. Bachiller, M. Tafalla, S. Cabrit, A. Fuente, and B. Lefloch (2009). In: *A&A* 507, Issue 2, pp. L25–L28.

Codella, C., B. Lefloch, C. Ceccarelli, J. Cernicharo, E. Caux, A. Lorenzani, S. Viti, P. Hily-Blant, B. Parise, S. Maret, B. Nisini, P. Caselli, S. Cabrit, L. Pagani, M. Benedettini, A. Boogert, F. Gueth, G. Melnick, D. Neufeld, S. Pacheco, M. Salez, K. Schuster, A. Bacmann, A. Baudry, T. Bell, E. A. Bergin, G. Blake, S. Bottinelli, A. Castets, C. Comito, A. Coutens, N. Crimier, C. Dominik, K. Demyk, P. Encrenaz, E. Falgarone, A. Fuente, M. Gerin, P. Goldsmith, F. Helmich, P. Hennebelle, T. Henning, E. Herbst, T. Jacq, C. Kahane, M. Kama, A. Klotz, W. Langer, D. Lis, S. Lord, J. Pearson, T. Phillips, P. Saraceno, P. Schilke, X. Tielens, F. van der Tak, M. van der Wiel, C. Vastel, V. Wakelam, A. Walters, F. Wyrowski, H. Yorke, C. Borys, Y. Delorme, C. Kramer, B. Larsson, I. Mehdi, V. Ossenkopf, and J. Stutzki (2010). In: *A&A* 518, id.L112.

Codella, C., F. Fontani, C. Ceccarelli, L. Podio, S. Viti, R. Bachiller, M. Benedettini, and B. Lefloch (2015). In: *MNRAS* 449, pp. L11–L15.

Codella, C., C. Ceccarelli, S. Cabrit, F. Gueth, L. Podio, R. Bachiller, F. Fontani, A. Gusdorf, B. Lefloch, S. Leurini, and M. Tafalla (2016). In: *A&A* 586, id.L3.

Codella, C., C. Ceccarelli, P. Caselli, N. Balucani, V. Barone, F. Fontani, B. Lefloch, L. Podio, S. Viti, S. Feng, R. Bachiller, E. Bianchi, F. Dulieu, I. Jiménez-Serra, J. Holdship, R. Neri, J. E. Pineda, A. Pon, I. Sims, and S. Spezzano (2017). In: *A&A* 605, id.L3.

Cohen, M. and F. C. Witteborn (1985). In: *ApJ* 294, pp. 345–356.

Collings, M. P., M. A. Anderson, R. Chen, J. W. Dever, S. Viti, D. A. Williams, and M. R. S. MCCoustra (2004). In: *MNRAS* 354, pp. 1133–1140.

Corazzi, M. A., D. Fedele, G. Poggiali, and J. R. Brucato (2020). In: *A&A* 636, id. A63.

Corazzi, M. A., J. R. Brucato, G. Poggiali, L. Podio, D. Fedele, and C. Codella (2021). In: *ApJ* 913, Issue 2, id.128.

Cordiner, M. A., M. Y. Palmer, C. A. Nixon, P. G. J. Irwin, N. A. Teanby, S. B. Charnley, M. J. Mumma, Z. Kisiel, J. Serigano, Y. J. Kuan, Y. L. Chuang, and K. S. Wang (2015). In: *Astrophysical journal letters* 800, Issue 1.

D'Hendecourt, L. B., L. J. Allamandola, R. J. A. Grim, and J. M. Greenberg (1986). In: *A&A* 158, pp. 119–134.

Duley, W. W. and D. A. Williams (1984). In: *Nature* 311.

Dupuy, R., M. Bertin, G. Féraud, M. Hassenfratz, X. Michaut, T. Putaud, L. Philippe, P. Jeseck, M. Angelucci, R. Cimino, V. Baglin, C. Romanzin, and J. H. Fillion (2018). In: *Nature* 2, pp. 796–801.

Enrique-Romero, J., A. Rimola, C. Ceccarelli, and N. Balucani (2016). In: *MNRAS* 459, Issue 1.

Favre, C., D. Fedele, D. Semenov, S. Parfenov, C. Codella, C. Ceccarelli, E. A. Bergin, E. Chapillon, L. Testi, F. Hersant, B. Lefloch, F. Fontani, G. A. Blake, L. I. Cleeves, C. Qi, K. R. Schwarz, and V. Taquet (2018). In: *ApJL* 862, Issue 1, article id. L2.

Ferrero, S., L. Zamirri, C. Ceccarelli, A. Witzel, A. Rimola, and P. Ugliengo (2020). In: *ApJ* 904, Issue 1, id.11.

Flores, C., G. Duchêne, S. Wolff, M. Villenave, K. Stapelfeldt, J. P. Williams, C. Pinte, D. Padgett, M. S. Connelley, G. van der Plas, F. Ménard, and M. D. Perrin (2021). In: *AJ* 161, Issue 5, id.239.

Fornaro, T., J. R. Brucato, E. Pace, M. Cestelli Guidi, S. Branciamore, and A. Pucci (2013). In: *Icarus* 226, pp. 1068–1085.

Fujiyoshi, T., C. M. Wright, and T. J. T. Moore (2015). In: *MNRAS* 451, pp. 3371–3384.

Garrod, R. T. and E. Herbst (2006). In: *A&A* 457, Issue 3.

Garrod, R. T., V. Wakelam, and E. Herbst (2007). In: *A&A* 467, Issue 3, pp. 1103–1115.

Gerakines, P. A., M. H. Moore, and R. L. Hudson (2004). In: *Icarus* 170, Issue 1, pp. 202–213.

Gibb, E. L., D. C. B. Whittet, W. A. Schutte, A. C. A. Boogert, J. E. Chiar, P. Ehrenfreund, P. A. Gerakines, J. V. Keane, A. G.G. M. Tielens, E. F. van Dishoeck, and O. Kerkhof (2000). In: *ApJ* 536, Issue 1, pp. 347–356.

Goesmann, F., H. Rosenbauer, J. H. Bredehöft, M. Cabane, P. Ehrenfreund, T. Gautier, C. Giri, H. Krüger, L. Le Roy, A. J. MacDermott, S. McKenna-Lawlor, U. J. Meierhenrich, G. M. M. Caro, F. Raulin, R. Roll, A. Steele, H. Steininger, R. Sternberg, C. Szopa, W. Thiemann, and U. S. (2015). In: *Science* 349, Issue 6247.

Griffiths, P. R. and J. A. de Haseth (2007). *Fourier Transform Infrared Spectrometry, Second Edition*. John Wiley and Sons, Inc. ISBN: 9780470106310.

Guzman, A. E., V. V. Guzman, G. Garay, L. Bronfman, and F. Hechenleitner (2018). In: *ApJSupplement Series* 236, Issue 2, article id. 45.

Hagen, W., L. J. Allamandola, and J. M. Greenberg (1979). In: *Astrophysics and Space Science* 65, Issue 1, pp. 215–240.

Halfen, D. T., V. Ilyushin, and L. M. Ziurys (2011). In: *ApJ* 743.

Hama, T., N. Watanabe, A. Kouchi, and M. Yokoyama (2011). In: *ApJL* 738, Issue 1, article id. L15.

Hartmann, L. (2009). *Accretion Processes in Star Formation, Second Edition*. Cambridge University Press. ISBN: 9780511552090.

Hassel, G. (2004). In: *American Astronomical Society Meeting Abstracts* 204, id.24.02 Bulletin of the American Astronomical Society, Vol. 36.

Heays, A. N., A. D. Bosman, and E. F. van Dishoeck (2017). In: *A&A* 602, id.A105, 62 pp.

Henning, T. (2010). In: *ARA&A* 48, pp. 21–46.

Herbig, G. H. and R. W. Goodrich (1986). In: *ApJ* 309, p. 294.

Hoff, M. L. R. van 't, J. J. Tobin, L. Trapman, D. Harsono, P. D. Sheehan, W. J. Fischer, S. T. Megeath, and E. F. van Dishoeck (2018). In: *ApJL* 864, Issue 1, article id. L23.

Honda, M., H. Kataza, Y. K. Okamoto, T. Miyata, T. Yamashita, S. Sako, S. Takubo, and T. Onaka (2003). In: *ApJ* 585, Issue 1.

Hosein, G., A. Muhammad, S. Suriati, L. Bhajan, and U. Yoshimitsu (2017). In: *Journal of Molecular Liquids* 242, pp. 395–403.

Huber, F., J. Berwanger, S. Polesya, S. Mankovsky, H. Ebert, and F. J. Giessibl (2019). In: *Science* 366, Issue 6462, pp. 235–238.

Hudson, R. L. and B. Donn (1991). In: *Icarus* 94, Issue 2, pp. 326–332.

Iino, T., H. Sagawa, and T. Tsukagoshi (2020). In: *ApJ* 890, Issue 2.

Imai, M., N. Sakai, Y. Oya, A. López-Sepulcre, Y. Watanabe, C. Ceccarelli, B. Lefloch, E. Caux, C. Vastel, C. Kahane, T. Sakai, T. Hirota, Y. Aikawa, and S. Yamamoto (2016). In: 830, Issue 2, article id. L37.

Jaeger, C., F. J. Molster, J. Dorschner, T. Henning, H. Mutschke, and L. B.F. M. Waters (1998). In: *A&A* 339, pp. 904–916.

Jauhari, S. (2008). In: *American Astronomical Society/Division for Planetary Sciences Meeting Abstracts* 40, p. 485.

Kahane, C., C. Ceccarelli, A. Faure, and E. Caux (2013). In: *ApJL* 763, Issue 2, article id. L38.

Kanuchová, Z., R. G. Urso, G. A. Baratta, J. R. Brucato, M. E. Palumbo, and G. Strazzulla (2016). In: *A&A* 585, id.A155.

Kempen, T. A. van, E. F. van Dishoeck, R. Güsten, L. E. Kristensen, P. Schilke, M. R. Hogerheijde, W. Boland, K. M. Menten, and F. Wyrowski (2009). In: *A&A* 507, Issue 3, pp. 1425–1442.

Kemper, C., M. Spaans, D. J. Jansen, M. R. Hogerheijde, E. F. van Dishoeck, and A. G.G. M. Tielens (1999). In: *ApJ* 515, Issue 2, pp. 649–656.

Kloprogge, J. (2018). In: *Spectroscopic Methods in the Study of Kaolin Minerals and Their Modifications* Springer Mineralogy. Springer, Cham.

Kouchi, A., H. Nakano, Y. Kimura, and C. Kaito (2005). In: *ApJ* 626, Issue 2, pp. L129–L132.

Lai, S. C. S., S. E. F. Kleyn, V. Rosca, and M. T. M. Koper (2008). In: *Journal of Chemical Physics* 112, 48.

Lamberts, T., M. N. Markmeyer, F. J. Kolb, and J. Kastner (2019). In: *ACS Earth and Space Chemistry* 3, issue 6.

Langmuir, I. (1918). In: *J. Am. Chem. Soc.* 40.

Le Gal, R., M. T. Brady, K. I. Oberg, E. Roueff, and F. Le Petit (2019). In: *ApJ* 886, Issue 2.

Lee, C., Z. Li, P. T. P. Ho, N. Hirano, Q. Zhang, and H. Shang (2017). In: *ApJ* 843, Issue 1, article id. 27.

Lee, J., S. Lee, G. Baek, Y. Aikawa, L. Cieza, S. Yoon, G. Herczeg, D. Johnstone, and S. Casassus (2019). In: *Nature Astronomy* 3.

Lefloch, B., C. Ceccarelli, C. Codella, C. Favre, L. Podio, C. Vastel, S. Viti, and R. Bachiller (2017). In: *MNRAS* 469, Issue 1, pp. L73–L77.

Lennard-Jones, J. (1971). In: *Transactions of the Faraday Society* 67.

Lisse, C. M., J. VanCleve, A. C. Adams, M. F. A'Hearn, Y. R. Fernández, T. L. Farnham, L. Armus, C. J. Grillmair, J. Ingalls, M. J. S. Belton, O. Groussin, L. A. McFadden, K. J. Meech, P. H. Schultz, B. C. Clark, L. M. Feaga, and J. M. Sunshine (2006). In: *Science* 313, Issue 5787, pp. 635–640.

Loomis, R. A., L. I. Cleeves, K. I. Öberg, Y. Aikawa, J. Bergner, K. Furuya, V. V. Guzman, and C. Walsh (2018). In: *ApJ* 859, Issue 2.

López-Sepulcre, A., A. A. Jaber, E. Mendoza, B. Lefloch, C. Ceccarelli, C. Vastel, R. Bachiller, J. Cernicharo, C. Codella, C. Kahane, M. Kama, and M. Tafalla (2015). In: *MNRAS* 449, Issue 3, pp. 2438–2458.

López-Sepulcre, A., N. Balucani, C. Ceccarelli, C. Codella, F. Dulieu, and P. Theulé (2019). In: *ACS Earth and Space Chemistry* 3, issue 10, pp. 2122–2137.

Mahata, A., A. S. Nair, and B. Pathak (2019). In: *Catalysis Science and Technology* 9 (18), pp. 4835–4863.

Marcelino, N., M. Gerin, J. Cernicharo, A. Fuente, H. A. Wootten, E. Chapillon, J. Pety, D. C. Lis, E. Roueff, B. Commerçon, and A. Ciardi (2018). In: *A&A* 620, id.A80.

Martín-Doménech, R., K. I. Oberg, and M. Rajappan (2020). In: *ApJ* 894, Issue 2.

Materese, C. K., M. Nuevo, and S. A. Sandford (2011). In: *The Molecular Universe, Proceedings* 280th Symposium of the International Astronomical Union held in Toledo, id.249.

Mc Naughton, D., C. J. Evans, S. Lane, and C. J. Nielsen (1999). In: *Journal of Molecular Spectroscopy* 193, pp. 104–117.

Meinert, C., I. Myrgorodska, P. de Marcellus, T. Buhse, L. Nahon, S. V. Hoffmann, L. L. S. d'Hendecourt, and U. J. Meierhenrich (2016). In: *Science* 352, Issue 6282, pp. 208–212.

Mendoza, E., G. C. Almeida, D. P. P. Andrade, H. Luna, W. Wolff, M. L. M. Rocco, and H. M. Boechat-Roberty (2013). In: *MNRAS* 433, Issue 4, pp. 3440–3452.

Mennella, V. (2015). In: *Highlights of Astronomy* 16, pp. 715–716.

Messenger, S., L. P. Keller, and D. S. Lauretta (2005). In: *Science* 309, pp. 737–741.

Min, M., J. W. Hovenier, A. de Koter, L. B.F. M. Waters, and C. Dominik (2005). In: *Icarus* 179, Issue 1.

Mumma, M. J. and S. B. Charnley (2011). In: *ARA&A* 49, issue 1, pp. 471–524.

Muñoz Caro, G. M., R. Ruiterkamp, W. A. Schutte, J. M. Greenberg, and V. Mennella (2001). In: *A&A* 367, pp. 347–354.

Muñoz Caro, G. M. and W. A. Schutte (2003). In: *A&A* 412, p.121–132.

Muñoz Caro, G. M., U. Meierhenrich, W. A. Schutte, W. H. P. Thiemann, and J. M. Greenberg (2004). In: *A&A* 413, pp. 209–216.

Myers, P. C. and P. J. Benson (1983). In: *ApJ* 266, pp. 309–320.

Nagy, Z., F. F. S. van der Tak, G. A. Fuller, and R. Plume (2015). In: *A&A* 577, id.A127.

Najita, J., E. A. Bergin, and J. N. Ullom (2001). In: *ApJ* 561, Issue 2, pp. 880–889.

Natta, A., L. Testi, N. Calvet, T. Henning, R. Waters, and D. Wilner (2007). In: *Protostars and Planets V, B. Reipurth, D. Jewitt, and K. Keil (eds.), University of Arizona Press, Tucson* 951, pp. 767–781.

Navarro-Almaida, D., R. Le Gal, A. Fuente, P. Rivière-Marichalar, V. Wakelam, S. Cazaux, P. Caselli, J. C. Laas, T. Alonso-Albi, J. C. Loison, M. Gerin, C. Kramer, E. Roueff, R. Bachiller, B. Commercon, R. Friesen, S. García-Burillo, J. R. Goicoechea, B. M. Giuliano, I. Jiménez-Serra, J. M. Kirk, V. Lattanzi, J. Malinen, N. Marcelino, R. Martín-Doménech, G. M. Muñoz Caro, J. Pineda, B. Tercero, S. P. Treviño Morales, O. Roncero, A. Hacar, M. Tafalla, and D. Ward-Thompson (2020). In: *A&A* 637, id.A39.

Navarro-Gonzalez, R., L. Montoya, W. Davis, and C. McKay (2008). In: *COSPAR Scientific Assembly* 37th, held in Montréal, Canada, p. 2190.

Nguyen, A. N., L. R. Nittler, C. M.O. D. Alexander, and P. Hoppe (2018). In: *Geoch. Cosmochimica Acta* 221, pp. 162–181.

Nguyen, T., I. Fourré, C. Favre, C. Barois, E. Congiu, S. Baouche, J. C. Guillemin, Y. Ellinger, and F. Dulieu (2019). In: *A&A* 628, id.A15.

Nguyen, T. T. (1986). In: *Division of Soils, Private Mail Bag No.2* Glen Osmond, South Australia.

Nittler, L. R., C. M. O. Alexander, R. Gallino, P. Hoppe, A. N. Nguyen, F. J. Stadermann, and E. K. Zinner (2008). In: *ApJ* 682, pp. 1450–1478.

Nummelin A. ; Bergman, P., A. Hjalmarson, P. Friberg, W. M. Irvine, T. J. Millar, M. Ohishi, and S. Saito (1998). In: *ApJS* 117, pp. 427–529.

Öberg, K. I., R. T. Garrod, E. F. Van Dishoeck, and H. Linnartz (2009). In: *A&A* 504, pp. 891–913.

Öberg, K. I., V. V. Guzman, K. Furuya, C. Qi, Y. Aikawa, S. M. Andrews, R. Loomis, and D. J. Wilner (2015). In: *Nature* 520, Issue 7546.

O'Connor, J., B. Sexton, and R. S. Smart (2013). *Surface Analysis Methods in Materials Science*. Springer, Second Edition. ISBN: 978-3-662-05227-3.

Ootsubo, T., H. Kawakita, Y. Shinnaka, J. Watanabe, and M. Honda (2020). In: *Icarus* 338.

Oparin, A. I. (1938). In: *The Origin of life* New Yourk.

Oya, Y., N. Sakai, Y. Watanabe, A. E. Higuchi, T. Hirota, A. López-Sepulcre, T. Sakai, Y. Aikawa, C. Ceccarelli, B. Lefloch, E. Caux, C. Vastel, C. Kahane, and S. Yamamoto (2017). In: *ApJ* 837, Issue 2, article id. 174.

Palumbo, M. E. and G. Strazulla (1993). In: *A&A* 269.

Panayotov, D. A, S. Burrows, M. Mihaylov, K. Hadjiivanov, B. M. Tissue, and J. R. Morris (2010). In: *Langmuir ACS Journal of Surfaces and Colloids* 26, pp. 8106–8112.

Picazzio, E., I. V. Lukyanyk, O. V. Ivanova, E. Zubko, O. Cavichia, G. Videen, and S. M. Andrievsky (2019). In: *Icarus* 319.

Podio, L., C. Codella, B. Lefloch, N. Balucani, C. Ceccarelli, R. Bachiller, M. Benedettini, J. Cernicharo, N. Faginas-Lago, F. Fontani, A. Gusdorf, and M. Rosi (2017). In: *MNRAS* 470, Issue 1, pp. L16–L20.

Podio, L., A. Garufi, C. Codella, D. Fedele, E. Bianchi, F. Bacciotti, C. Ceccarelli, C. Favre, S. Mercimek, K. Rygl, and L. Testi (2020). In: *A&A* 642, id.L7.

Poteet, C. A., S. T. Megeath, D. M. Watson, N. Calvet, I. S. Remming, M. K. McClure, B. A. Sargent, W. J. Fischer, E. Furlan, L. E. Allen, J. E. Bjorkman, L. Hartmann, J. Muzerolle, J. J. Tobin, and B Ali (2011). In: *ApJ* 733.

Przygodda, F., R. van Boekel, P. Ábrahám, S. Y. Melnikov, L. B.F. M. Waters, and C. Leinert (2003). In: *A&A* 412, pp. L43–L46.

Quénard, D., J. D. Ilee, I. Jiménez-Serra, D. H. Forgan, C. Hall, and K. Rice (2018). In: *ApJ* 868, Issue 1, article id. 9.

Ranke, W. (2005). In: *Lecture. Fritz-Haber Institute.*

Redhead, P. A. (1962). In: *Vacuum* 12, issue 4, pp. 203–211.

Rubin, M., K. Altwegg, H. Balsiger, J. Berthelier, M. R. Combi, J. De Keyser, M. Drozdovskaya, B. Fiethe, S. A. Fuselier, S. Gasc, T. I. Gombosi, N. Hänni, K. C. Hansen, U. Mall, H. Rème, I. R.H. G. Schroeder, M. Schuhmann, T. Sémon, J. H. Waite, and S. F. Wampfler (2019). In: *MNRAS* 489, Issue 1, pp. 594–607.

Rubinson, K. A., J. F. Rubinson, and M. Taddia (2002). *Chimica analitica strumentale.* Zanichelli. ISBN: 8808089592.

Sakai, N. and S. Yamamoto (2013). In: *Chemical Reviews* 113, pp. 8981–9015.

Sandford, S. A. and L. J. Allamandola (1988). In: *Icarus* 76, Issue 2, pp. 201–224.

Savage, C. and L. M. Ziurys (2004). In: *ApJ* 616 Issue 2, pp. 966–975.

Schroeder, S. L. M. and M. Gottfried (2002). In: *Advanced Physical Chemistry Laboratory FU Berlin* Temperature-Programmed Desorption (TPD). Thermal Desorption Spectroscopy (TDS).

Shi, J., G. A. Grieves, and T. M. Orlando (2015). In: *ApJ* 804, Issue 1.

Shinnaka, Y., T. Ootsubo, H. Kawakita, M. Yamaguchi, M. Honda, and J. Watanabe (2018). In: *AJ* 156, Issue 5, article id. 242.

Simons, M. A. J., T. Lamberts, and H. M. Cuppen (2020). In: *A&A* 634, id.A52.

Sivaraman, B., B. N. Raja Sekhar, B. G. Nair, V. Hatode, and N. J. Mason (2013). In: *Spectrochimica Acta Part: Molecular and Biomolecular Spectroscopy.*

Smith, R. G., K. Sellgren, and T. Y. Brooke (1993). In: *MNRAS* 263, pp. 749–766.

Soma, T., N. Sakai, Y. Watanabe, and S. Yamamoto (2015). In: *ApJ* 802, Issue 2, article id. 74.

Spaans, M., M. R. Hogerheijde, L. G. Mundy, and E. F. van Dishoeck (1995). In: *ApJ* 455, p. L167.

Taha, A. S., L. Labadie, E. Pantin, A. Matter, C. Alvarez, P. Esquej, R. Grellmann, R. Rebolo, C. Telesco, and S. Wolf (2018). In: *A&A* 612, id.A15.

Taniguchi, K., A. E. Guzman, L. Majumdar, M. Saito, and K. Tokuda (2020). In: *ApJ* 898.

Taquet, V., A. López-Sepulcre, C. Ceccarelli, R. Neri, C. Kahane, and S. B. Charnley (2015). In: *ApJ* 804, Issue 2, article id. 81.

Testi, L., T. Birnstiel, L. Ricci, S. Andrews, J. Blum, J. Carpenter, C. Dominik, A. Isella, A. Natta, J. P. Williams, and D. J. Wilner (2014). In:

Protostars and Planets VI, Henrik Beuther, Ralf S. Klessen, Cornelis P. Dullemond, and Thomas Henning (eds.), University of Arizona Press, Tucson 914, pp. 339–361.

Thelen, A. E., C. A. Nixon, N. J. Chanover, M. A. Cordiner, E. M. Molter, N. A. Teanby, P. G. J. Irwin, J. Serigano, and S. B. Charnley (2019). In: *Icarus* 319.

Turner, B. E. (1991). In: *ApJS* 76, pp. 617–686.

Urso, R. G., C. Scirè, G. A. Baratta, J. R. Brucato, G. Compagnini, Z. Kanuchová, M. E. Palumbo, and G. Strazzulla (2017). In: *Phys. Chem. Chem. Phys.* 19, issue 32, pp. 21759–21768.

Val-Borro, M. de, S. N. Milam, M. A. Cordiner, S. B. Charnley, I. M. Coulson, A. J. Remijan, and G. L. Villanueva (2018). In: *MNRAS* 474, Issue 1.

Vastel, C., C. Ceccarelli, B. Lefloch, and R. Bachiller (2014). In: *ApJL* 795, Issue 1, article id. L2.

Ventura, G. and L. Risegari (2008). In: *The art of cryogenics. Low-temperature experimental techniques* Elsevier, 2nd Edition.

Wakelam, V., J. C. Loison, R. Mereau, and M. Ruaud (2017). In: *Molecular Astrophysics* 6, pp. 22–35.

Walsh, C., R. A. Loomis, K. I. Öberg, M. Kama, M. L. R. van 't Hoff, T. J. Millar, Y. Aikawa, E. Herbst, S. L. Widicus Weaver, and H. Nomura (2016). In: *ApJL* 823, Issue 1, article id. L10.

Watanabe, Y., N. Sakai, K. Sorai, and S. Yamamoto (2014). In: *ApJ* 788, Issue 1, article id. 4.

Weinbruch, S., H. Palme, and B. Spettel (2000). In: *Meteoritics and Planetary Science* 35, pp. 161–171.

Whittet, D. C. B., P. A. Gerakines, A. G.G. M. Tielens, A. J. Adamson, A. C. A. Boogert, J. E. Chiar, T. de Graauw, P. Ehrenfreund, T. Prusti, W. A. Schutte, B. Vandenbussche, and E. F. van Dishoeck (1998). In: *ApJ*, pp. L159–L163.

Willis, E. R., R. T. Garrod, A. Belloche, H. S. P. Muller, C. J. Barger, M. Bonfand, and K. M. Menten (2020). In: *A&A* 636.

Wirström, E. S., W. D. Geppert, m. Hjalmarson, C. M. Persson, J. H. Black, P. Bergman, T. J. Millar, M. Hamberg, and E. Vigren (2011). In: *A&A* 533, id.A24.

Wolfire, M. G., C. F. McKee, D. Hollenbach, and A. G.G. M. Tielens (2003). In: *ApJ* 587, Issue 1, pp. 278–311.

Woodney, L. M., M. F. A Hearn, D. G. Schleicher, T. L. Farnham, J. P. McMullin, M. C. H. Wright, J. M. Veal, L. E. Snyder, I. de Pater, J. R. Forster, P. Palmer, Y. J. Kuan, R. Williams W, C. C. Cheung, and B. R. Smith (2002). In: *Icarus* 157, Issue 1.

Wyrowski, F., C. M. Walmsley, W. M. Goss, and A. G.G. M. Tielens (2000). In: *ApJ* 543, Issue 1, pp. 245–256.